UNIVERSITY OF NOVA GORICA
GRADUATE SCHOOL

ULTRA-HIGH ENERGY COSMIC RAYS AND GALACTIC MAGNETIC FIELD

DISSERTATION

Mustafa Hussain

ADVISERS:
Prof.Dr. Danilo Zavrtanik
Doc.Dr. Darko Veberič

Nova Gorica, 2009

to my parents

First of all, I will like to thank Prof.Dr. Danilo Zavrtanik for accepting me as his PhD-student. His advices and his ability to formulate the most difficult tasks and questions in a simple way were priceless. My co-adviser Doc.Dr. Darko Veberič with his bright intellect, creativity, and passion for science not only motivated me in my darkest hours but also taught me more physics than anyone has ever done before. I am forever thankful for his patience and belief in me. I would also like to thank Dr. Serguei Vorobiov for his readiness to answer questions. I am especially grateful for all the help and assistance he provided me throughout my thesis. The contribution of other members of the Laboratory of Astroparticle Physics, University of Nova Gorica, should not be underestimated. I am especially indebted to Dr. Alex Creusot, Prof.Dr. Martin O'Loughlin, and Prof.Dr. Samo Stanič. During my stay in Slovenia, I befriended a bunch of linguists that are worth mentioning. The offices of Doc.Dr. Franc Marušič and Doc.Dr. Rok Žaucer became places of venting frustrations and planning new endeavors. I would also like to mention Vrinda S. Chidabaram, Amanda Saksida, Alja Ferme, Slavica Kochovska and Dr. Jonathan Kaye, the nicest linguists (people) I ever met.
People outside linguistics and astroparticle physics that I am grateful to are Doc.Dr. Biago Forte, Fei Gao, Dr. Martina Bergant, and Minoo Tasbihi. I would also like to thank my comrade-in-arms Teja Komel, and Niko Gorjup and his family for all their hospitality and kindness. The Norwegian community in Slovenia helped me feel at home. I would especially like to thank Marie Olsen, Jon Bangsund, and Lars "Bar" Jenssen.
My friends home in Oslo, who always found time to cheer me up and provide moral support, despite the fact I abandoned them for almost three years, consist of: Ragna Linboe, Monica Rundqvist, Esben Lund, Zahir Shah, Jon Pato, Fatima Pinto, Espen Gjøstøl, Hege Strand, Harald Nicolaisen, Benjamin Endre Larsen, Marte Nilsen, Iram Chaudhry, Torgeir Holgersen, Aksel Flack, Liv Kjersti Moen, Tanja Askvik, Sepideh Sadeghi, Tonje Larsen, Mehran Raja, and Johannes Wilm.
Last, but not least, I would like to thank my parents and my sister, for constantly supporting me. Survival would not have been possible without their care and consideration.

Abstract

In this work the prospects of cosmic ray astronomy in general and possibilities for particles originating from the galactic center and active galactic nuclei are investigated numerically by integrating trajectories of incoming cosmic rays backwards in time, in different models of the galactic magnetic field. In principle it is concluded that cosmic ray astronomy is possible for cosmic protons with energies of 10 EeV and above. In the case of the galactic center it is shown that for 0.1 to 1 EeV protons the galactic center is unobservable at Earth except when the galactic magnetic field is assumed to have field reversal at the galactic disk. For the active galactic nuclei case, the observed correlation between ultra-high energy cosmic-ray arrival directions and positions of active galactic nuclei, as reported by the Pierre Auger Observatory, is recalculated using original Auger data, corrected for magnetic deflections. The correlation becomes weaker, indicating that either the galactic magnetic field models are inaccurate or that the Auger data correlates with other astronomical objects rather than active galactic nuclei.
One of the predicted effects of magnetic deflections of cosmic rays from a common point source is the forming of thread-like multiplets. Their existence can be used to infer the position of the sources, making them a useful tool in cosmic ray astronomy. Groups of thread-like multiplets are constructed from data using the minimum spanning tree method. An interesting group of thread-like multiplets are found in proximity of Centaurus A. Simulations show that these multiplets probably are a result of chance coincidence.

Key words: propagation of ultra high energy cosmic rays, comic ray astronomy, galactic magnetic field models, magnetic deflections, extra-galactic exposure, galactic center, active galactic nuclei, thread-like multiplets.

Povzetek

V pričujočem doktorskem delu so z uporabo numerične povratne integracije trajektorij v različnih modelih galaktičnega magnetnega polja v splošnem raziskane možnosti za obstoj astronomije kozmičnih žarkov in možnosti, da so izvori teh energetskih delcev center Galaksije in aktivna galaktična jedra. Splošni zaključek predvideva možnost astronomije (astronomskih opazovanj) kozmičnih žarkov z energijami nad 10 EeV. V primeru galaktičnega centra se izkaže, da je iz Zemlje neopazljiv v vseh modelih galaktičnega magnetnega polja razen v tistih, ki vsebujejo inverzijo magnetnega polja na prehodu skozi galaktično ravnino. V primeru aktivnih galaktičnih jeder, za katere je Observatorij Pierre Auger objavil korelacijo med vpadnimi smermi kozmičnih žarkov ekstremnih enerij in pozicijami aktivnih galaktičnih jeder, so originalni podatki preračunani z upoštevanjem uklona nabitih delcev v galaktičnem magnetnem polju. Ugotovimo, da korelacija postane šibkejša, kar lahko kaže na dejstvo, da so modeli galaktičnega magnetnega polja neustrezni ali pa, da originalne meritve zares korelirajo in izvirajo iz drigih astronomskih objektov. Eden izmed napovedanih indikatorjev magnetnega uklona kozmičnih žarkov, ki izvirajo iz skupnega izvora, je oblikovanje podaljšnih nizov dogodkov. Njihovo identificiranje in obstoj so lahko uporabna orodja v astronomiji kozmičnih žarkov. Kandidate za skupine teh nizov kontruiramo s pomočjo metode drevesa najmanjše razsežnosti (minimum spanning tree). Ta metoda nam na izmerjenih podatki daje zanimive skupine nizov v bližini Centaurus A. Na žalost pa simulacije kažejo, da so lahko ti nizi le produkt naključnih sovpadanj.

Key words: razširjanje kozmičnih žarkov ekstremnih energij, astronomija kozmičnih žarkov, modeli galaktičnega magnetnega polja, magnetni ukloni, ekstragalaktična izpostavljenost, galaktični center, aktivna galaktična jedar, nizi dogodkov.

LaTeX

Contents

Chapter 1

Introduction

The origin and nature of the Ultra-high Energy Cosmic Rays (UHECR) has been a mystery ever since they were discovered in the period 1910 to 1912 [1]. Their energies reach up to and beyond 10^{20} eV, meaning that the microscopic particles can obtain macroscopic energies as 10^{18} eV is almost 1 J. Hence the questions about how and where they are accelerated, have been timely asked for decades. Speculations about the possible acceleration sites range from Active Galactic Nuclei (AGN) to Radio lobes [2, 3, 4, 5]. The main reason for their elusiveness is the steeply falling flux at high energies. The flux for the UHECR above 10^{20} eV is less than 1 event per square kilometer per century! Tremendous amount of effort has been invested in solving the puzzles surrounding the UHECR. Historically this led to the discoveries of the positron, muon, pion particles [6, 7, 8, 9], in addition to strange particles like kaons and lambdas, thus making the cosmic ray research the initiator of particle physics [10, 11]. By the development of better particle accelerators astrophysics and particle physics were separated as two distinctive fields of science. However, there are economical limits as far as the center-of-mass energy of terrestrial particle accelerators is concerned. The most important particle accelerator today is LHC at CERN with a maximum center-of-mass energy of 14 TeV. Clearly, the only way to study particles with energy in the range 10^{19} eV and above is to measure UHECR. However, as already mentioned, these particles are extremely rare. The southern site of the Pierre Auger Observatory (PAO) was built in order to gather a large amount of ultra-high energy data in reasonable time [12].

The UHECR are charged particles and are bent by magnetic fields. For cosmic ray astronomy this imposes an additional uncertainty since the galactic magnetic field is poorly understood. If the field is stronger than anticipated then experiments like PAO would not be feasible in terms of assigning their potential origin. If the field is within reasonable limits an effort has to be made in order to establish the deflections of the UHECR and correct their arrival directions or to establish energy limits where the deflections are negligible. This thesis is centered around this task.

Following sections give a brief description of the data detection and reconstruction methods used by the PAO. The energy spectrum, being one of the three fundamental observables [10] of UHECR, is also discussed.

1.1 Pierre Auger Observatory

The methods for detecting cosmic rays have greatly improved ever since Victor Hess' daring balloon missions in the beginning of the twentieth century [1]. As cosmic rays penetrate the sky they interact with air molecules, producing secondary particles. A cascade is started where enormous amount of secondary particles are produced. This cosmic ray induced cascade is called Extensive Air Shower (EAS). By collecting the secondaries on the ground via Surface Detectors (SD) the energies and the directions of the cosmic ray primaries are found. The majority of earlier UHECR experiments were measuring the properties of the EAS at ground. Alternatively, the Fly's Eye experiment developed a technique to measure the fluorescence light emitted by excited nitrogen

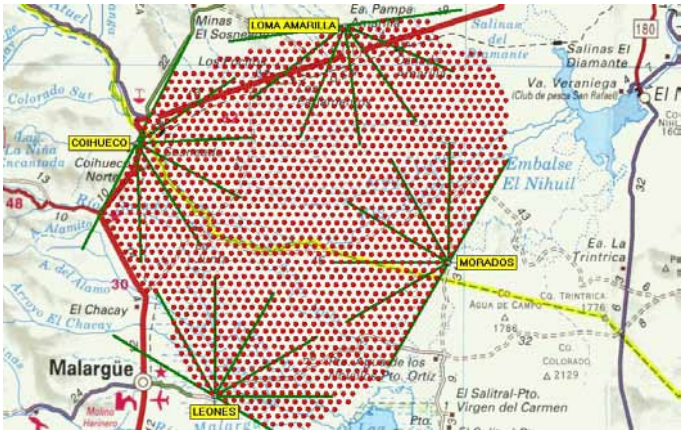

Figure 1.1: The Auger detector. Red dots are water tanks detecting Cherenkov radiation. These are surrounded by four buildings containing telescopes that measure fluorescence light.

molecules by which the energies and the directions of the cosmic rays are determined [13].

The Pierre Auger experiment combines for the first time in the history of comic ray experiments both Surface and Fluorescence Detector (FD) on a grand scale. The Auger detector is thus a hybrid detector with an optimal angular accuracy and energy measurement [12]. The following sections describe the EAS and the reconstruction procedure of obtained data.

1.1.1 Auger layout

In figure 1.1 the Auger layout is shown [14]. The Auger surface detector covers 3000 km^2 of the Argentinian Pampa Amarilla plain with 1600 detector units (see figure 1.1). Each of the units contains 12 tons of water. When particles from the cascade pass through, Cherenkov radiation in water is detected. The SD units are powered by both solar power and batteries. These are surrounded by four stations containing six Schmidt optic telescopes (FDs). The telescopes measure the fluorescence light emitted by excited nitrogen molecules.

The light detected by the SDs and FDs are converted into photoelectrons by PMTs, constituting the signal.

1.2 Extensive air showers

Due to their low flux it is impossible to detect a sufficient amount of UHECR directly by means of a single detector. The properties of the EAS over huge detection areas are rather used to infer cosmic ray energies and arrival directions. Figure 1.2 shows schematically the development of the EAS [15].

The energy of the cosmic ray primary is depleted through different types of cascades. The hadronic EAS is launched by a cosmic ray nucleon or nucleus primary that interacts hadronically producing a nucleonic cascade until reaching the ground. In addition, an enormous amount of neutral pions decay into photons, and because of this about 90% of the cosmic ray energy is feeding the electromagnetic cascade [12]. The rest of the energy is channeled through charged pion decays,

$$\pi^{\pm} \rightarrow \mu^{\pm} + \nu_{\mu}^{\pm}. \tag{1.1}$$

An important property of the EAS is the *depth of maximum* $X_{\max}$ that is measured by the fluorescence detectors. It is measured from the top of the atmosphere as an amount of traversed matter in the units of g cm^{-2} [16].

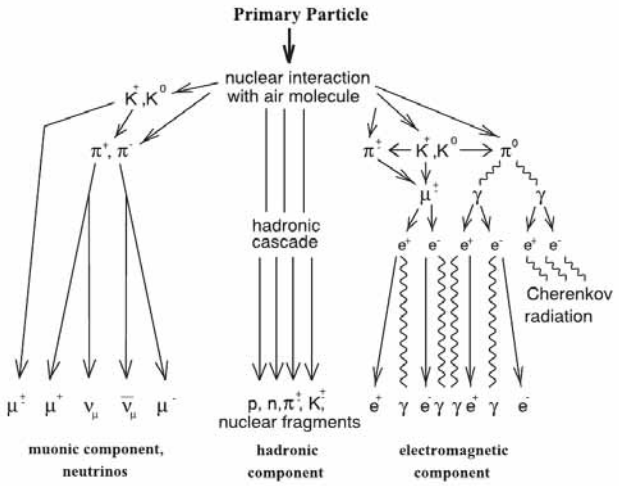

Figure 1.2: The different cascades and components constituting the EAS. The nucleon cascade (here termed hadronic cascade) is caused by the EAS initiating cosmic ray primary. As the primary traverses towards the ground, charged and neutral pions are produced, contributing to the muonic and electromagnetic components of the EAS as they decay. Here the contribution of kaons is also depicted.

At a certain altitude $h_{\max}$ the number of secondaries N produced by the cosmic-ray-induced shower reach a maximum, $N_{\max} = N(h_{\max})$. The integrated air density traversed by the shower from the top of the atmosphere (i.e. infinite height) to the altitude $h_{\max}$ is denoted as $X_{\max}$ [17].

A heavy cosmic ray primary, like iron, with a given energy produces an EAS that develops higher up in the atmosphere than an EAS produced by a proton with the same energy [18, 19]. This also implies that for iron the shower produces a maximum number of secondaries higher up in the atmosphere as well. Thus, the $X_{\max}$ for iron induced showers is in average lower than for protons.

The depth of maximum changes [20] approximately as a function of the energy of the shower inducing cosmic ray and its atomic mass A,

$$X_{\max} \propto \ln\left(\frac{E}{A}\right). \tag{1.2}$$

The second important property of the EAS is its lateral spread and is measured by the SD.

1.3 Reconstruction – surface detector

The Pierre Auger experiment uses water tanks as the surface detectors. As charged relativistic particles hit the water tanks Cherenkov photons are produced. These are collected by PMTs that yield a signal that is used to infer the energy of the cosmic ray. The direction of the latter is determined by a fit of the shower axis[1] of the EAS [12, 16, 21, 22, 23] to the arrival times recorded by the SD stations.

1.4 Shower geometry

Experiments using surface detectors, like water Cherenkov tanks, take the advantage of the fact that the front of the EAS does not hit the tanks simultaneously. Rather, the EAS hits the tanks

[1] The shower axis points opposite to the direction of the propagation of the shower.

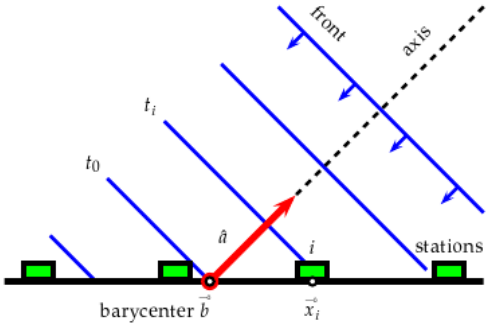

Figure 1.3: The shower front modelled as planar front. The barycenter is assumed to be at the origin [22].

at different arrival times. As a first approximation, the direction of the cosmic rays are deduced from the arrival times assuming a planar shower front [12, 16, 22, 23]. The EAS front viewed as planar front is shown in figure 1.3.

The central features in figure 1.3 are the barycenter $\vec{b}$ and the shower axis $\hat{a}$. For the plane model the barycenter is the origin from where all the distances are measured [22, 24] and is also, in first approximation, assumed to be the shower *impact point* on the ground [22]. The barycenter is given [24, 25, 26] by a signal-weighted sum[2],

$$\vec{b} = \frac{\sum_i \sqrt{S_i}\,\vec{x}_i}{\sum_i \sqrt{S_i}}, \tag{1.3}$$

where S_i is the signal measured in station i. The shower evolution $\vec{x}(t)$ is described as [22],

$$\vec{x}(t) = \vec{b} + \mathrm{c}\,(t - t_0)\cdot\hat{a}, \tag{1.4}$$

where axis $\hat{a}$ is a normal vector[3] pointing towards the incoming direction of the cosmic ray, and time t_0 is measured when the shower track arrives at the barycenter. In order to obtain the direction of the shower axis, and thus the direction of the incoming comic ray, a shower plane is defined perpendicular to the shower axis [22]. This plane arrives at a point $\vec{x}$ at the time,

$$ct\,(\vec{x}) = ct_0 - \left(\vec{x} - \vec{b}\right)\cdot\hat{a}, \tag{1.5}$$

and the direction of the shower axis is found by minimizing χ^2,

$$\chi^2 = \sum_i \frac{|t_i - t\,(\vec{x}_i)\,|^2}{\sigma_{t_i}^2} = \sum_i \frac{|\mathrm{c}t_i - \mathrm{c}t_0 + \vec{x}_i\hat{a}|^2}{\mathrm{c}^2\sigma_{t_i}^2}, \tag{1.6}$$

where t_i is the measured signal start time and $\vec{x}_i = \vec{x}_i - \vec{b}$ the relative position of station i. σ_{t_i} is the time uncertainty of station i.

The planar front model is only used for finding the first approximation of the shower axis [22]. The shower front is described more accurately as a concentric spherical front (see figure 1.4).

[2] $\vec{b}$ is a point and not a vector. The difference between a point and a vector is shown by affine transformations. The rotational part of an affine transformation changes the direction of a vector, while the translational part of an affine transformation changes the absolute value of the coordinates of a point [22].

[3] Normalized vectors will be denoted with a caret, i.e. $\hat{a}$.

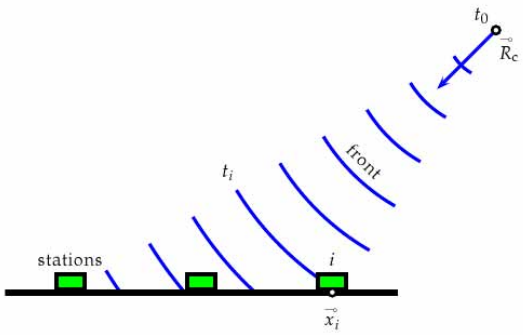

Figure 1.4: The shower front modelled as a spherical front. t_0 is the approximated starting time of the shower [22].

The concentric spherical shower front reaches station i at time t_i [22],

$$ct_i = ct_0 + |\vec{R}_c - \vec{x}_i|, \tag{1.7}$$

where t_0 indicates the time when the shower is initiated and $\vec{R}_c$ is the apparent origin of the shower (shower center) [22], and the shower axis is obtained by minimizing

$$\chi^2 = \sum_i \frac{\left(c\left(t_i - t_0\right) - |R_c\hat{a} - \vec{x}_i|\right)^2}{c^2\sigma_{t_i}^2}, \tag{1.8}$$

where $\hat{a}$ is the shower axis.

1.5 Shower energy

The secondaries of a shower are scattered laterally out from the axis primarily by Coulomb scattering [27]. The lateral signals from different stations are fitted with a suitable Lateral Distribution Function (LDF) as seen in figure 1.5. The core distance is the distance of a station from the impact point of the shower on the ground. The signals are in units of Vertical Equivalent Muon (VEM). One VEM is equivalent to the signal detected by the PMTs when a single muon enters the station vertically, centered on the tank axis.

For the Auger experiment the signals are most accurately reconstructed for core distances of 1000 m and the corresponding parameter in the LDF is denoted as S_{1000}. The measured signal is given by [22]

$$S\left(r\right) = S_{1000}\, f_{\mathrm{LDF}}\left(r\right) \tag{1.9}$$

where $f_{\mathrm{LDF}}\left(r\right)$ is a shape parametrization [22, 28] where $f_{\mathrm{LDF}}\left(1000\,\mathrm{m}\right) = 1$. The distance r is measured perpendicularly from the station to the axis of the shower [24].

There is a proportionality between S_{1000} and the shower inducing cosmic ray energy [12, 29]. By obtaining S_{1000} from the chosen LDF distribution the energy of the shower inducing cosmic ray is inferred by the Constant Intensity Cut (CIC) method [30, 31].

1.6 Reconstruction – fluorescence detector

As seen in figure 1.1 four buildings with telescopes measuring fluorescence light are located around the SD array. The EAS emits fluorescence light produced by excited nitrogen molecules

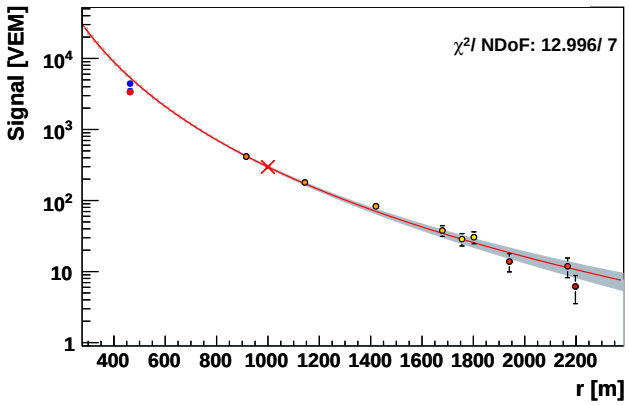

Figure 1.5: The signals yielded by the SDs as a function of the distance from the impact point of the shower core on the ground (core distance). The dots denote the signals from different SD stations while the cross represent the S_{1000} signal.

in the air. The number of fluorescence photons produced by charged particles propagating a distance dl is

$$\frac{\mathrm{d}N_\gamma}{\mathrm{d}l} = Y_\mathrm{f} N_\mathrm{e}, \tag{1.10}$$

where N_e is the number of charged particles, and Y_f is the fluorescence yield in photons per charged particle per meter [12, 32].

The fluorescence photons are measured at several atmospheric depths X, yielding the longitudinal profile of the shower $N(X)$, and in turn, the integral of the longitudinal profile yields the total electromagnetic shower energy.

1.7 Shower geometry

The fluorescence photons in equation (1.10) are seen as narrow pattern of PMT hits of the FD camera as seen in figure 1.6, and the Shower Detector Plane (SDP) in figure 1.7 is defined by these hits [33]. In order to find the direction of the shower axis in the SDP plane, the impact parameter R_p and the incident angle $\psi = \pi - \chi_0$ are determined [16, 34]. Like for the SD the shower axis is deduced from timing. The arrival time of the fluorescence light at each PMT is [35],

$$t_i = T_0 + \frac{R_\mathrm{p}}{c} \tan\left(\frac{\chi_0 - \chi_i}{2}\right), \tag{1.11}$$

where T_0 is the time when the shower is at distance R_p away from the detector, χ_0 is the angle between the shower axis and the ground, and χ_i is the height angle of PMT i. By introducing the incident angle $\psi = \pi - \chi_0$, equation (1.11) is rewritten [34], and the parameters R_p, ψ, and T_0 defining the shower axis are found by χ^2 minimization,

$$\chi^2 = \sum_i^N \frac{(t_i - t_{i,\mathrm{obs}})^2}{\sigma_i^2}, \tag{1.12}$$

where $t_{i,\mathrm{obs}}$ is the observed hit time for PMT i and σ_i^2 its uncertainty [12]. Here R_p, ψ, and T_0 are varied so that a minimum of equation (1.12) is achieved.

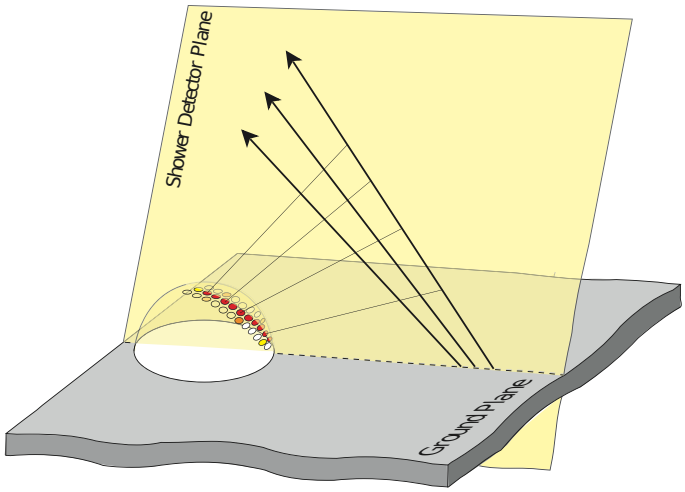

Figure 1.6: The narrow pattern of PMT hits on the FD camera caused by the fluorescence photons. The shower front is modeled as a planar front [33].

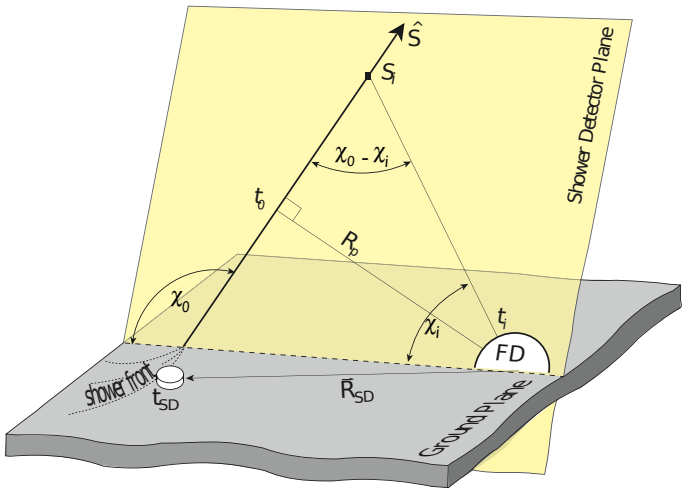

Figure 1.7: The shower detector plane constructed from the PMT hits in the fluorescence detector. Here the shower axis is denoted with vector $\hat{S}$, and S_i is the point of fluorescence emission [33].

1.8 Shower energy

As noted in section 1.6 the energy of the shower inducing cosmic ray is retrieved by integrating the longitudinal profile $N(X)$ of the shower. The profile is described by the Gaisser-Hillas function [36],

$$N(X) = N_{\max}\left(\frac{X - X_0}{X_{\max} - X_0}\right)^{\frac{X_{\max}-X_0}{\lambda_{\mathrm{GH}}}} \exp\left(\frac{X_{\max} - X}{\lambda_{\mathrm{GH}}}\right), \tag{1.13}$$

where $N_{\max}$ is the maximum shower size, λ_{GH} is a constant related to the primary-air cross-section, and X_0 improves the modeling of the profile.

The profiles of equation (1.13) are generated and compared to the observed profiles. The parameters $N_{\max}$, $X_{\max}$ and X_0 are varied until the generated profile is comparable with the observed and thus the depth of the maximum in the electromagnetic cascade is obtained [12].

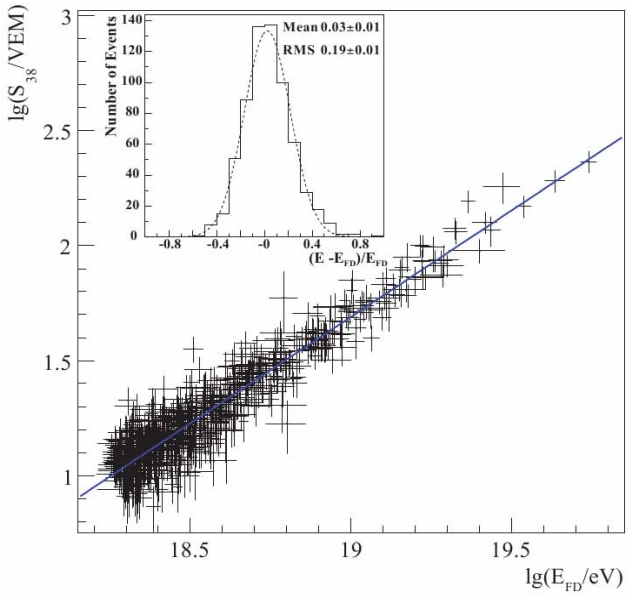

Figure 1.8: The correlation between the S_{38° signal and the energy as measured by the FDs.

The energy is given straightforwardly by integrating the measured profile [12],

$$E_{\mathrm{em}} = \frac{E_{\mathrm{c}}}{\lambda_r} \int N_e\,(X)\,\mathrm{d}X, \tag{1.14}$$

where E_{c} is the electron critical energy and λ_{r} the electron radiation length in air [37].

1.9 Hybrid reconstruction

Both detection methods described above have their unique systematic uncertainties. These are highly reduced by the hybrid detection.

The time t_i in equation (1.11) has almost linear dependence on the elevation angle χ_i. The departure from linearity is not easily seen for short tracks, i.e. for tracks that are reconstructed for a small range of χ_i values [38]. As mentioned in section 1.7 the parameters R_{p}, $\psi = \pi - \chi_0$ and T_0 are varied in order to find the χ^2 minimum. However, due to the almost linear form of equation (1.11) for short tracks there exist several possible solutions of R_{p} and ψ that are compatible with measurement error [12, 24, 38], leading to uncertainties in the energy and angular reconstruction.

This ambiguity in equation (1.11), which is used to time fit the SDP as given by the fluorescence data, is constrained by time of shower impact on ground that is obtained from the SD [34]. This is the essence of the hybrid method.

CIC reconstruction

The energy of the primaries is reconstructed in accordance to the CIC method [30, 31, 39, 40] using the energy measured by the FD and S_{1000} from the SD. The method assumes the flux of cosmic rays reaching the Earth is isotropic and homogeneous for all energies. However, for a given energy the S_{1000} signal is reduced with increasing zenith angle θ due to attenuation of the shower [31, 40] in the atmosphere. At larger zenith angles there are fewer shower particles and hence lower S_{1000} values. The intensity distribution of S_{1000} is plotted as a function of $\cos^2(\theta)$

and uniformity of the intensity is obtained by requiring that each bin contains the same amount of events [24, 31]. The attenuation curves are consequently fitted [40] with the function,

$$\mathrm{CIC}(\theta) = 1 + a\,x + b\,x^2, \tag{1.15}$$

where $x = \cos^2(\theta)$ - $\cos^2(38^\circ)$. The S_{1000} is converted into a reference signal [22, 31],

$$S_{38^\circ} = \frac{S(1000)}{\mathrm{CIC}(\theta)}. \tag{1.16}$$

Having obtained the S_{38° signal the energy is deduced by relating S_{38° to the energy measured from the FD [31]. For each S_{38° value (deduced from the SD) in figure 1.8, there is a corresponding energy as measures by the FD [40].

A clear linear relation is seen and the energy is in general calculated as [31]

$$E = 0.149\,(S_{38^\circ})^{1.8}\,\mathrm{EeV}. \tag{1.17}$$

1.10 Energy spectrum

One of the most fascinating aspects of UHECR is the measured spectrum of their energies. Figure 1.9 shows the energy spectrum as measured over the years by different types of cosmic ray experiments. The most striking feature is the enormous extension of the spectrum in flux (31 orders of magnitude) and energy (12 orders of magnitude) [41]. The flux rate changes around the energies 10^{15}, 10^{18} and 10^{19} eV. In the jargon of cosmic ray research these flux rate changing regions in figure 1.9 are called the "knee", the "second knee" and the "ankle". There exists an abundance of literature dealing with these features of the energy spectrum and the possible acceleration mechanisms of the cosmic rays as shown in [42] and the references therein.

The knee at 10^{15} eV was discovered in 1958 [42] and several possible explanations of its origin exist [43]. The second knee was discovered soon after [44]. The ankle discovered in the sixties is thought to indicate the transition from galactic cosmic rays to extra-galactic cosmic rays. As seen in figure 1.9 (modified from [11] and [16]) the flux for energies above 10^{20} eV is extremely low. This suppression is explained by the Greisen-Zatsepin-Kuz'min (GZK) cutoff [45, 46]. Greisen, Zatsepin, and Kuz'min showed that protons interacting with the Cosmic Microwave Background (CMB) eventually lose energy through pion production,

$$\begin{aligned} p + \gamma_{\mathrm{CMB}} &\rightarrow n + \pi^+ \\ &\rightarrow p + \pi^0 \\ &\rightarrow p + e^+ + e^-. \end{aligned} \tag{1.18}$$

They predicted a cutoff in the energy spectrum at $E_{\mathrm{GZK}} = 6 \cdot 10^{19}$eV. A cutoff at similar energies is also predicted for heavy nuclei [45] and photons (for details see [16, 42] and references therein).

The GZK cutoff makes, in principle, charged particle astronomy possible. For 10^{20} eV protons equations 1.18 yield an attenuation length of less than 50 Mpc implying not only their extra-galactic origin but also where the source candidates are located. An additional constraint was put on possible sources for the UHECR by Hillas [3]. The Larmor radius of a cosmic ray [3] accelerated in a source with magnetic field B can be written as,

$$r_{\mathrm{L}} = \frac{1.08}{Z}\left(\frac{E}{10^{15}\,\mathrm{eV}}\right)\left(\frac{\mu\mathrm{G}}{B}\right), \tag{1.19}$$

where Z is the charge of the accelerated particle. By requiring that the size of the source is larger than the Larmor radius,

$$L > \frac{2\,r_{\mathrm{L}}}{\beta_{\mathrm{s}}}, \tag{1.20}$$

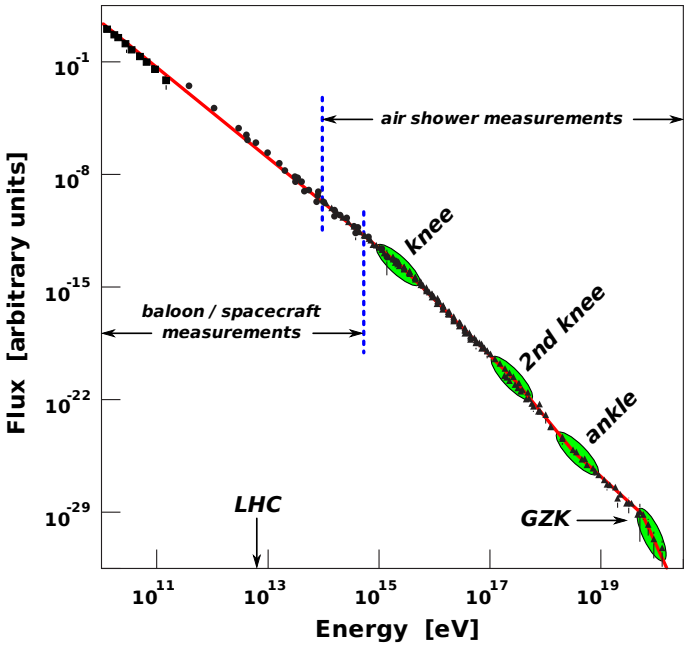

Figure 1.9: The measured energy spectrum of different cosmic ray experiments through history. The highest achievable energy at LHC accelerator is also shown.

where L is the size of the acceleration site and β_s is the efficiency of the acceleration mechanism, equation (1.19) is transformed into [3],

$$\left(\frac{E}{10^{15}\,\mathrm{eV}}\right) < \frac{Z\beta_\mathrm{s}}{2.16}\left(\frac{B}{\mu\mathrm{G}}\right)\left(\frac{L}{\mathrm{pc}}\right). \tag{1.21}$$

Equation (1.21) shows that the maximum energy obtained by a cosmic ray is a function of the both the size and the strength of the magnetic field of the source. The cosmic rays are contained in the acceleration site until inequation (1.20) is violated.

Figure 1.10 shows the magnetic fields and the sizes of the potential sources of the UHECR. The diagonal lines are given by the equation

$$\left(\frac{B}{\mu\mathrm{G}}\right) > \frac{2.16}{Z\beta_\mathrm{s}}\left(\frac{E}{10^{15}\,\mathrm{eV}}\right)\left(\frac{\mathrm{pc}}{L}\right), \tag{1.22}$$

for protons with energy of $10^{20}\,\mathrm{eV}$, and $\beta_s = 1$ and $\beta_s = 1/300$. Acceleration sites below these lines are unable to produce protons with energies above $10^{20}\,\mathrm{eV}$. All the sites are excluded for $\beta_s = 1/300$ while for $\beta_s = 1$ only AGN and jets from radio galaxies remain.

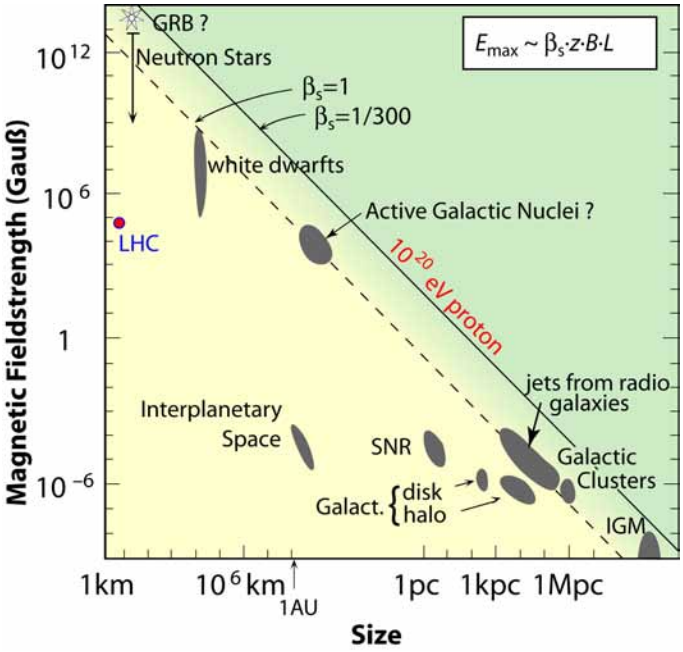

Figure 1.10: The sizes and magnetic field strengths of potential acceleration sites of the UHECR. Diagonal lines are given by equation (1.22) for 10^{20} eV protons with two different values of β_s. The plot [47], modified from [48], is a version of the famous Hillas plot [3].

Chapter 2

The Galactic Magnetic Field

2.1 Introduction

With the construction of the Pierre Auger Observatory charged particle astronomy is now a real possibility, complementing optical and radio astronomy. However, this requires a deeper understanding of the Galactic Magnetic Field (GMF). The GMF is not measured directly. A wide range of methods are used to deduce its magnitude and general structure. However, different, even contradictory, results have emerged even when the same method was applied. In literature this has led to an inflation of models trying to describe the GMF. This chapter reviews the most important ones and subsequently checks their impact on the ultra-high energy cosmic rays traversing the galaxy. Particles of extra-galactic origin have additionally traveled through wast distances filled with Inter-Galactic Medium (IGM) and the corresponding Extra-Galactic Magnetic Field (EGMF). The chapter starts with a general description of the journey of the charged particles through both galactic and extra-galactic magnetic field.

2.2 Propagation of UHECRs in the galactic and the extra-galactic magnetic field

The strength of the extra-galactic magnetic field components outside of cluster of galaxies is supposed to have the upper limits [49],

$$\begin{aligned} B_{\text{rand}}^{\text{EGMF}} &\approx 1\,\text{nG}, \\ \langle B_{\text{LS}}^{\text{EGMF}} \rangle &\approx 0.01\,\text{nG}, \end{aligned} \tag{2.1}$$

where $B_{\text{rand}}^{\text{EGMF}}$ is the amplitude of the random component and $\langle B_{\text{LS}}^{\text{EGMF}} \rangle$ is the large scale component of the extra-galactic magnetic field. For an ultra-relativistic cosmic ray the gyroradius in a constant magnetic field is given by [49],

$$r_{\text{g}} = \frac{E}{ZeBc}, \tag{2.2}$$

where E is its energy, Ze is its charge, and B is the magnetic field. Assuming $B = \langle B_{\text{LS}}^{\text{EGMF}} \rangle$, equation (2.2) can be rewritten as

$$r_{\text{g}} = \left(\frac{10.8}{Z}\right) \left(\frac{E}{10^{20}\,\text{eV}}\right) \left(\frac{10^{-11}\,\text{G}}{\langle B_{\text{LS}}^{\text{EGMF}} \rangle}\right) 10^{9}\,\text{pc}. \tag{2.3}$$

The deflection α of cosmic rays traveling a distance D is approximately given by $\alpha \approx D/r_g$, and thus the deflection in the large scale field is expressed as [49],

$$\alpha = 0.53^\circ Z \left(\frac{D}{100\,\mathrm{Mpc}}\right)\left(\frac{\langle B_{\mathrm{LS}}^{\mathrm{EGMF}}\rangle}{10^{-11}\,\mathrm{G}}\right)\left(\frac{10^{20}\,\mathrm{eV}}{E}\right). \tag{2.4}$$

For Auger energies up to $E = 100\,\mathrm{EeV}$ for protons ($Z = 1$) and $\langle B_{\mathrm{LS}}^{\mathrm{EGMF}}\rangle = 10^{-11}\,\mathrm{G}$, equation (2.2) yields a gyroradius of approximately 10 Gpc. The trajectories of 100 EeV protons are thus linear in the large scale component of the extra-galactic magnetic field. This indicates negligible deflections. By using $E = 100\,\mathrm{EeV}$, $\langle B_{\mathrm{LS}}^{\mathrm{EGMF}}\rangle = 10^{-11}\,\mathrm{G}$, $Z = 1$ and $D = 100\,\mathrm{Mpc}$ equation (2.4) yields a deflection of only 0.5°.

For the random component the calculation is not so straightforward. The extra-galactic sky is filled with randomly oriented magnetic cells with a given coherence length, ℓ_{coh}. The cosmic rays are deflected randomly after encountering each such cell, resulting in a diffusion in the plane perpendicular to the direction of travel [49]. Given a magnetic cell of size $2\ell_{\mathrm{coh}}$ the deflection of a charged particle traversing through it is [49],

$$\delta\alpha \approx \frac{2ZeB_{\mathrm{rand},\perp}^{\mathrm{EGMF}}\ell_{\mathrm{coh}}}{E}. \tag{2.5}$$

where $B_{\mathrm{rand},\perp}^{\mathrm{EGMF}}$ is the component of $B_{\mathrm{rand}}^{\mathrm{EGMF}}$ that is perpendicular to the velocity direction of the cosmic ray. In a distance D the charged particle has encountered N magnetic cells with different field orientations yielding different deflections. The Root Mean Square (RMS) deflection is

$$\alpha_{\mathrm{rms}}^2 = \langle\delta\alpha_1^2\rangle + \langle\delta\alpha_2^2\rangle + \cdots = \sum_i^N \langle\delta\alpha_i^2\rangle, \tag{2.6}$$

where $N = D/2\ell_{\mathrm{coh}}$ is the number of magnetic cells encountered by the traversing charged particles. Expression 2.6 is rewritten as [49],

$$\alpha_{\mathrm{rms}}^2 = N\,\frac{\sum_i^N\langle\delta\alpha_i^2\rangle}{N} = N\,\langle\langle\delta\alpha^2\rangle\rangle = 2D\ell_{\mathrm{coh}}\left(\frac{Ze}{E}\right)^2\langle\langle B_{\mathrm{rand},\perp}^{\mathrm{EGMF}}\rangle\rangle, \tag{2.7}$$

and at our galaxy the RMS deflection angle is

$$\alpha_{\mathrm{rms}} \approx 10.5^\circ Z\left(\frac{B_{\mathrm{rand}}^{\mathrm{EGMF}}}{1\,\mathrm{nG}}\right)\left(\frac{10^{20}\,\mathrm{eV}}{E}\right)\sqrt{\left(\frac{D}{100\,\mathrm{Mpc}}\right)\left(\frac{\ell_{\mathrm{coh}}}{1\,\mathrm{Mpc}}\right)}. \tag{2.8}$$

For $\ell_{\mathrm{coh}} = 1\,\mathrm{Mpc}$, $B_{\mathrm{rand}}^{\mathrm{EGMF}} = 1\,\mathrm{nG}$ and $D = 50\,\mathrm{Mpc}$, the deflection is 7.4° for 100 EeV protons. Apparently equation (2.8) seems to make charged particle astronomy, at least for large distances, very difficult. However, due to the chaotic and uneven nature of the intergalactic space filled with galaxy clusters and filaments the deflections of the traversing particles are less than expected [50].

Particles traveling through massive clustered regions at distances of order $\sim 100\,\mathrm{Mpc}$ experience significant deflections [50]. However, these massive clustered regions cover only a negligible fraction of the sky, and thus, by excluding them, the deflections caused by the intergalactic magnetic field is only of order $1^\circ - 2^\circ$ [50]. Here the effects of the intergalactic field are thus omitted all together.

The GMF also have large scale and random components. The large scale deflection is given by [51],

$$\alpha = 0.53^\circ Z\left(\frac{D}{\mathrm{kpc}}\right)\left(\frac{B_{\mathrm{LS}}^{\mathrm{GMF}}}{\mu\mathrm{G}}\right)\left(\frac{10^{20}\,\mathrm{eV}}{E}\right), \tag{2.9}$$

where $B_{\mathrm{LS}}^{\mathrm{GMF}}$ is the large scale component of the GMF.

The equations (2.4) and (2.9) for the extra-galactic and galactic large-scale components are the same. Only the units differ due to the different scales involved.

The random component of the GMF is constituted by magnetic cells with coherence lengths in the range of only 10 pc to 100 pc [52]. The magnetic strength, $B_{\rm rand}^{\rm GMF}$, of each of these cells is comparable to the strength of the large scale component, $B_{\rm LS}^{\rm GMF}$ [52].

Assuming that the distance D traveled by the charged particles in the galaxy is much larger than the coherence length $\ell_{\rm coh}$ of the galactic magnetic cells, the deflection caused by the random component of the GMF is estimated to [53],

$$\alpha_{\rm rms} \approx 0.01^\circ Z \left(\frac{B_{\rm rand}^{\rm GMF}}{\mu{\rm G}}\right)\left(\frac{10^{20}\,{\rm eV}}{E}\right)\sqrt{\left(\frac{D}{\rm kpc}\right)\left(\frac{\ell_{\rm coh}}{1\,{\rm pc}}\right)}. \tag{2.10}$$

As is shown in the following section the magnitude of the GMF and its components is derived by various observational methods, including Faraday rotation. Using Faraday rotation measurements J.L. Han and G.J. Qiao [54], and R.G. Rand and A.G. Lyne [55] found an average local large scale regular field strength of $1.4\,\mu$G. For 100 eV protons traveling 20 kpc, and $B_{\rm LS}^{\rm GMF} = B_{\rm rand}^{\rm GMF} = 1.4\,\mu$G and $\ell_{\rm coh} = 100$ pc, equations (2.9) and (2.10) yield deflections of 10° and 0.6°, respectively. It is clear that the deflection caused by the random component of the GMF is negligible.

2.3 Experimental methods

There are many ways to calculate or infer the magnitude or the structure of the GMF. The observational methods are [56],

- Faraday rotation,
- Synchrotron emission,
- Zeeman splitting,
- Starlight polarization.

Faraday rotation is the most used method for deriving models of the GMF. Faraday rotation measurements are convenient since the line-of-sight component of the large scale regular component of the GMF, or $B_{\rm LS,\shortparallel}^{\rm GMF}$, is derived directly (see e.g. [52]). Synchrotron emission on the other hand yields the magnitude of the perpendicular component of both the total and the large scale regular field, complementing Faraday rotation (see e.g. [52]). Zeeman splitting is difficult to observe and starlight polarization does not provide any information that is not already found by synchrotron emission [56]. Thus, only Faraday rotation and Synchrotron emission are discussed in the following sections.

2.3.1 Faraday rotation

Faraday rotation of pulsars makes a direct estimation of $B_{\rm LS,\shortparallel}^{\rm GMF}$ in a given region possible, and combining this with the fact that pulsars have known distances and emit very linearly polarized light, creates a very powerful tool for probing the GMF [54, 57]. In addition, the pulsars are numerous ensuring a three dimensional description of the field [58]. In the following Faraday rotation is derived (for more details see reference [59] where the whole derivation presented here is found).

When a electromagnetic wave from pulsars traverses the galaxy, along the way it encounters and displaces free electrons in the interstellar medium. For electrons the equation of motion for a displacement $\vec{s}$ in a magnetic field in the z-direction is expressed as [59],

$$\frac{{\rm d}^2\vec{s}}{{\rm d}t^2} = -\frac{e}{m_e}\left(\vec{E} + \frac{{\rm d}\vec{s}}{{\rm d}t}\times\vec{B}\right) - \frac{f}{m}\vec{s}, \tag{2.11}$$

where m_e is the electron mass, f is the force constant and $\vec{B} = (0, 0, B_z)$. $\vec{E}$ is the electric field caused by the electromagnetic wave. The differential equation (2.11) is solved by introducing complex functions of the form

$$\begin{aligned} \vec{s} &= \vec{s_0} \exp(i\omega t), \\ \vec{E} &= \vec{E_0} \exp(i\omega t). \end{aligned} \tag{2.12}$$

In addition, assuming that $\vec{s}$ and $\vec{E}$ are perpendicular to the z-direction, and given the relations $E_\pm = E_x \pm iE_y$ and $s_\pm = s_x \pm is_y$, equation (2.11) is written as

$$\begin{aligned} \left(\omega_0^2 - \omega^2 - \omega\Omega\right) s_+ &= -\frac{e}{m} E_+, \\ \left(\omega_0^2 - \omega^2 + \omega\Omega\right) s_- &= -\frac{e}{m} E_-, \end{aligned} \tag{2.13}$$

where Ω is the electron cyclotron frequency $\Omega = eB_z/m_e$, and ω_0^2 is f/m. In short, $s_\pm$ is rewritten as

$$s_\pm = -\frac{e}{m} \frac{E_\pm}{\omega_0^2 - \omega^2 \mp \omega\Omega}. \tag{2.14}$$

The electric displacement and its polarization is given respectively by

$$D_\pm = \epsilon\epsilon_0 E_\pm = \epsilon_0 E_\pm + P_\pm, \tag{2.15}$$

$$P_\pm = -en_e s_\pm, \tag{2.16}$$

where n_e is the electron density and $s_\pm$ is given by the equation (2.14). Using the expression in equation (2.14), the polarization $P_\pm$ in equation (2.16) is rewritten as

$$P_\pm = -en_e s_\pm = E_\pm \frac{n_e e^2/m}{\omega_0^2 - \omega^2 \mp \omega\Omega}. \tag{2.17}$$

Equation (2.15) eventually yields

$$\epsilon_\pm = 1 + \frac{P_\pm}{\epsilon_0 E_\pm} = 1 + \frac{n_e e^2/\epsilon_0 m}{\left(\omega_0^2 - \omega^2 \mp \omega\Omega\right)} \equiv n_\pm^2(\omega), \tag{2.18}$$

where $n_\pm(\omega)$ is the refractive index. $n_+(\omega)$ and $n_-(\omega)$ describe two different waves passing through the interstellar medium, namely left-handed and right-handed circularly polarized waves. The variable ω is thus the angular frequency, $\omega = 2\pi f$. Their associated electric fields in the presence of a magnetic field yield the following relations

$$\begin{aligned} n(\omega) &= \frac{1}{2}\left(n_+(\omega) + n_-(\omega)\right), \\ \phi &= \frac{w}{2c}\left(n_+(\omega) - n_-(\omega)\right) z, \end{aligned} \tag{2.19}$$

where ϕ is the angle of polarization. Assuming $\Omega \ll \omega$ and that the medium has a low density ($n(\omega) \approx 1$ and $\omega_0 = 0$), equation (2.19) yields the total angle of the rotation of the polarization plane

$$\mathrm{d}\phi \approx \frac{e^3}{2\epsilon_0 m_e^2 c\omega^2} \int_0^{l_s} n_e(\ell)\, B_{\shortparallel}(\ell)\, \mathrm{d}\ell, \tag{2.20}$$

where $B_{\shortparallel}(\ell)$ is the line-of-sight large scale regular component of the magnetic field and $n_e(\ell)$ is the electron density along the line of sight [56]. Equation (2.20) is usually written as [56],

$$\phi = \mathrm{RM}\,\lambda^2 + \phi_0, \tag{2.21}$$

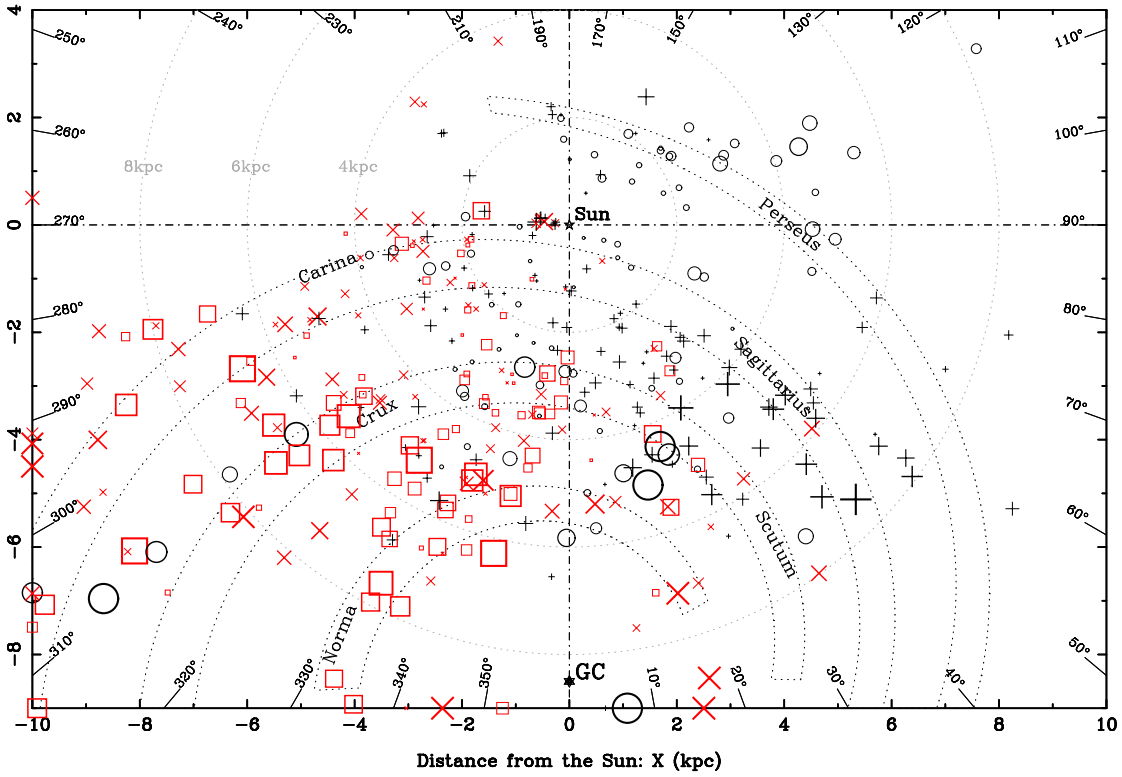

Figure 2.1: A compilation of RMs from pulsars. The sizes of the symbols are proportional to the RM values. The symbols + and × denote positive RM values while negative RM values are given by circles and squares. New measurements are in red while old measurements are in black. Plot is taken from J.L. Han *et al.* [58]. For details about the (old and new) measurements and the different catalogs used see the same reference.

where the measured quantity RM is the Rotation Measure and is given by ϕ/λ^2. ϕ_0 is the initial polarization angle of the traveling electromagnetic wave and λ is its wave length. In terms of degrees rotated per square meter the Rotation Measure is rewritten as [56],

$$\mathrm{RM} \approx \frac{14^\circ}{\mathrm{m}^2} \int_0^{l_s} \left(\frac{n_e}{\mathrm{cm}^{-3}}\right) \left(\frac{B_{\parallel}}{\mu\mathrm{G}}\right) \left(\frac{\mathrm{d}\ell}{\mathrm{kpc}}\right). \tag{2.22}$$

The electromagnetic waves emitted by the pulsars are linearly polarized and are measured by radio telescopes. The RM angle is deduced by measuring the polarization rotation angle, ϕ, for many wavelengths [56, 60]. The results of these measurements are seen in figure 2.1 (taken from [58]). The figure is a compilation of RM data from pulsars in the spiral arms for galactic latitudes $|b| < 8^\circ$. The positive and negative values correspond to different field directions indicating field reversals between the spiral arms.

After mapping RM values from pulsars, the task is to determine the magnetic strength of the different regions and spiral arms of the galaxy. In order to get the magnetic field a second quantity is needed, namely the Dispersion Measurement, DM (see e.g. [52, 54, 57, 58, 61, 62]),

$$\mathrm{DM} = \frac{3.1 \cdot 10^{13}}{\mathrm{m}^2} \int_0^{l_s} \left(\frac{n_e}{\mathrm{cm}^{-3}}\right) \left(\frac{\mathrm{d}\ell}{\mathrm{kpc}}\right). \tag{2.23}$$

The average regular magnetic field along the line of sight (see e.g. [52, 54, 57, 58, 62]) is given by,

$$\frac{B_{\parallel}}{\mu\mathrm{G}} = 1.232 \frac{\mathrm{RM}}{\mathrm{DM}}. \tag{2.24}$$

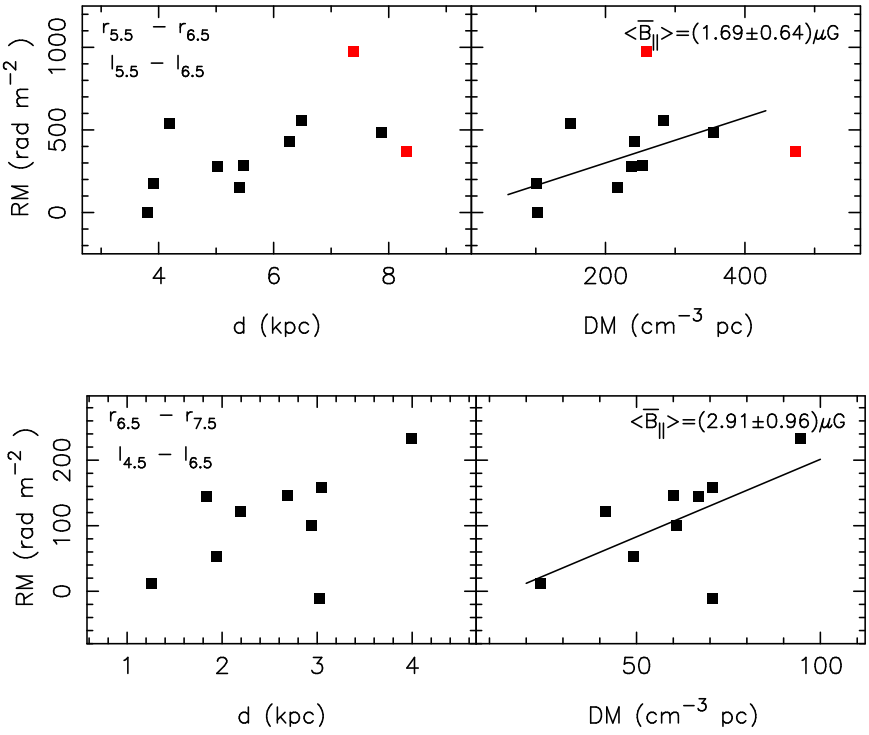

Figure 2.2: The upper panel shows measured RM values of pulsars lying inside a region denoted by two circles of radius of 5.5 and 6.5 kpc from the galactic center. In the lower plot the region is delimited by circles of 6.5 and 7.5 kpc. The RM values are compared to distances and the DM values of the pulsars. The magnetic field strength is inferred in the top-right corners. Red markers indicate outliers. Plot is taken from H. Men *et al.* [57].

Figure 2.2 (taken from [57]) shows the RM-DM distributions of pulsars in two different regions fitted with equation (2.24). The deduced field strengths are seen in the top-right corners.

After the line-of-sight regular-field strength of the different regions is determined, an overall model consisting of several free parameters is imposed. The goal of the chosen model is to encompass all the field directions and their strengths in the different regions of the galaxy in the best possible way.

Deducing the GMF strength using RMs has its weaknesses. Firstly, electromagnetic waves traveling through random fields do not Faraday rotate [61]. Secondly, equation 2.24 is only valid if the regular magnetic field and the electron density n_e are uncorrelated [52]. However, if they are anti-correlated equation 2.24 underestimates the field, and thirdly, the field is further underestimated if there are field reversals that are not accounted for [52].

Using RM measurements, J.L. Han and G.J. Qiao [54], and R.G. Rand and A.G. Lyne [55] found the local regular field strength to be $1.4 \pm 0.2\,\mu$G.

Figure 2.3: The radio emission (contours) and magnetic field vectors from the M51 galaxy measured by the VLA [63] and Effelsberg [64] radio telescopes. The picture of the galaxy is from the Hubble Space Telescope (Graphics by [65]. Copyright: A. Fletcher and R. Beck/Hubble Heritage Team [66]). Figure taken from [60].

2.3.2 Synchrotron emission

Electrons from jets or supernova remnants radiate as they traverse the magnetic field of the galaxy [61]. Like RM discussed in the previous section, synchrotron emission is measured by radio telescopes. Figure 2.3 shows the radio emission from the M51 galaxy and the direction of its magnetic field. The emissivity [56] of an electron with energy E is given by

$$J(\nu, E) \propto B_{\perp}^{\mathrm{GMF}} \left(\frac{\nu}{\nu_{\mathrm{c}}}\right)^{1/3} f\left(x = \frac{\nu}{\nu_{\mathrm{c}}}\right), \tag{2.25}$$

where E is the energy of the electron, $B_{\perp}^{\mathrm{GMF}}$ is the perpendicular component of the GMF, and ν is the frequency of the radiation emitted. The function $f(x)$ is close to one for $x \to 0$ and zero when x approaches infinity. The critical frequency ν_{c} is defined as [56],

$$\nu_{\mathrm{c}} = \nu_{\mathrm{L}} \left(\frac{E}{mc^2}\right)^2, \tag{2.26}$$

where $\nu_{\mathrm{L}} = \left(eB_{\perp}^{\mathrm{GMF}}/2\pi m\right)$ is the Larmor frequency given by $\Omega/2\pi$, where Ω is defined in section 2.3.1. From the profile of equation (2.25) it is obvious that the emission peak is around $\nu \approx \nu_{\mathrm{c}}$. In

addition, equation 2.25 shows that the emissivity is a function of the perpendicular component of the galactic magnetic field. The synchrotron emission is a function of $J(\nu, E)$.

The total intensity of the synchrotron emission depends on the distribution of the electrons, n_e [56, 61]. The most common assumption is that the electron distribution has a power-law structure [56] of the form,

$$n_e(E)\,\mathrm{d}E = n_{e0}\left(\frac{E}{E_0}\right)^{-\gamma}\mathrm{d}E, \tag{2.27}$$

where n_{e0} is the normalization of distribution and γ is the spectral index. The *synchrotron emissivity* [56] is thus given by,

$$j_\nu = \int J(\nu, E)\, n_e(E)\,\mathrm{d}E, \tag{2.28}$$

where $J(\nu, E)$ is given by equation 2.25. In order to deduce the field strength another property is needed, namely the total energy density,

$$\epsilon_{\mathrm{tot}} = (1+k)\epsilon_{\mathrm{re}} + \epsilon_B, \tag{2.29}$$

where k is the ratio of the total energy of heavy nuclei and electrons [52, 67] and ϵ_B is the density of the magnetic energy [56]. The total kinetic energy density of the electrons, ϵ_{re}, is given by the integral [56, 67],

$$\epsilon_{\mathrm{re}} = \int n_e(E)\, E\,\mathrm{d}E. \tag{2.30}$$

One of two assumptions is usually made in order to deduce the magnetic field strength. The magnetic field is estimated either by assuming equipartition where the magnetic energy density is equal to the total electron kinetic energy density, or by minimizing the total energy density with respect to the magnetic field [56, 67].

The total kinetic electron energy density in equation (2.30) is usually obtained by using a fixed integration interval in radio frequency [56, 67]. By integrating over radio frequencies and minimizing the total energy density with respect to the field yields a field strength that is weaker than when equipartition is assumed [67]. However, as noted by Beck and Beck *et al.* (e.g [52, 67, 68]), the two assumptions can yield similar field strengths if the total kinetic electron energy, as in equation (2.30), is calculated by using a fixed integration interval in energy. By using a fixed integration interval in energy the *revised* average total field strength for both assumptions (see [67] for details) has the form,

$$B_\perp^{\mathrm{GMF}} \propto \left(\frac{I_\nu\,(K+1)}{L}\right)^{1/(\alpha+3)}, \tag{2.31}$$

where I_ν is the synchrotron intensity, L is the length of the region emitting radio waves, K is the ratio of proton and electron number densities, and $\alpha = (\gamma-1)/2$ is the spectral index of the synchrotron emission. Identical field strengths are obtained for the two assumptions when $\alpha = 1$ [67]. The synchrotron intensity is related to the synchrotron emissivity as,

$$I_\nu = L\int J(\nu, E)\, n_e(E)\,\mathrm{d}E = L\, j_\nu, \tag{2.32}$$

The synchrotron intensity and spectral index α are measured from the observations. The intensity of the synchrotron emission thus yields the average strength of the perpendicular component of the *total* galactic magnetic field [52].

As mentioned before, the polarization of the synchrotron emission also plays an important role in determining the field strength. It yields the average perpendicular component of the regular field [52]. In presence of regular field only, the synchrotron emission is highly polarized while depolarized emission indicates a fluctuating or a random field [56, 61].

While RM might possible underestimate the field, synchrotron emission measurements perhaps overestimate it [52]. A *local* total perpendicular field was estimated by E.M. Berkhuijsen in reference [52] to $6 \pm 2\,\mu$G from radio synchrotron data.

Next section reviews different models of the GMF found in literature and investigates their effects on propagation of the UHECRs.

Figure 2.4: Our galaxy with its named spiral arms. The sun is located about 30000 light years or 8.5 kpc away from the galactic center. Figure taken from [69].

2.4 Models of galactic magnetic field

Our galaxy consists of a spiral disk ($z = 0$) with a radius of 20 kpc and a surrounding halo with a large volume. A 2D drawing is shown in figure 2.4.

In the literature the different models of the GMF have the following main components (see e.g. [70, 71]):

- Large "regular" field. The regular fields penetrate the whole galaxy disk and its surrounding halo. In addition evidence exists for dipole and toroidal fields near the galactic center.
- Small turbulent (or non-regular) fields. The turbulent or random fields have a given coherence length and are distributed throughout the spiral arms.

The use of RM of pulsar light has yielded contradictory results and these components are described differently in different papers.

The regular field is said to be bi-symmetrical, denoted by BSS, if field reversals occur between the spiral arms (see e.g. [54, 72, 73, 74]) . The regular field is axis-symmetrical, denoted by ASS, when there are no field reversals between the arms (see e.g. [75] and references therein).

In all the models the regular field strength has a common structure where only the numerical values of the parameters and the form of a radial function differ. If sign reversal of the field between the spiral arms is assumed, the magnitude of the regular field is given by the function (see e.g. [51, 54, 74, 76, 77, 78, 79]),

$$B_{\text{disk}} = B_{\text{radial}} \cos(\theta - \beta \ln(r/\xi_0)). \tag{2.33}$$

Here θ is the azimuthal angle which rotates clockwise when viewed from the galactic north pole (see figure 2.5), ξ_0 is the distance to the field maximum and r is the galactocentric cylindrical radius. The model dependent function, B_{radial}, describes the field in the radial direction. β is dependent on the angle between the azimuthal component of the magnetic field and the field

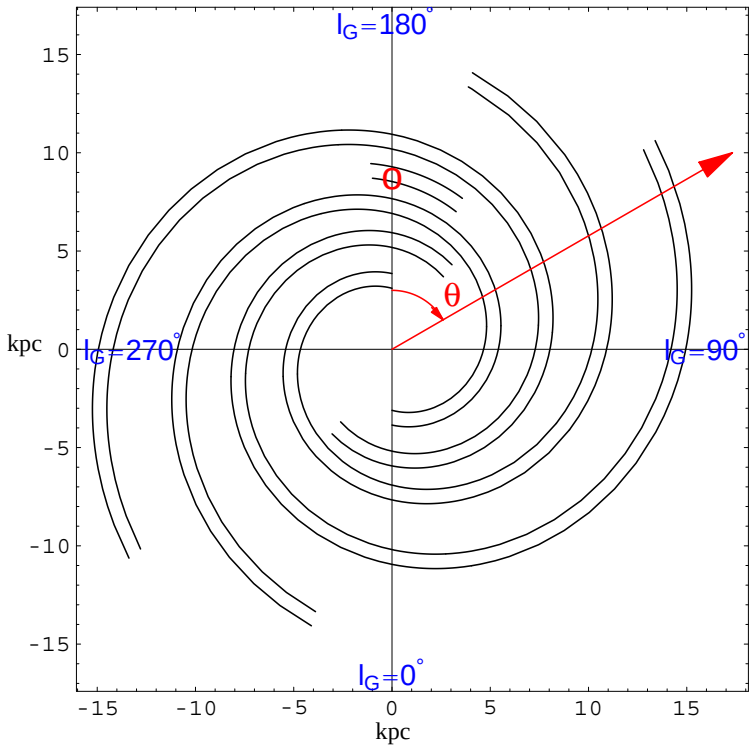

Figure 2.5: The coordinate system used in *models of the GMF in literature*. The Sun is located at the positive y-axis and the azimuthal angle θ rotates clockwise as viewed from the galactic north pole. $\theta = 0^\circ$ corresponds to galactic longitude of $l_G = 180^\circ$. The position of Earth is given by $R = (0, 8.5, 0)$kpc. In the next section, a new azimuthal angle ϕ is introduced so that $\phi = 0^\circ$ corresponds to $l_G = 0^\circ$. Plot is taken from Kachelrieß *et al.*[51]. Note that the plot shows the spiral arm structure from Wainscoat *et al.* [80].

itself, called the pitch angle p,

$$\beta = \frac{1}{\tan p} \tag{2.34}$$

The measurement of p is related to the rotation of the azimuthal angle and the logarithmic spiral structure of the galaxy given by (see e.g. [62, 73, 79]),

$$R_{\text{spiral}} = R_0 \exp(k\theta), \tag{2.35}$$

where R_{spiral} is the radius of the logarithmic spiral, R_0 is a scale radius and k is,

$$k = \tan p. \tag{2.36}$$

For our galaxy R_{spiral} increases in the counterclockwise direction (as viewed from the galactic north pole) i.e. for negative θ values [62, 79]. Hence, k has a negative value in all the models.

In the axis-symmetrical assumption where the field direction remains the same only positive values of the magnitude are retained.

The azimuthal and radial parts of the GMF are given by the pitch angle (see e.g. [51, 54, 76, 77, 78, 79]),

$$B_r = B_{\text{disk}} \sin p, \tag{2.37}$$

$$B_\phi = B_{\text{disk}} \cos p. \tag{2.38}$$

In agreement with the radio structure of the galaxy, as found by K. Beuermann *et al.* [81], the field magnitude in the halo is derived from the disk field in all the models [51]. It is described by the function [51],

$$B_{\text{halo}} = f(z)B_{\text{disk}}. \tag{2.39}$$

The field in the halo decreases as $|z|$ increases. This is ensured by the model dependent factor $f(z)$, usually an exponential with a certain scale height. In addition, as in the case with the disk field, the symmetry properties of the halo field are not clear [68]. The odd parity models where the field changes sign while going through the disk, are denoted with A. When the field has even parity, the model is denoted as S. Following the example of reference [51] the models used in this study are denoted by the initials of their creators. Basically, the models differ due to different values of the parameters described above.

Recently however, it was suggested that the GMF might have much more complex regular structure than a mere ASS or BSS configuration [57]. Likewise Han *et al.* [54] suggest that the GMF has a BSS structure but with both clockwise and anti-clockwise fields. The issue is additionally complicated by discrepancies in the estimations of the field strength. This discussion is far from finished. Here only models that are well established and that are in one or other way complementary, are used.

Concerning the random fields that are spread out in the galaxy, Tinyakov and Tkachev [82] calculated the deflections caused by the turbulent fields to be of the order of 3 to 30% of the deflections induced by the regular field. Most of the GMF models in literature neglect these fields.

In the next section a new coordinate system is defined.

2.4.1 Coordinate system

In all of the models found in literature the azimuthal plane angle θ runs clockwise as viewed from the galactic north pole (see figure 2.5). $\theta = 0^\circ$ corresponds to a galactic longitude of 180°.

In the present thesis a new coordinate system is used so that the new azimuthal angle, ϕ, runs counterclockwise as viewed from the galactic north pole, corresponding to the *galactic longitude* (see figure 2.6) i.e. $\phi = 0^\circ$ corresponds to a galactic longitude of 0°. The new (cylindrical) coordinates are defined as

$$\rho = \sqrt{x^2 + y^2}, \qquad \tan\phi = \frac{y}{x}, \qquad z = z. \tag{2.40}$$

Here x and y coordinates are in the galactic disk, and positive and negative z-directions point to the galactic north and south pole, respectively. ϕ runs counterclockwise when viewed from the galactic north pole, starting from the axis that corresponds to a galactic longitude of 0°. This axis is the new positive x-axis whereas in the models it is the negative y-axis. The position of the Sun is now $R = (-8.5, 0, 0)$ kpc. However, spherical coordinates are used to describe the dipole components of some of the GMF models

$$r = \sqrt{x^2 + y^2 + z^2}, \qquad \tan\phi = \frac{y}{x}, \qquad \cos\theta = \frac{z}{r}. \tag{2.41}$$

As noted in the previous section, the measurement of p is related to the rotation of the azimuthal angle and the logarithmic spiral structure of the galaxy [62, 79]. In the new coordinates, equation (2.35) is changed to

$$R_{\text{spiral}} = R_0 \exp\left(k\phi\right), \tag{2.42}$$

where $k = \tan p$. As both ϕ and R_{spiral} increase in the counterclockwise direction (as viewed from the galactic north pole), k is positive in the new coordinates. In section 2.4 (and in the models) the pitch angle is measured from magnetic field vector to the azimuthal magnetic field component pointing in the clockwise direction. With the new azimuthal plane angle ϕ defined here, the

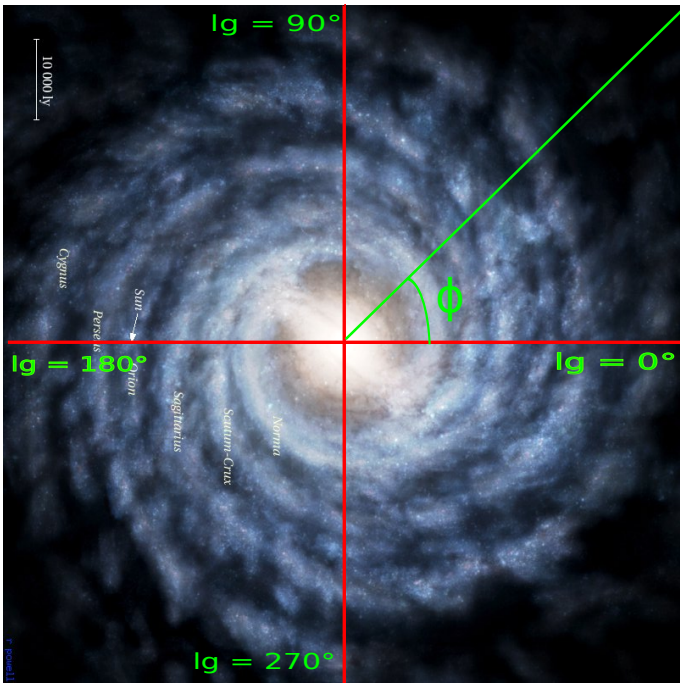

Figure 2.6: The coordinate system used in this work. The galactic center is at the origin. The red horizontal axis is the x-axis and the sun is located at $x = -8.5\,\mathrm{kpc}$ (marked with text and arrow). The vertical red axis is the y-axis. The angle ϕ starts at the positive x-axis and rotates anticlockwise as viewed from the galactic north pole. The underlying picture of the galaxy is taken from [69].

pitch angle is measured from the field vector to the azimuthal component that now points in the counterclockwise direction. This yields,

$$p_{\mathrm{new}} = -180^{\circ} - p_{\mathrm{model}}, \tag{2.43}$$

where p_{model} is given by the models. Here $\tan(p_{\mathrm{new}})$ or k is positive. This causes a sign change of β in equation (2.34) effectively changing the overall field direction. This is corrected by rewriting equation (2.33) as

$$B^{\mathrm{new}}_{\mathrm{disk}} = B_{\mathrm{radial}} \cos(\phi - \beta \ln(\rho/\xi_0) - \pi). \tag{2.44}$$

In Cartesian coordinates the field is given by,

$$\begin{aligned} B^{\mathrm{new}}_x &= (x \sin p_{\mathrm{new}} - y \cos p_{\mathrm{new}})\, B^{\mathrm{new}}_{\mathrm{disk}}\, f(z) \\ B^{\mathrm{new}}_y &= (y \sin p_{\mathrm{new}} + x \cos p_{\mathrm{new}})\, B^{\mathrm{new}}_{\mathrm{disk}}\, f(z) \end{aligned} \tag{2.45}$$

The reviewed models in the next section are expressed in the new coordinates defined in this work.

2.4.2 Stanev model

Many models in literature use the models suggested by Stanev [76] as a starting point. Stanev investigates the proposed field structures by studying the deflections and anisotropies of simulated particles. The consequences of the GMF models for any search for sources are also discussed.

Two "extreme" models are constructed in order to demonstrate the effects of the GMF, namely

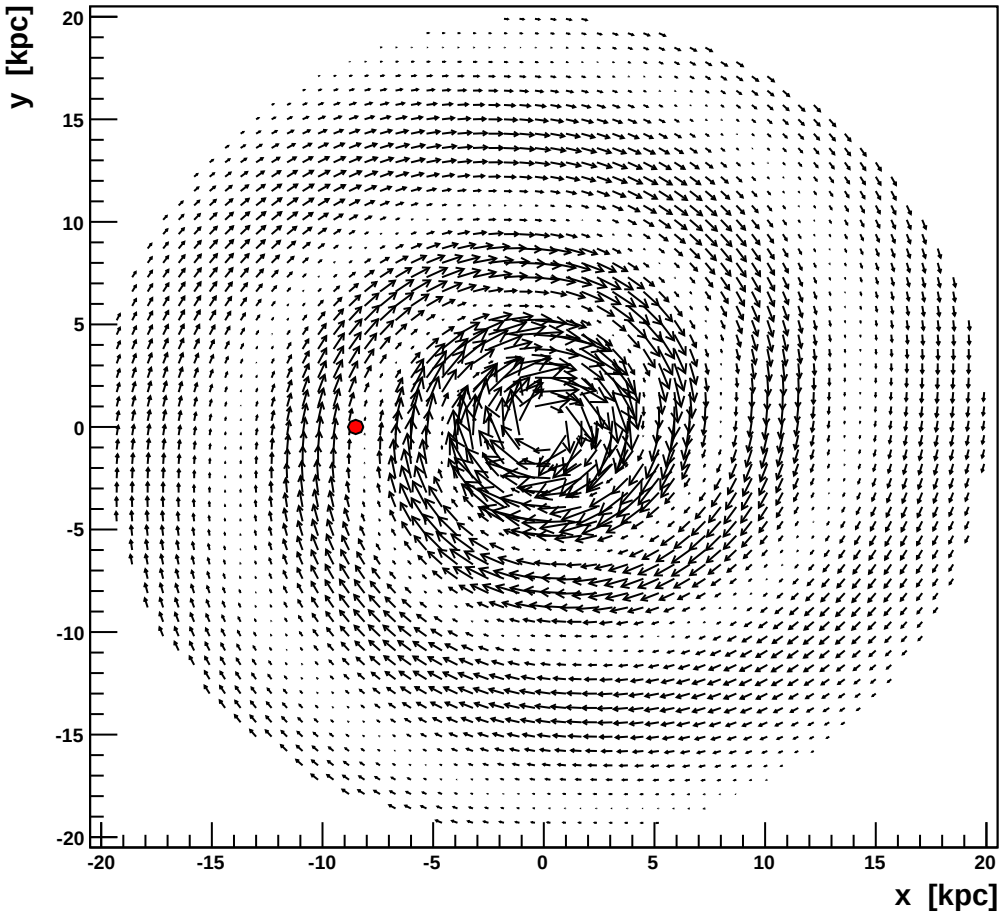

Figure 2.7: Vector field for the Stanev ASS-A model 0.1 kpc above the galactic disk. The vector length is proportional to the field amplitude and the size of the arrows is proportional to the field strength caused by $B = (b_x^2 + b_y^2)^{1/2}$. The Sun's location is indicated by the red circle.

the BBS-S and the ASS-A model[1]. B_{radial} is set to

$$\begin{aligned} B_{\text{radial}} &= \frac{\rho}{R}\,\mu\text{G}, & \rho &> 4\,\text{kpc}, \\ B_{\text{radial}} &= 6.4\,\mu\text{G}, & \rho &\leq 4\,\text{kpc}, \end{aligned} \tag{2.46}$$

where $R = -8.5\,\text{kpc}$ is the distance of the Sun from the galactic center. The pitch angle is -170° and ξ is 10.55 kpc. The strength of the halo field, regardless of the parity, is described[2] by an exponential with two scale heights,

$$|B_{\text{halo}}| = |B_{\text{disk}}| \exp\left(-|z|/z_0\right), \tag{2.47}$$

where z_0 is 1 kpc and 4 kpc for $|z| < 0.5$ and $|z| > 0.5$, respectively. In addition, a component of the magnetic field in the z-direction of magnitude 0.3 μG is added to the models. Thereby, the total number of models in reference [76] is increased to four.

[1] It was noted [78] that Stanev alternated the odd and even parity designations.
[2] The minus sign and the absolute value is missing in reference [76].

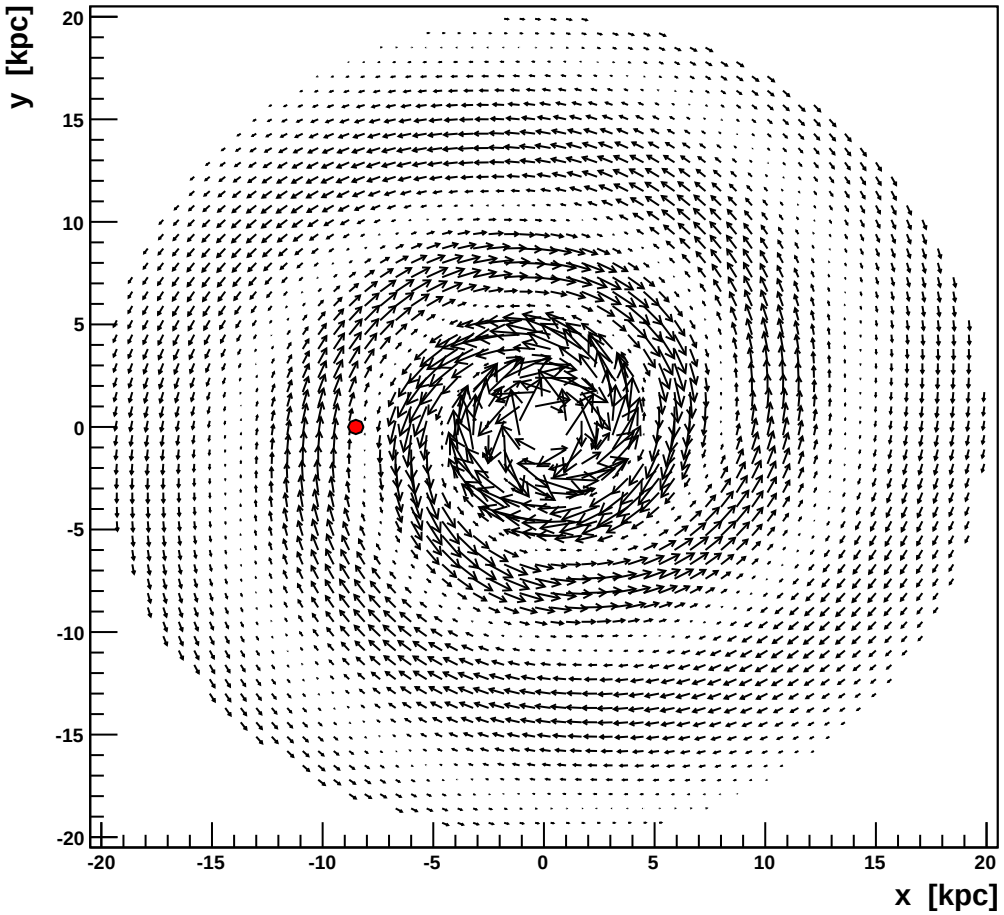

Figure 2.8: Vector field for the Stanev BSS-S model 0.1 kpc above the galactic disk. The vector length is proportional to the field amplitude and the size of the arrows is proportional to the field strength caused by $B = (b_x^2 + b_y^2)^{1/2}$. The Sun's location is indicated by the red circle.

Figure 2.7 and 2.8 show vector fields for the ASS-A and BSS-S configurations for $z = 0.1$ kpc above the galactic disk.

The field configurations are clearly visible. The spiral arms have the same field direction in figure 2.7 while in figure 2.8 it is clear that the field direction changes from arm to arm.

2.4.3 Tinyakov and Tkachev model

Tinyakov and Tkachev (TT) constructed two models [77] for two purposes:

- to check the correlation between UHECRs and BL Lacs after correcting for the GMF,
- to establish the charge composition of the UHECRs.

A BSS scenario with either an even or odd parity is used. The radial component of the field is described as

$$B_{\text{radial}} = B_0 \frac{\rho_0}{\rho \cos \phi'}, \tag{2.48}$$

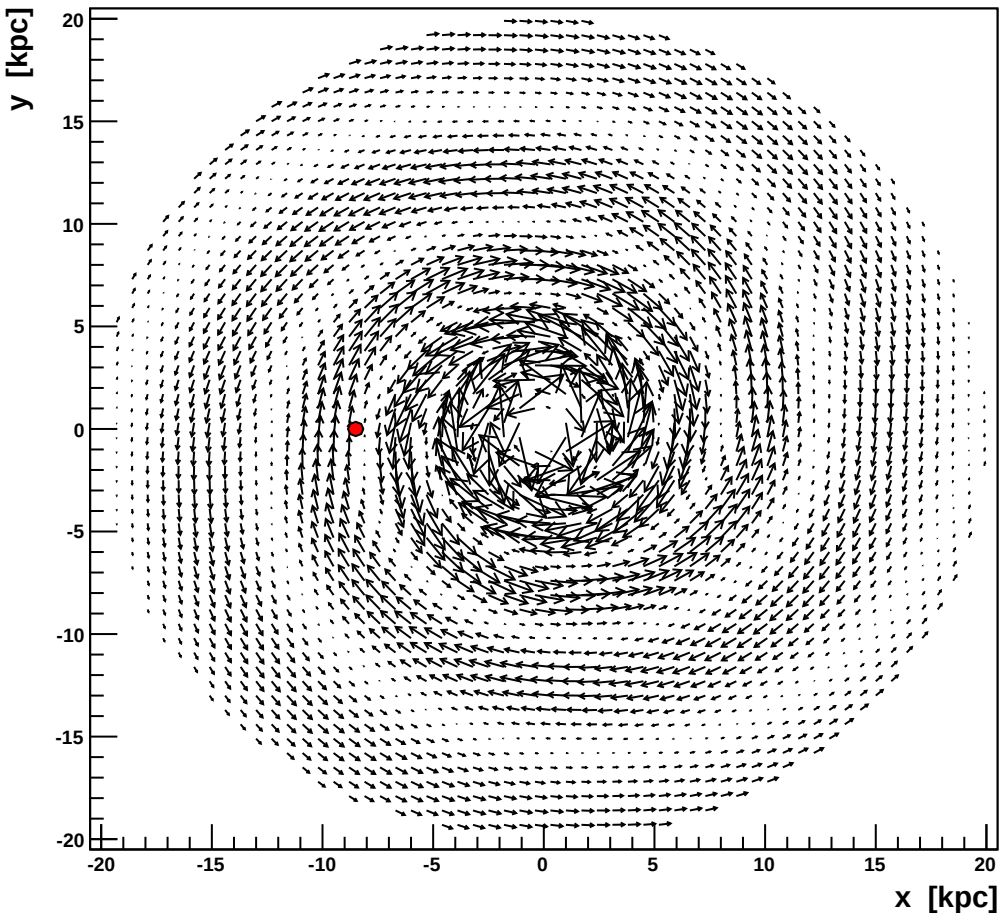

Figure 2.9: Vector field for the TT BSS-A model 0.1 kpc above the galactic disk. The vector length is proportional to the field amplitude and the size of the arrows is proportional to the field strength caused by $B = (b_x^2 + b_y^2)^{1/2}$. The Sun's location is indicated by the red circle.

where B_0 is the local field strength of magnitude 1.4 μG [54, 55] and ϕ' is a phase constant dependent on the pitch angle and the distance to the first field reversal,

$$\phi' = \ln\left(1 + \frac{d}{R}\right) / \tan p - \frac{\pi}{2}. \tag{2.49}$$

with $p = -172^\circ$ and $d = -0.5$ kpc. Like in the Stanev model B_{radial} is set to constant for $\rho < 4$ kpc. The halo field is determined by an exponential with a single scale height h of 1.5 kpc,

$$B_{\text{halo}} = \text{sign}(z) B_{\text{disk}} \exp\left(-|z|/h\right). \tag{2.50}$$

The scale height is chosen in accordance to [54, 73]. The disk field in equation (2.44) is now of the form,

$$B_{\text{disk}} = B_{\text{radial}} \cos(\phi - \beta \ln(\rho/R) + \phi' - \pi). \tag{2.51}$$

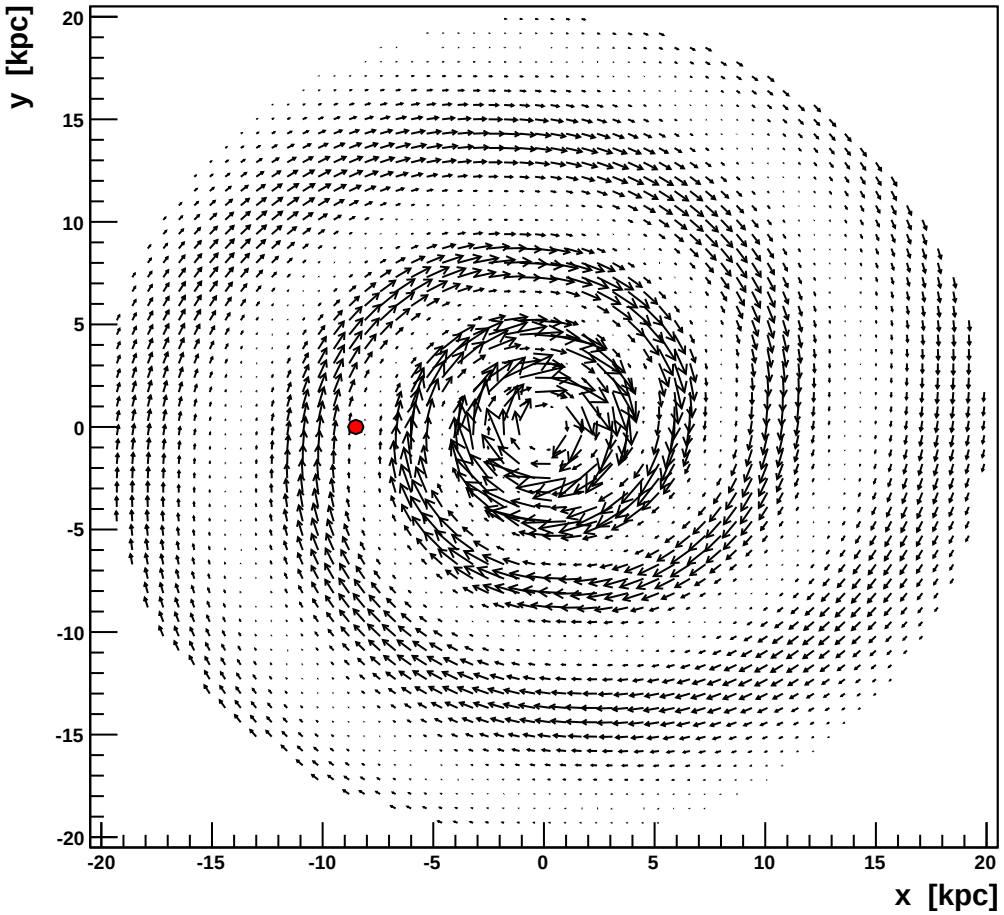

Figure 2.10: Vector field for the HMR ASS-A model 0.1 kpc above the galactic disk. The vector length is proportional to the field amplitude and the size of the arrows is proportional to the field strength, $B = (b_x^2 + b_y^2)^{1/2}$. The Sun's location is indicated by the red circle.

2.4.4 Harari, Mollerach, and Roulet model

Among other, Harari, Mollerach, and Roulet [78] deal with issues like deflections, composition, magnification/demagnification, and multiple images of sources. Two models were constructed, BSS-S and ASS-A, that differ in certain aspects from the Stanev and TT models. Firstly, the radial component is described by a function that not only decreases as $1/\rho$ for $\rho > 4\,\mathrm{kpc}$ but also disappears at the galactic center,

$$B_{\mathrm{radial}} = B_0 \frac{3R}{\rho} \tanh^3\left(\frac{\rho}{\rho_1}\right), \tag{2.52}$$

with $B_0 = 1\,\mu\mathrm{G}$. Here ρ_1 is set to 2 kpc. The halo field is also described by a hyperbolic function with two scale heights, z_1 (0.3 kpc) and z_2 (4 kpc),

$$B_{\mathrm{halo}} = \frac{1}{2\cosh\left(\frac{z}{z_1}\right)} + \frac{1}{2\cosh\left(\frac{z}{z_2}\right)}. \tag{2.53}$$

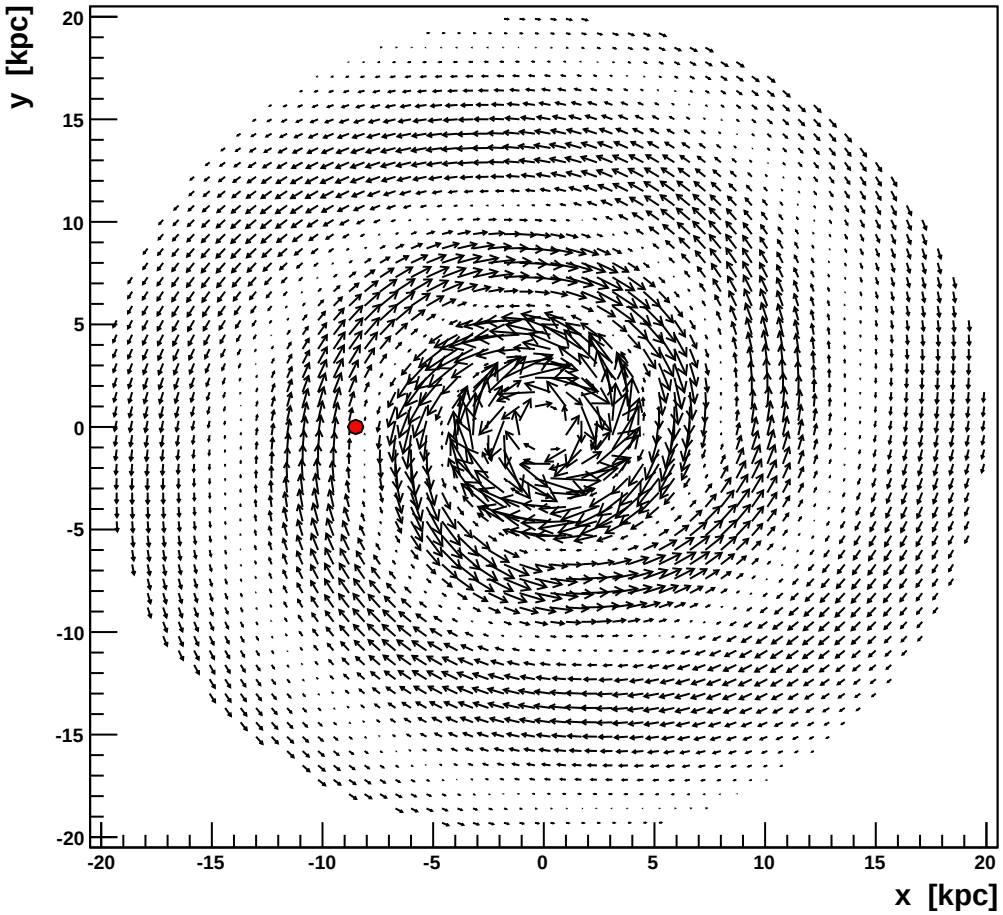

Figure 2.11: Vector field for the HMR BSS-S model 0.1 kpc above the galactic disk. The vector length is proportional to the field amplitude and the size of the arrows is proportional to the field strength, $B = (b_x^2 + b_y^2)^{1/2}$. The Sun's location is indicated by the red circle.

The halo field in the ASS-A model has an additional hyperbolic factor, $\tanh(z/20\,\mathrm{pc})$ that takes into account the odd parity. Other parameters are identical to the ones in the Stanev model.

In figures 2.10 and 2.11 the fields disappear at the galactic center in accordance with equation (2.52).

2.4.5 Kachelrieß, Serpico and Teshima model

For a directional and composition analysis Prouza and Šmída [79] constructed an elaborate model containing poloidal, toroidal, and turbulent field components. The disk field is modeled as for the Stanev model with a clockwise rotating θ while the poloidal and toroidal components are given in ordinary spherical coordinates. Some aspects of this model were modified by Kachelrieß, Serpico, and Teshima (KST) [51]. Here, this modification of the Prouza and Šmída (PS) model is denoted as the KST model.

In the KST model the disk field is defined as in equation (2.51), i.e. as in the TT model. For the halo field component the KST model uses an exponential with a single scale height of 0.2 kpc.

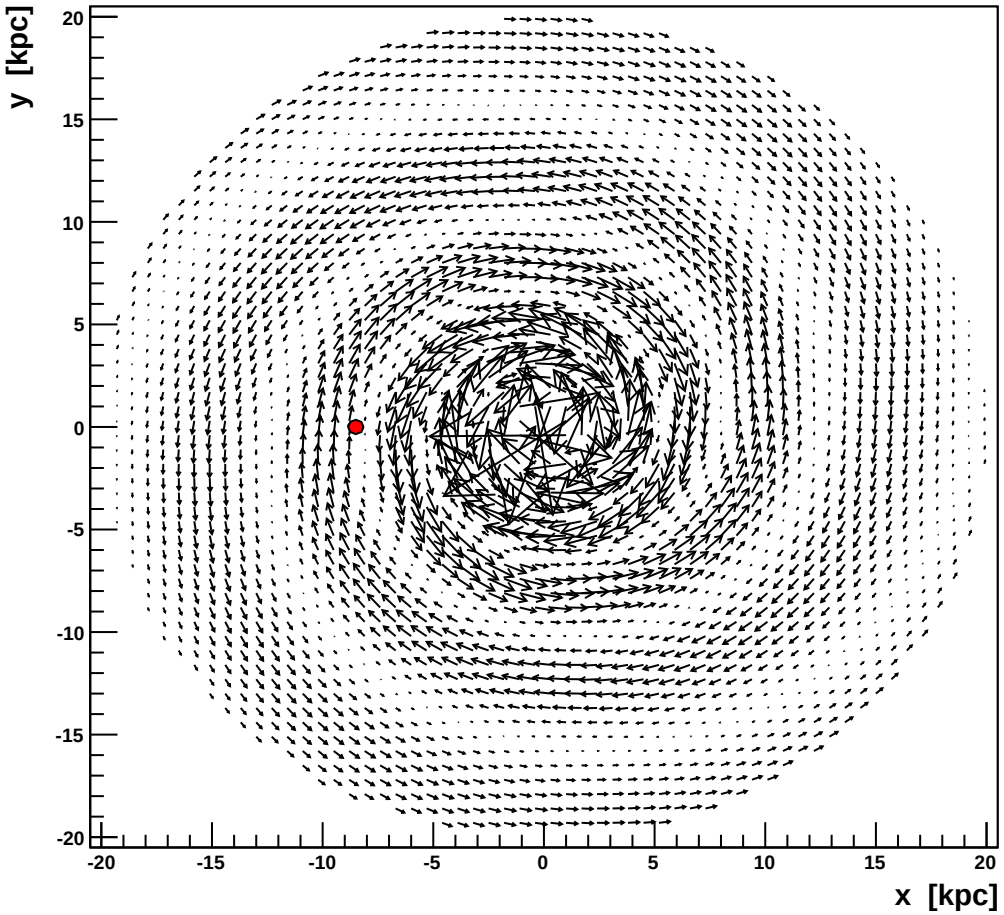

Figure 2.12: Vector field for the KST BSS-S model 0.1 kpc above the galactic disk. The vector length is proportional to the field amplitude and the size of the arrows is proportional to the field strength caused by $B = (b_x^2 + b_y^2)^{1/2}$. The Sun's location is indicated by the red circle.

The Cartesian components of a circular toroidal field are given by [51, 79],

$$B_x = -B_\mathrm{T}\,\mathrm{sign}(z)\sin\phi, \tag{2.54}$$

$$B_y = B_\mathrm{T}\,\mathrm{sign}(z)\cos\phi, \tag{2.55}$$

with B_T as modified by KST,

$$B_T = B_{\mathrm{T,max}}(\rho)\frac{1}{1+\left(\frac{|z|-H}{P}\right)^2} \tag{2.56}$$

where $H = 1.5\,\mathrm{kpc}$ is the height of the maximum above the galactic plane, $P = 0.3\,\mathrm{kpc}$ is the Lorentzian width. $B_{\mathrm{T,max}}(r)$ is given in terms of Heaviside step functions,

$$B_{\mathrm{T,max}} = 1.5\mu\mathrm{G}\left[\Theta\left(R_0-\rho\right)+\Theta\left(\rho-R_0\right)\exp\left(\frac{R_0-\rho}{R_0}\right)\right] \tag{2.57}$$

where R_0 is 8.5 kpc. Relation (2.57) ensures that the toroidal field vanishes for large values of ρ.

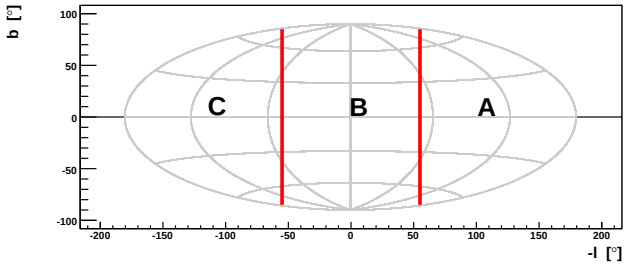

Figure 2.13: The three regions divided according to the galactic longitude l. Region A ($l < -55°$), region B ($-55° < l < 55°$), and region C ($l > 55°$).

This is in accordance with the fact that the toroidal field does not exist outside the solar circle [51, 83].

In order to take into account the existence of a local field of 0.2 to 0.3 μG pointing in the z-direction (see [54]), dipole components given in spherical coordinates were added in the PS model. As noted in section 2.4.1, equation (2.41), dipole components are described by *spherical coordinates*. In the KST model the dipole components are given by [51, 79],

$$B_x = -\frac{3\mu_G}{2r^3}\sin 2\theta \cos\phi, \tag{2.58}$$

$$B_y = -\frac{3\mu_G}{2r^3}\sin 2\theta \sin\phi, \tag{2.59}$$

$$B_z = -\frac{\mu_G}{r^3}(3\cos^2\theta - 1), \tag{2.60}$$

where μ_G is the magnetic momentum. A singularity is clearly present at the galactic center in the equations (2.60). Thus, a sphere of radius 500 pc with $B_z = -100\,\mu$G is added at the center of the galaxy. In contrast, the PS model uses a cylinder of radius 50 pc and height 300 pc with a 2 mG field inside it.

Although the PS model includes turbulent field components these were discarded in the KST model. In addition both the KST and the PS model adopt a spiral arm structure as described by Wainscoat *et al.* [80]. Here this specific structure is omitted.

The field as predicted by the KST BSS-S model is seen in figure 2.12. The field is very strong in the inner region near the galactic center due to the presence of the powerful dipole field and the sphere of $B_z = -100\,\mu$G.

The KST BSS-S, HMR ASS-A, HMR BSS-S and TT BSS-A models are used in the following analysis. The goal is to establish at what energies cosmic ray astronomy is possible for the different GMF models. Following the example of [51, 78] this is done by obtaining the deflections and the extra-galactic exposure of a given cosmic ray experiment.

2.5 Magnetic Deflections

In order to get an idea about the effects of the GMF models on the cosmic ray propagation, particles with different energies and incoming directions are backtracked until the galactocentric distance of 20 kpc is exceeded. Due to the substantial information contained in the following plots it is convenient to divide the sky in three regions along the galactic longitude: $l < -55°$ (region A), $-55° < l < 55°$ (region B) and $l > 55°$ (region C) (see figure 2.13). The calculated deflections for different energies are shown in figures 2.14 to 2.17.

2.5.1 Backtracking

For ultra-relativistic particles in a quasi-static magnetic field B the equations of motions [49] are given by the Lorentz force (see appendix A),

$$\frac{\mathrm{d}\vec{x}}{c\mathrm{d}t} = \hat{n}, \tag{2.61}$$

$$\frac{\mathrm{d}\hat{n}}{c\mathrm{d}t} = \frac{qc}{E}\,\hat{n} \times \vec{B}. \tag{2.62}$$

Here $\hat{n}$ is the unit vector along the direction of flight [49] and E and q are the energy and charge of the ultra-relativistic particles. $s = ct$ is the length travelled by the particles.

The path of the incoming particles is obtained by integrating equations (2.62) for their corresponding anti-particles leaving Earth in the direction of the incoming particles [78, 84]. Hence, the last equation in (2.62) is rewritten as

$$\frac{\mathrm{d}\hat{n}}{c\mathrm{d}t} = -\frac{qc}{E}\,\hat{n} \times \vec{B}. \tag{2.63}$$

At time $t = 0$, $\hat{n}$ is just the direction of the outgoing anti-particle which is equivalent to the incoming direction of its corresponding particle. Integrating the direction of anti-particles forwards in time is thus equivalent to integrating the direction of the corresponding particles *backwards* in time. This is denoted as *backtracking* of particles.

Vector $\vec{x}$ at $t = 0$ is given by $\vec{x} = (-8.5, 0, 0)$ kpc, indicating the position of the Sun from the center of galaxy.

It is not possible to solve equation (2.63) analytically. Instead, the Runge-Kutta method is applied (for details see e.g. [85, 86]). Here the 5^{th} order Runge-Kutta method is used and equation (2.63) is integrated numerically in steps.

The size of the steps is either fixed or *adaptive*. Here adaptive stepsize is used. This yields small steps where the magnetic field is complex and thus a high degree of accuracy is achieved. Where the magnetic field is simpler larger steps are used without loss of accuracy.

Suitable integrators are found in reference [85]. Equations (2.63) are backtracked using the `odeint` routine [85] that includes the 5^{th} order Runge-Kutta method with adaptive stepsize control.

In the next section the cosmic rays are assumed to be protons. Each proton is assigned a *unique* initial direction at Earth given by galactic longitude and latitude. The galactic longitudes and latitudes are given in steps of 0.5° in the range $[-179.5^\circ, 179.5^\circ]$ and $[-89.5^\circ, 89.5^\circ]$, respectively. A total of 64800 directions are thus generated.

Starting from Earth protons are backtracked until they are a distance of 20 kpc away from the galactic center. This corresponds to the extent of the galaxy.

The deflections are subsequently calculated according to

$$\cos(\alpha) = \hat{n}_{\text{init}} \cdot \hat{n}_{\text{last}}, \tag{2.64}$$

where $\hat{n}_{\text{init}}$ is the (unique) initial direction of the particles at Earth and $\hat{n}_{\text{last}}$ is the backtracked position outside the galaxy.

In figures 2.14 to 2.17 in the next section the deflection α is plotted for each initial direction $\hat{n}_{\text{init}}$ (given by galactic longitude and latitude). Since the initial directions are unique there is only one deflection value for each direction. The deflections range from 0° to 180°.

The figures are plotted using $-l$ rather than l. This is done in order to plot results in galactic coordinates according to astronomical convention.

As pointed out in the introduction, cosmic rays suffer from energy losses while propagating through the Universe. In the local Universe, the energy loss length of cosmic rays with energies 0.1 EeV to 150 EeV, range from 4 Gpc down to 10 Mpc, respectively (see figure 1 in reference [49]). The energy losses of cosmic rays propagating in our galaxy (with its extent of only 20 kpc) are thus negligible. Hence, energy losses are not taken into account when protons are backtracked.

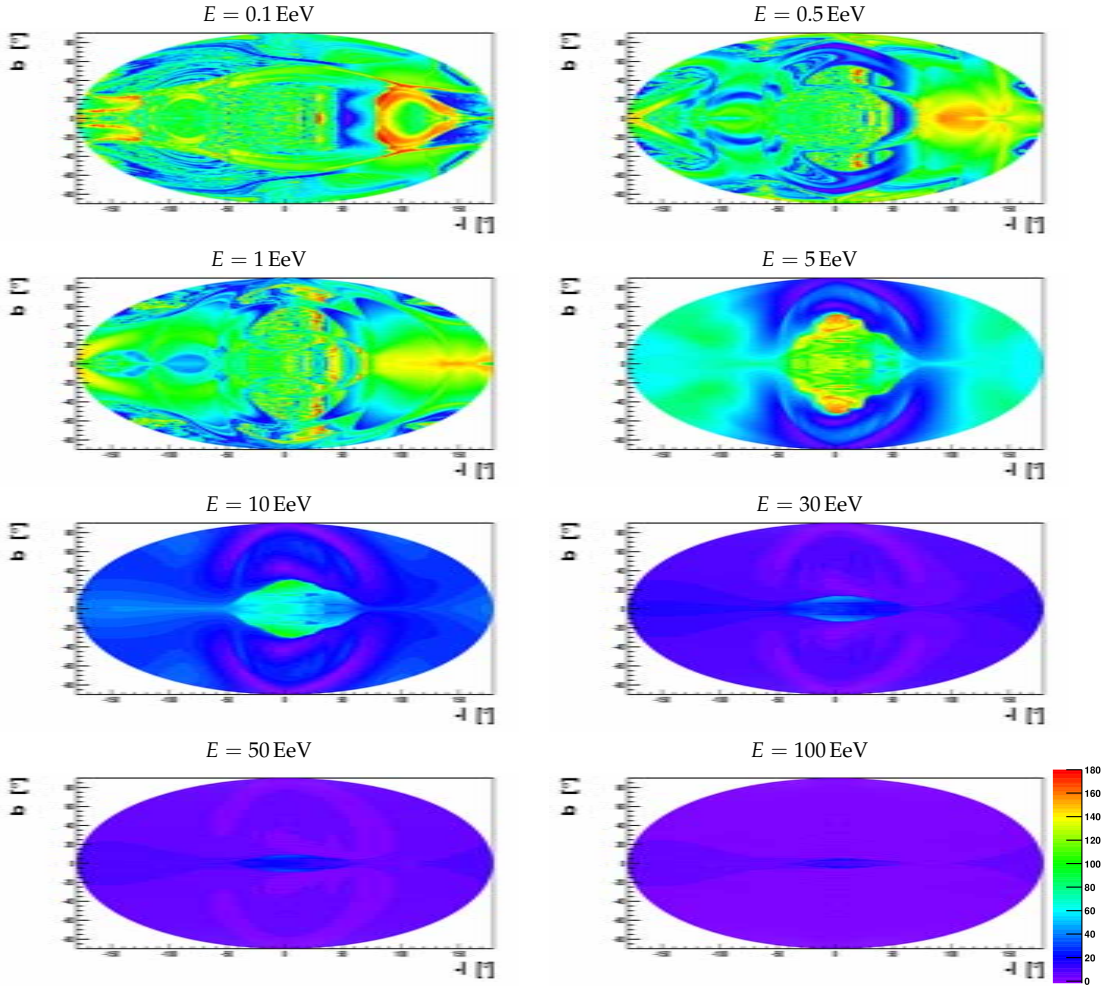

Figure 2.14: Deflection maps for HMR ASS-A model for different energies of the cosmic rays. Hammer-Aitoff projection is used.

2.5.2 HMR ASS-A model

Figure 2.14 clearly shows a symmetric structure where the deflections above and beneath the galactic plane are exactly the same. The average deflections for the lowest energies of 0.1, 0.5, and 1 EeV are in the range 81° to 84°. The distribution function for a large number of random isotropic deflections is given by

$$\frac{\mathrm{d}N}{\mathrm{d}\alpha} \propto \sin(\alpha)\,, \tag{2.65}$$

where N is the total number of deflections. This distribution peaks at the average deflection of 90°. The deflections for the 0.1, 0.5, and 1 EeV energies are thus compatible with random isotropic deflections. However, their corresponding deflection plots show large variations among them in the regions A, B, and C.

For 5 EeV the largest deflections occur in region B and the average deflections yield 47°, 70° and 57° for region A, B, and C respectively. The average deflection for the whole sky is 58°. There are thus again large variations between the three regions. This is also reflected in the Root Mean

Square (RMS) values given by,

$$\mathrm{RMS} = \sqrt{\int \alpha^2 \left(\frac{\mathrm{d}N}{\mathrm{d}\alpha}\right) \mathrm{d}\alpha}, \tag{2.66}$$

where $\mathrm{d}N/\mathrm{d}\alpha$ is the deflection distribution. The RMS for all regions is 31°. For region A, B, and C the values are 20°, 43°, and 21°, respectively.

The 5 EeV deflections might be considered to be of a transitional character, lying between random isotropic deflections and the deflections at higher energies. The deflections and the RMS values remain largest in region B for the 10 EeV and 30 EeV energies. From 30 EeV to 50 EeV the region of the largest deflections is shifted, from region B to C. However the difference in deflections is not significant. For 50 EeV the average deflections are 4.6° , 5.9°, and 6° for region A, B and C respectively, with an average deflection for the whole sky being 5.5°. For 100 EeV the numbers are 2.3°, 2.8°, 3.1°, for region A, B, and C, respectively. The average deflection for the whole sky is 2.7°. This is not surprising at all since the deflection is inversely proportional to energy.

2.5.3 HMR BSS-S model

In this model the field direction does not change at the disk, ensuring that the symmetric structure found in figure 2.14 is absent from figure 2.15. As for the HMR ASS-A model the deflections are random and isotropic for 0.1 EeV, 0.5 EeV, and 1 EeV energies.

For 5 EeV the highest deflections are found in region C while for larger energies ($E > 5$ EeV) the largest deflections are found in region A. The regional differences, however, are negligible for energies above 5 EeV. In addition, energies equal and above 5 EeV are deflected less than in the HMR ASS-A model. However, the differences between the two models in average deflections above 50 EeV are negligible as the deflections in both models are more and more inversely proportional to energy ($\alpha \propto 1/E$).

The difference with the HMR ASS-A model is clear. The deflections at higher energies are largest in region A rather than in region B and C, as in the HMR ASS-A case.

2.5.4 TT BSS-A model

The most striking feature of this model is the high degree of symmetry of the deflections. As in the HMR models the regional differences are large. The deflections for the 0.1 EeV and 0.5 EeV energies are compatible with random isotropic deflections, but the average deflections for these energies are much lower here than in the HMR models.

However, the deflections for 1 EeV deviate from a random isotropic behavior. While the average deflections of the regions are similar (in the range 46° to 51°), the RMS values differ significantly. Region A and C have RMS values of 31° and 39° i.e. the values are compatible with random isotropic deflections. In region B the RMS value is 16°.

At 5 EeV the deflections in region B are the largest. For the rest of the energies, region C is dominating yielding a regional B-C pattern for the movement of the highest average deflections. In addition the average deflections over the whole sky are lower than in the HMR models for all energies.

2.5.5 KST BSS-S model

Due to its strong dipole field in the vicinity of the galactic center the KST BSS-S model is distinctively different than the other models.

The massive strength of the dipole field ensures rather large regional variations at higher energies. While the average deflection over the whole sky is only 2.7° for 100 EeV the average deflections in region A, B, and C are 1.1°, 5.9°, and 1.4° respectively. Thus, here the deflection maps differ largely with the other models.

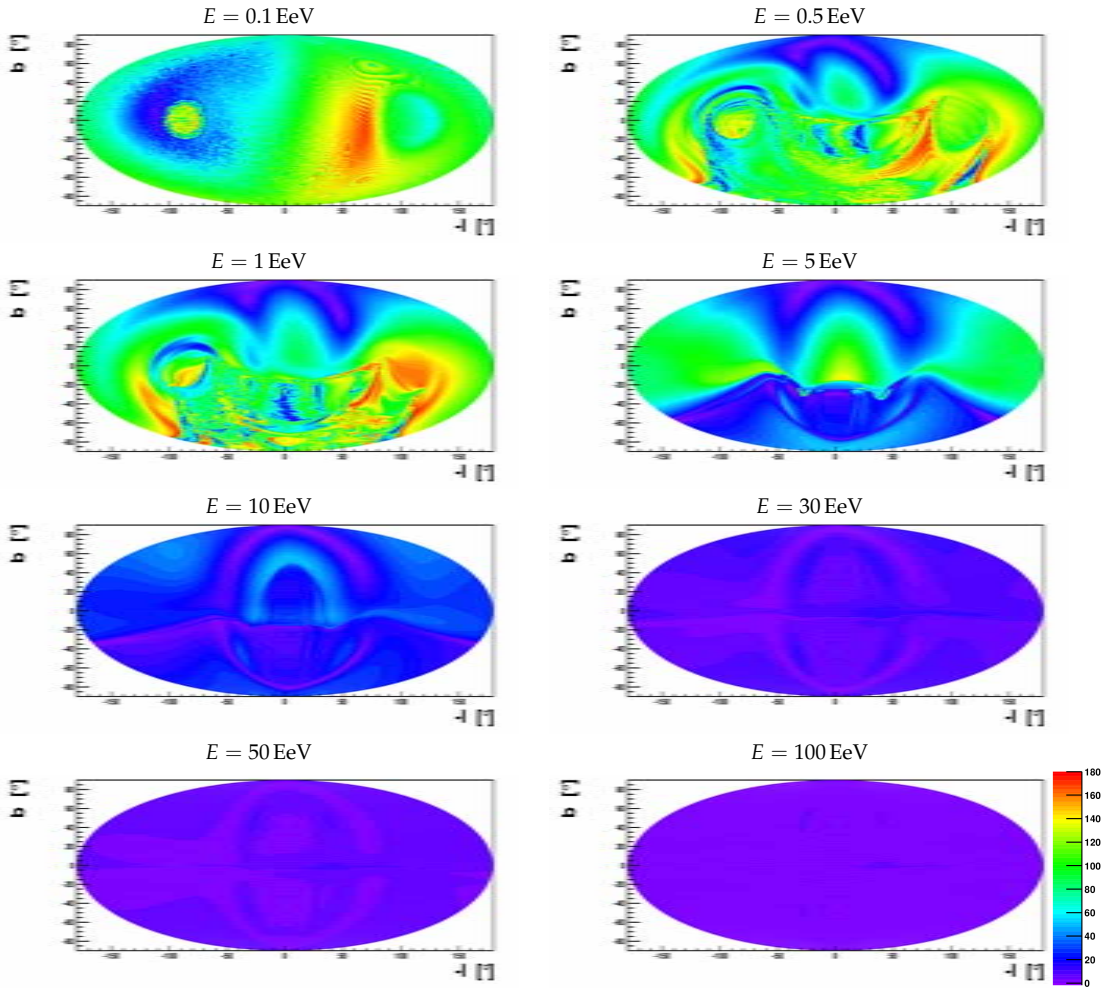

Figure 2.15: Deflection maps for HMR BSS-S model for different energies of the cosmic rays. Hammer-Aitoff projection is used.

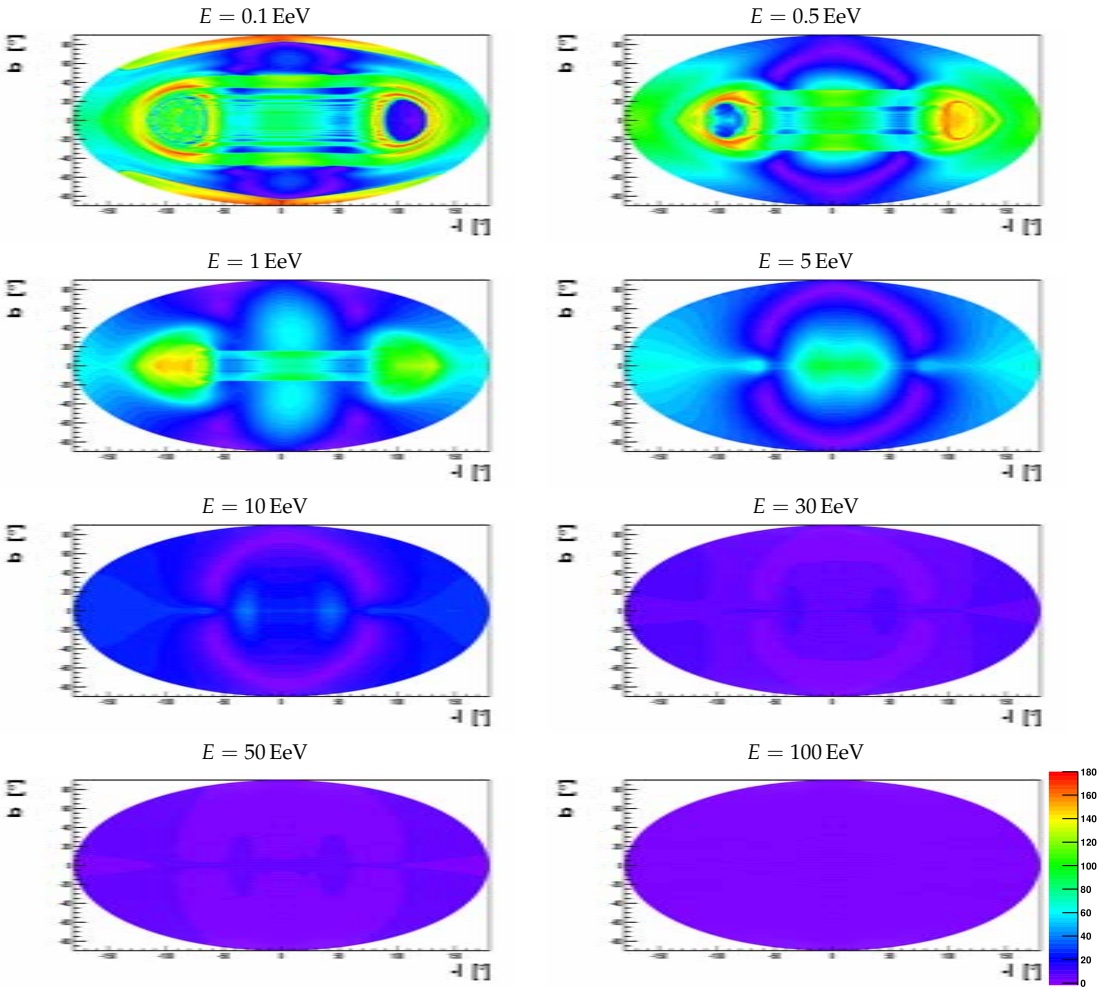

Figure 2.16: Deflection maps for TT BSS-A model for different energies of the cosmic rays. Hammer-Aitoff projection is used.

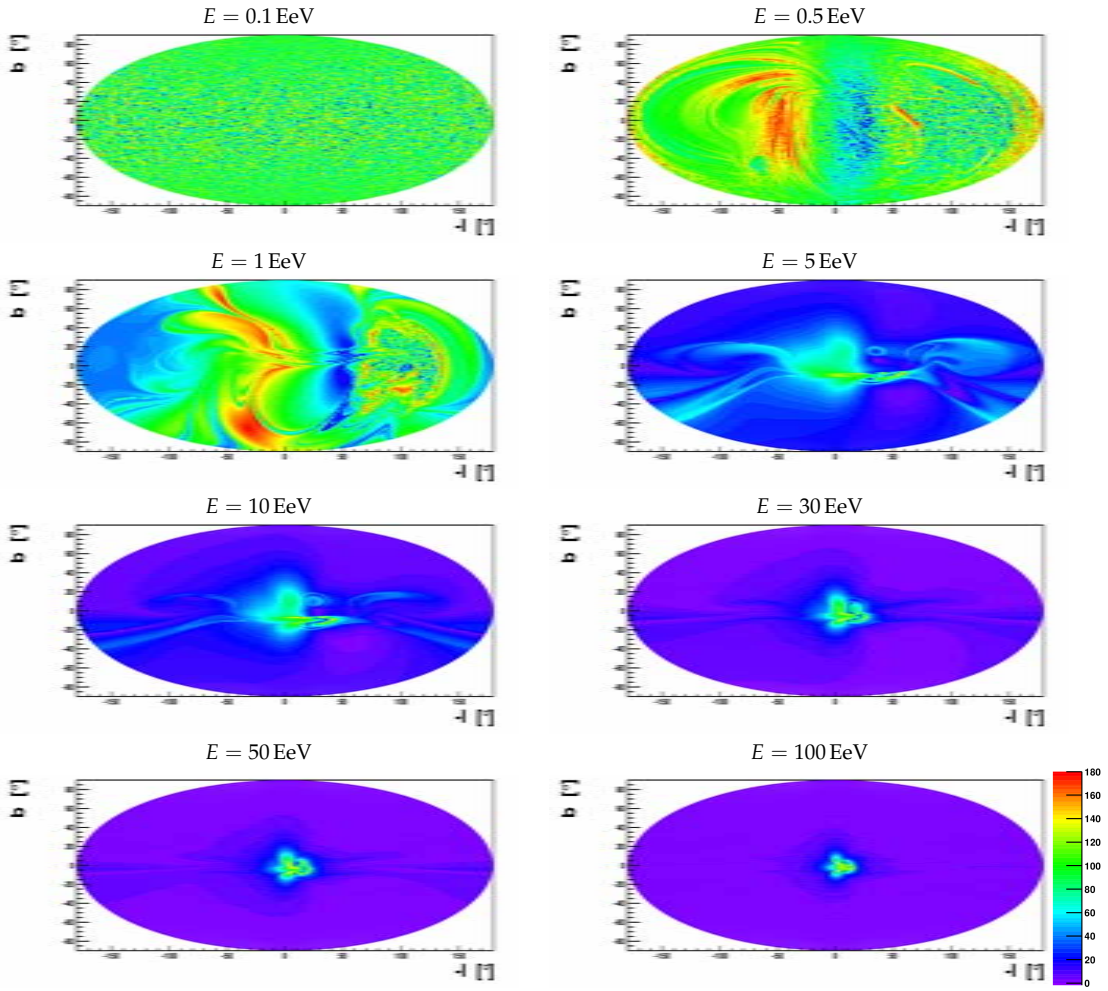

Figure 2.17: Deflection maps for KST BSS-S model for different energies of the cosmic rays. Hammer-Aitoff projection is used.

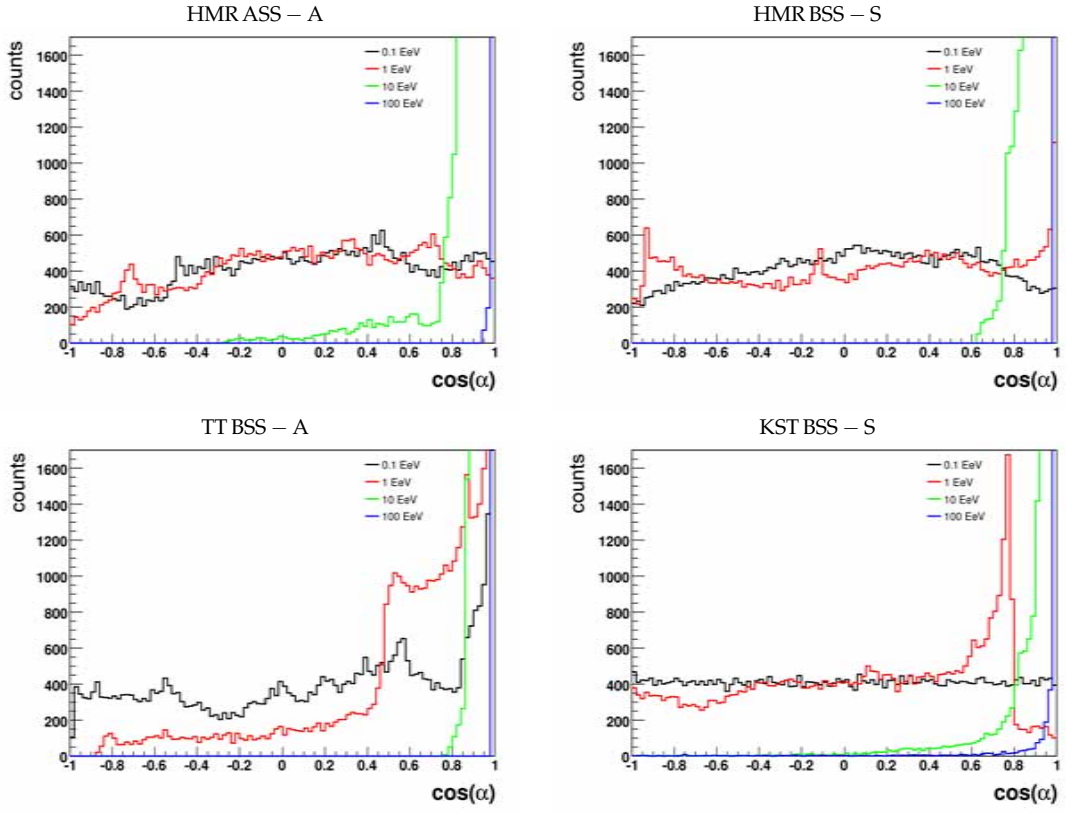

Figure 2.18: Deflection distributions for 0.1 EeV, 1 EeV, 10 EeV and 100 EeV for different models.

2.5.6 Deflection distributions

From the figures above it is clear why cosmic ray astronomy is only possible for the highest energies. This is also shown in figure 2.18 where the all-sky deflection distribution, $\mathrm{d}N/\mathrm{d}\cos\alpha$, for different models and energies (0.1, 1, 10 and 100 EeV) is presented.

As expected, the deflections vanish at higher energies. The average deflection over the whole sky for 100 EeV is 2.7°, 2.1°, 1.6°, and 2.7° for HMR ASS-A, HMR BSS-S, TT BSS-S, and KST BSS-S, respectively.

However, in the case of the KST BSS-S model there exist large regional differences. Region B, where the dipole field is present, has an average deflection of 5.9°, i.e. 3.2° higher than the overall sky average.

Going downwards to 10 EeV a shift to higher deflections occurs for all models. However, the deflections still peak approximately around 0° for all models except HMR ASS-A. In the latter model the deflections peak around 27°.

For 1 EeV the distributions begin to flatten for the HMR models. The KST BSS-S model has a rather flat distribution up to deflections around 60°. For the TT model the distribution shows that the majority of the deflections are in the range 60° or lower.

For 0.1 EeV a flat distribution is clearly seen for the KST BSS-S model as expected from random isotropic deflections. The distributions for the HMR models look relatively flat. The TT model however still shows a preference for small deflections and the distribution peaks below 37°. But overall this latter distribution is compatible with random deflections.

The distributions become more and more flat as the energies are reduced. As shown in equation (2.2) the gyroradius of the cosmic rays is $r_g \propto E/B$. For a given field strength the gyroradius becomes smaller for lower and lower energies. It is well known that a point is reached when the

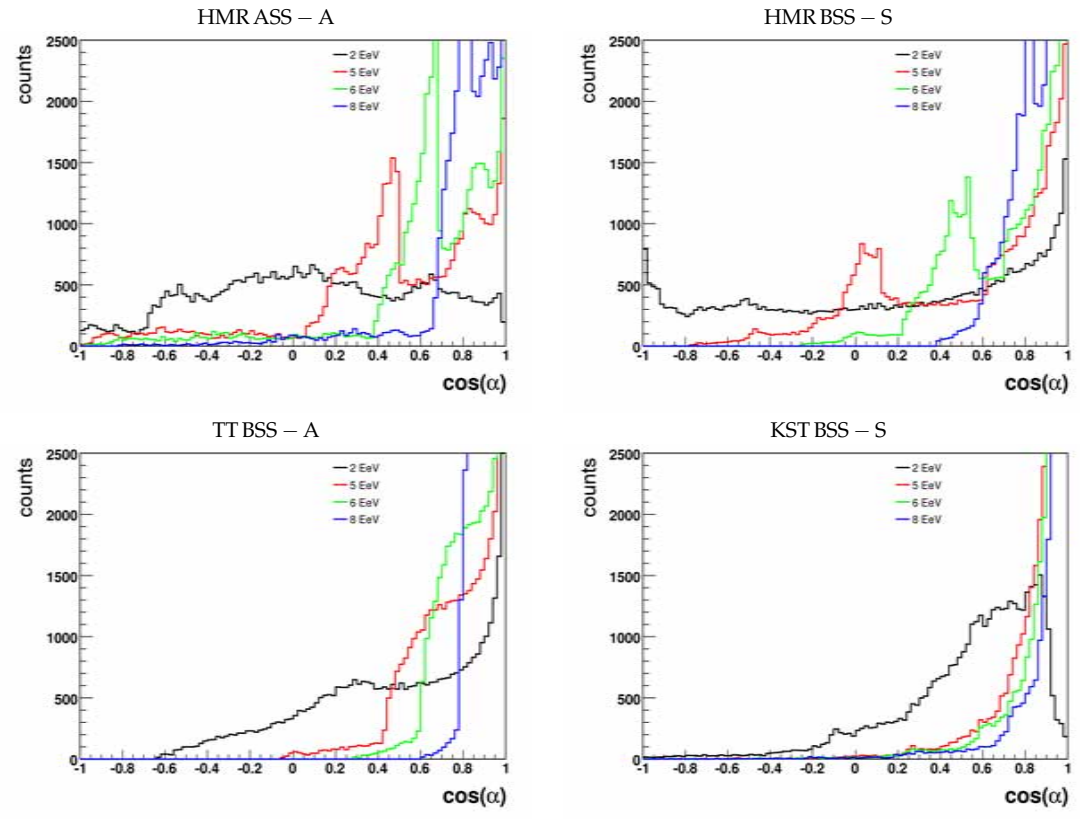

Figure 2.19: Deflection distributions for energies from the transitional range (2, 5, 6, 8 EeV) for different models.

gyroradius is smaller than the thickness of the galaxy, ensuring that the cosmic rays with lower energies are trapped. When arrival directions of these particles at Earth are backtracked out of the galaxy the exit direction, $\hat{n}_{\text{last}}$, is random and covers the whole sky uniformly.

Conversely, the distributions become more and more narrow as the energies increase. For extremely high energies the distributions should become delta functions located at 0° ($\cos\alpha = 1$). Clearly a transition as a function of energy takes place. Four energies (2, 5, 6, and 8 EeV) from this transitional region and their deflections are shown in figure 2.19. It is clear that the distributions shift towards lower deflections and it is also clear that there are large differences between the models.

The 2 EeV distributions for the HMR models are approximately flat while for the TT BSS-A and KST BSS-S the distributions are shifted towards smaller deflections. In fact, for the TT BSS-A and KST BSS-S models all the deflection distributions are shifted to the right and towards lower deflections when compared with the HMR models.

For the TT BSS-A model this is not surprising. It was shown in section 2.5.4 that the TT BSS-A model ensures the lowest overall average deflections for all the eight energies considered there.

Since the strength of the disk field B_{disk} is approximately the same for all models these differences might be explained by the different descriptions of the halo field, B_{halo}. The TT BSS-A and KST BSS-S models use exponentials in order to suppress the field strength for increasing $|z|$-values, while the HMR models use the hyperbolic function in equation (2.53). By using scale heights of $z_1 = 0.3\,\text{kpc}$ and $z_2 = 4\,\text{kpc}$, equation (2.53) decreases the field strength more slowly with increasing z-values as compared to the exponentials in the TT BSS-A and KST BSS-S models.

Figure 2.20 shows the average deflections and the RMS values for different models and energies. Up to 1.5 EeV the deflections are extremely large and fluctuating in mean value. The

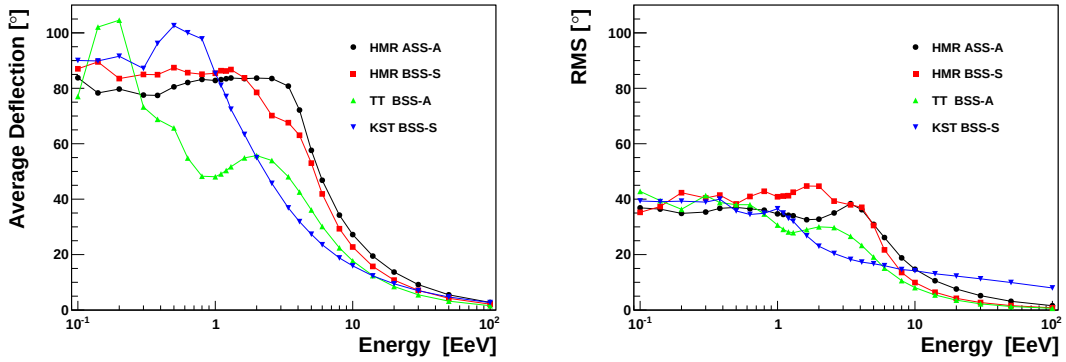

Figure 2.20: Left panel: The average deflection for different energies and models. Right panel: The Root Mean Square (RMS) measure of the deflection distributions for different models and energies.

exception is the TT model with its much sharper decline of deflection when energy is increased. The deflections are, if not totally, rather randomly isotropic and chaotic in this range. This is also reflected in the RMS plot. The distributions are highly spread up until 1.5 EeV.

In the transitional region in figure 2.19, the KST BSS-S and the TT BSS-S models produce more small deflections than the HMR models. This is also indicated in figure 2.20 where the average deflections for the TT BSS-A and KST BSS-S models are lower than the HMR models.

From 10 EeV and upwards the deflections are approaching a ballistic region for all models and follow the relation,

$$\alpha = \frac{D}{E}, \tag{2.67}$$

where D is deflection power in the units of $[\mathrm{EeV}\,^\circ]$. At 10 EeV the average deflection is around 20° for all the models. This yields,

$$\langle\alpha\rangle = 20^\circ \left(\frac{10\,\mathrm{EeV}}{E}\right) = 2^\circ \left(\frac{100\,\mathrm{EeV}}{E}\right), \tag{2.68}$$

yielding an average 2° deflection for 100 EeV protons.

However, for the ballistic region, differences appear in the RMS plot. The RMS values for the KST BSS-S model are substantially larger than in the other models. The RMS values of the KST BSS-S model become relatively constant in the transitional region and remain so in the ballistic region. For the KST BSS-S model thus the RMS values in the transitional and ballistic ranges are comparable. A difference with the other models is also seen in figure 2.18. The 100 EeV distribution for the KST BSS-S model clearly shows a relatively large tail. These differences are explained by the deflection discrepancies of the three regions. In region A and B the deflections are very small and vary very little, yielding an average deflection of order 1°. In region B the deflections are extremely varied ranging from 100° and more at the galactic center region to negligible deflections towards the galactic poles yielding an average deflection of order 6°.

If the HMR and the TT BSS-A models are describing the GMF sufficiently accurately, cosmic ray astronomy is possible for energies above 10 EeV. In this range the deflections are inversely proportional to the energy (see equation (2.68)). This is only partly true for the KST BSS-S configuration. Here the deflections in region A and C follow equation (2.68) while this equation is not valid for region B.

Overall, cosmic ray astronomy is thus feasible for energies above 10 EeV, provided that the field strengths of the models are accurate. As noted before, the field strengths of the models are derived by using RM measurements.

J.L. Han and G.J. Qiao [54], and R.G. Rand and A.G. Lyne [55], using RM measurements, calculated the *average* regular field along the line of sight to be $B^{\mathrm{GMF}}_{\mathrm{LS},\parallel} = 1.4\,\mu$G. Assuming this

value for the large scale component of the GMF, equation (2.9) yields a deflection of 10° for 100 EeV protons traveling 20 kpc. This is an overestimation as the field strength is reduced for increasing $|z|$-values.

E.M. Berkhuijsen, in reference [52], found an average local total perpendicular field of 6 μG using synchrotron measurements. Using this value, equation (2.9) yields a deflection of 64°. As noted in the previous sections, synchrotron emission measurements probably overestimate the field. However, if future measurements show that the total field is indeed of order 6 μG, then cosmic ray astronomy would be very difficult.

In this section the deflections are calculated for proton primaries with different energies. However, figures 2.21 to 2.24 are also valid for other primaries if the energies are corrected accordingly. By requiring that a given primary is deflected as much as a proton primary with a given energy E_{proton}, equation (2.63) yields

$$E_{\text{primary}} = \frac{Z_{\text{primary}}}{Z_{\text{proton}}} E_{\text{proton}} \tag{2.69}$$

where $Z_{\text{proton}} = 1$ is the proton charge and Z_{primary} the charge of the given primary. For iron $Z_{\text{primary}} = 26$. From equation (2.69) it is clear that a 26 EeV iron primary has the same trajectory as an 1 EeV proton primary. Equation (2.69) is generally true for all primaries and their trajectories. In the ballistic regime another approximation can be made, namely,

$$\alpha_{\text{primary}} \approx \frac{Z_{\text{primary}}}{Z_{\text{proton}}} \alpha_{\text{proton}} \tag{2.70}$$

The deflection maps for 100 EeV protons are thus equivalent to the deflection maps of 2600 EeV iron.

2.6 Extra-galactic exposure

Due to their geographical location, the daily rotation of the Earth, and the zenith angle dependence of the detector acceptance, cosmic ray experiments are more exposed to cosmic rays from some parts of the sky than others. Experiments located in only one hemisphere are for instance only with vanishing efficiency able to detect cosmic rays from other parts of the sky. By running experiments simultaneously on the northern and southern hemispheres the combined detectors are exposed to cosmic rays from every direction of the sky. However, assuming that there exists a 4π detector at Earth[3], the isotropic influx of cosmic rays at Earth[4] would nevertheless correspond to a non-uniform distribution of arrival directions on the extra-galactic sky[5] due to propagation effects through the GMF [51, 78]. In other words[6], sources do not contribute equally to the isotropic cosmic ray flux at Earth and cosmic rays from certain sources might not be detected at Earth [51, 78]. The distribution of the arrival directions on the extra-galactic sky yields the extra-galactic exposure.

While the maps in section 2.5 convey information about the deflections of the cosmic rays arriving at Earth from different parts of the sky, the extra-galactic exposure maps in this section show the contributions to the cosmic ray flux at Earth from different portions of the extra-galactic sky. Figures 2.21 to 2.24 show extra-galactic exposure maps for the GMF models and several different energies. The maps are obtained by backtracking 50 000 randomly generated arrival directions of protons at Earth, until they are 20 kpc away from the galactic center.

In this section, it is assumed that the cosmic rays are detected by a 4π detector[7] at Earth.

[3] A 4π detector has a uniform exposure to the total sky.

[4] In the backtracking picture this corresponds to the isotropic distribution of initial directions that are used for backtracking.

[5] In the backtracking picture this corresponds to the final directions of cosmic rays when they exit the galaxy.

[6] In the forward-tracking picture.

[7] The detector has a total sky coverage. The Auger coverage is not taken into account.

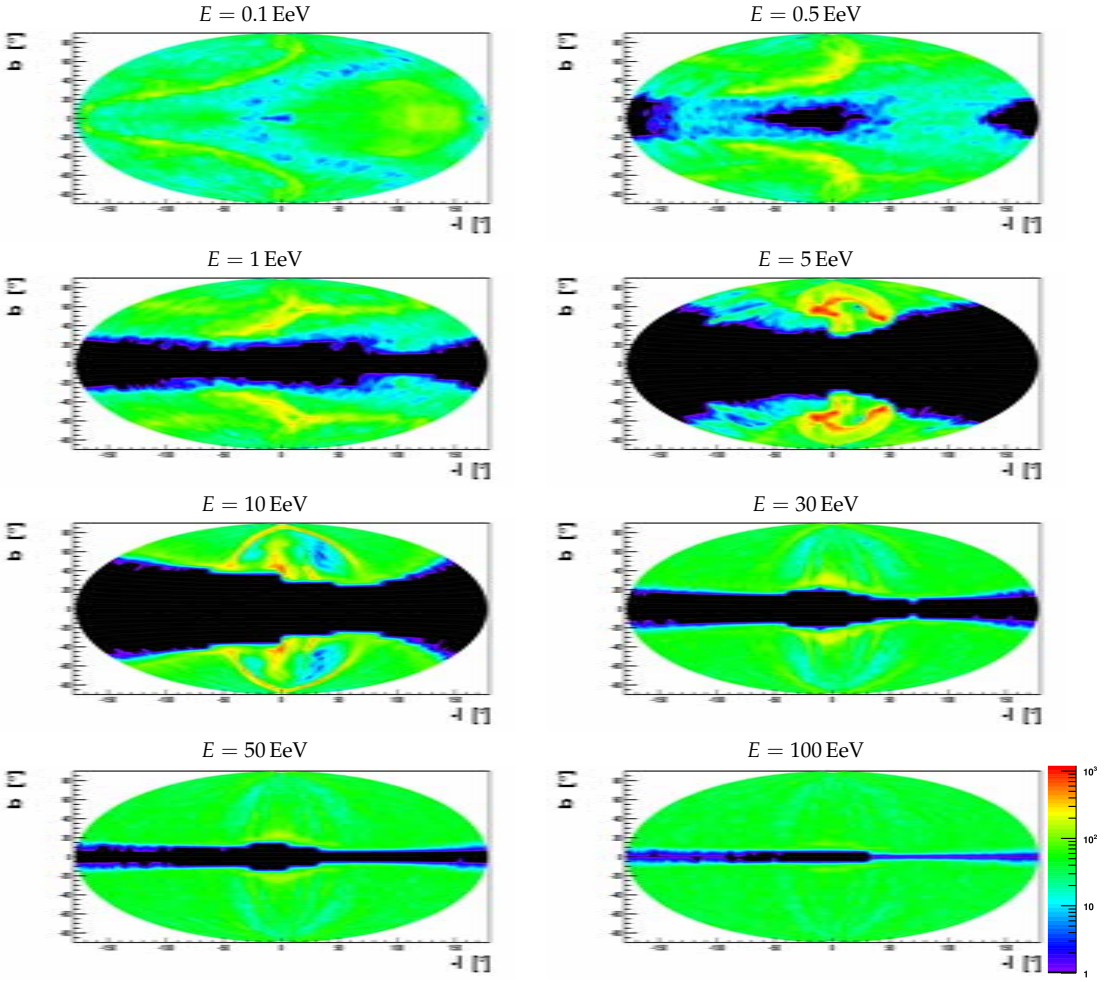

Figure 2.21: Extra-galactic exposure maps for the HMR ASS-A model for different proton energies in Hammer-Aitoff projection. 50 000 random arrival directions are backtracked until they are outside the galaxy and the corresponding final directions of the tracks are histogrammed.

2.6.1 HMR ASS-A model

The most obvious feature in figure 2.21 is the symmetry with respect to the z-axis. This is again due to the axis-symmetric configuration of the HMR-ASS-A model. Another striking feature is the almost isotropic distribution of the particle directions at 0.1 and 100 EeV. The distributions are isotropic for different reasons. At 0.1 EeV the deflections are large, ensuring that the particles are almost randomly spread all over the sky when backtracked. Physically it means that the cosmic ray isotropy at Earth is caused by particles that entered the galaxy isotropically and homogeneously. At 0.5 EeV two huge gaps appear in the central region around $z = 0$. Cosmic rays originating from extra-galactic sources in these regions are off limit for the detector placed at Earth's position, constituting blind spots for observers. The two gaps develop into a huge blind spot for energies up to 5 EeV. Now, the extra-galactic particles detected at Earth originate from sources in the vicinity of the galactic north and south pole only, making charged particle astronomy difficult at this energy. For 10 EeV and upwards the gap narrows down to a small region covering the whole vicinity of the galactic equator. Clearly, energies higher than 100 EeV are required in order to have access to particles from the whole extra-galactic sky. The arrival isotropy at very high energies is due to the low deflections of the particles. The particles just sim-

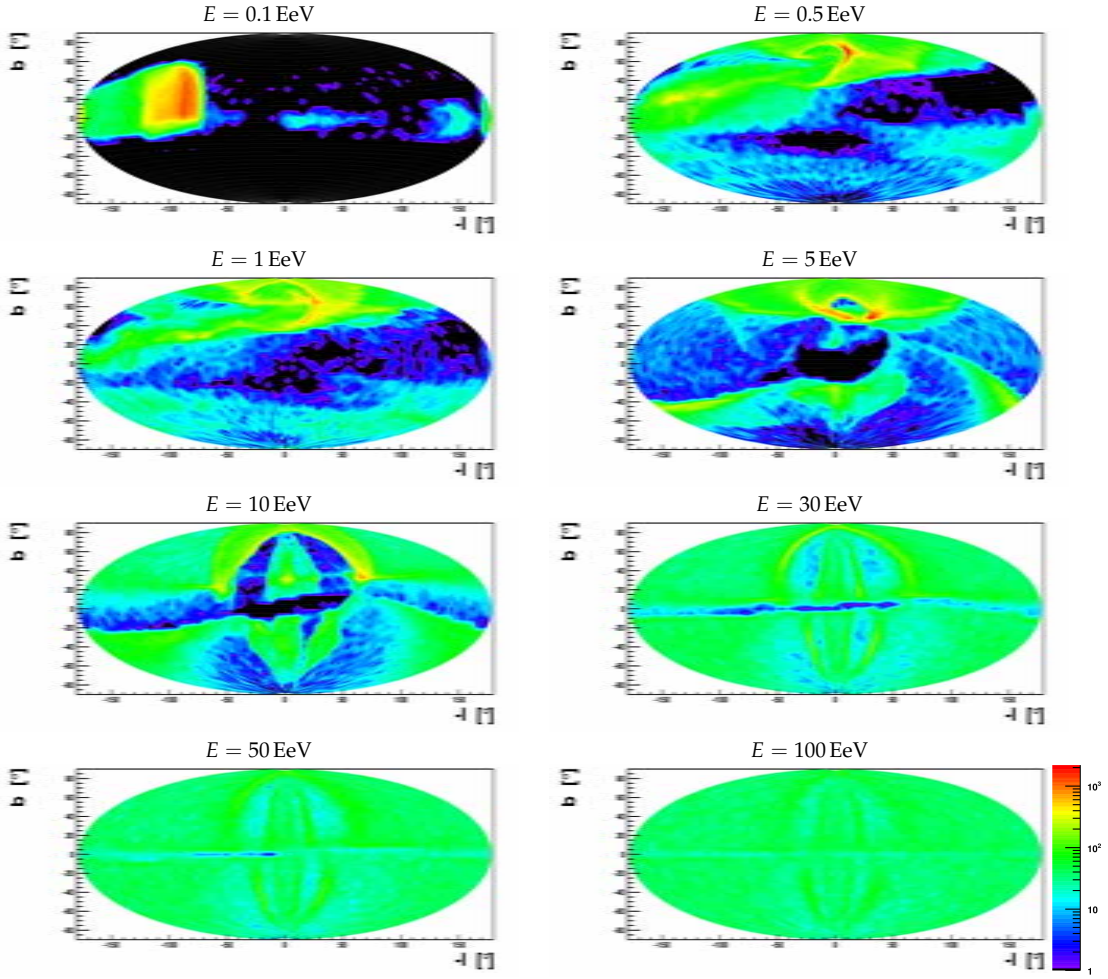

Figure 2.22: Extra-galactic exposure maps for the HMR BSS-S model for different proton energies in Hammer-Aitoff projection. 50 000 random arrival directions are backtracked until they are outside the galaxy and the corresponding final directions of the tracks are histogrammed.

ply traverse through the galaxy. Thus, for the HMR ASS-A model the particles from the whole extra-galactic sky are only accessible for very low or very high energies.

2.6.2 HMR BSS-S model

In contrast to figure 2.21, figure 2.22 shows a huge inaccessible region for 0.1 EeV. In this case, almost all the extra-galactic particles that are detected at Earth originate from sources in region C in the northern galactic hemisphere. In addition, the blind region is progressively narrowed down with increasing energy. This is a quite different behavior than in the HMR ASS-A model where the blind region does not exist at 0.1 EeV, is huge at 5 EeV, and small at 100 EeV.

As in figure 2.15 the symmetry is broken since the field along the z-axis does not change direction.

2.6.3 TT BSS-A model

With respect to the development of the blind region on the sky, the exposure maps in figure 2.23 are similar to those in figure 2.22. The blind region is largest for 0.1 EeV, gradually decreas-

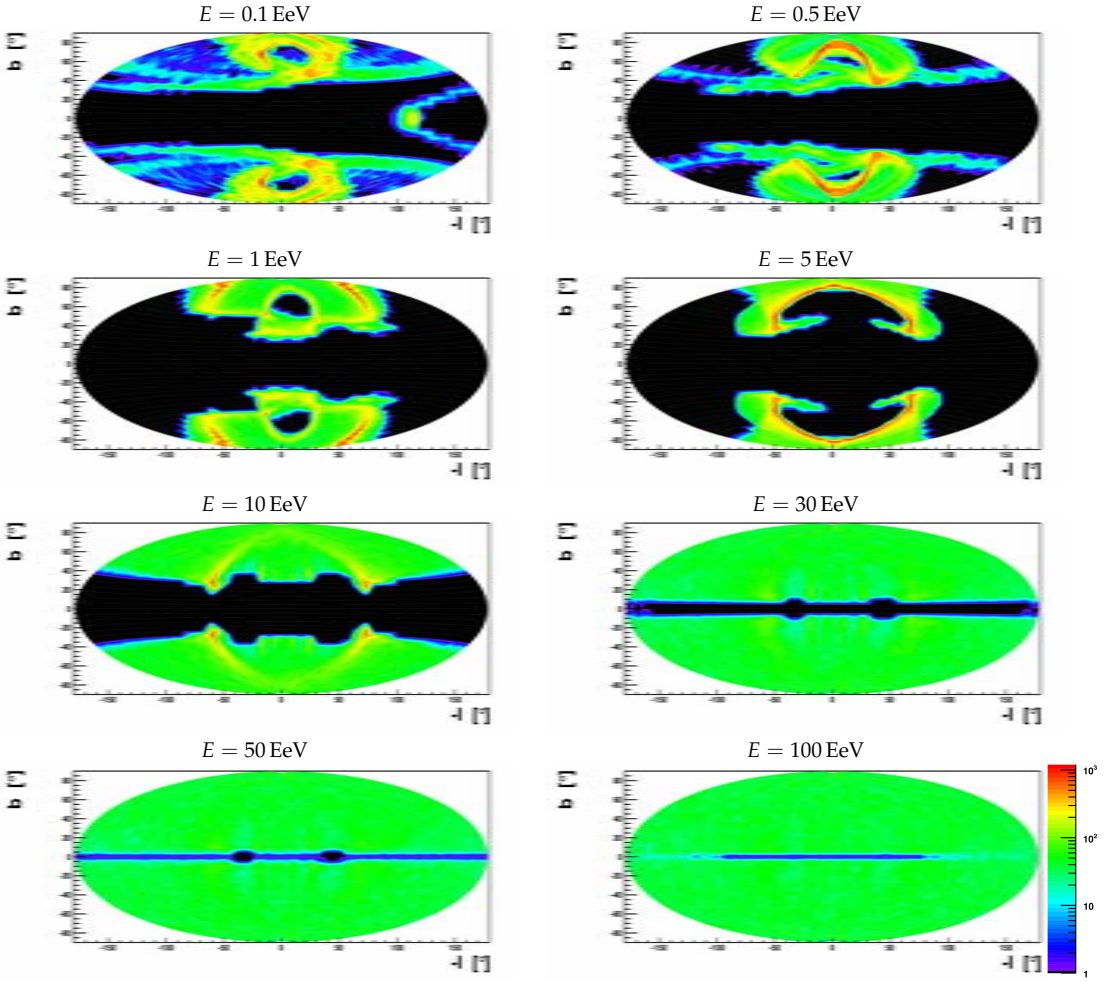

Figure 2.23: Extra-galactic exposure maps for the TT BSS-A model for different proton energies in the Hammer-Aitoff projection. 50 000 random arrival directions are backtracked until they are outside the galaxy and the corresponding final directions of the tracks are histogrammed.

ing with higher energy. Due to the field reversal at the disk the exposure maps are symmetric, resembling the ones in figure 2.21. This reversal also ensures that the distribution for higher energies is less isotropic than in the case of HMR BSS-S model.

2.6.4 KST BSS-S

The exposure maps for the KST model are truly unique due to its dipole field. The most striking feature is the significant size of the blind region around the galactic center from 30 EeV and upwards. For 0.1 EeV and 0.5 EeV the blind regions are located in the regions around the galactic north and south poles. At 1 EeV a transition takes place, and from 5 EeV and onwards the blind spot is contained in the region around the galactic center. The dipole field in equation (2.60) increases towards the galactic center as

$$B_z = -246\,\mu\mathrm{G}\left(\frac{r}{\mathrm{kpc}}\right)^{-3} \tag{2.71}$$

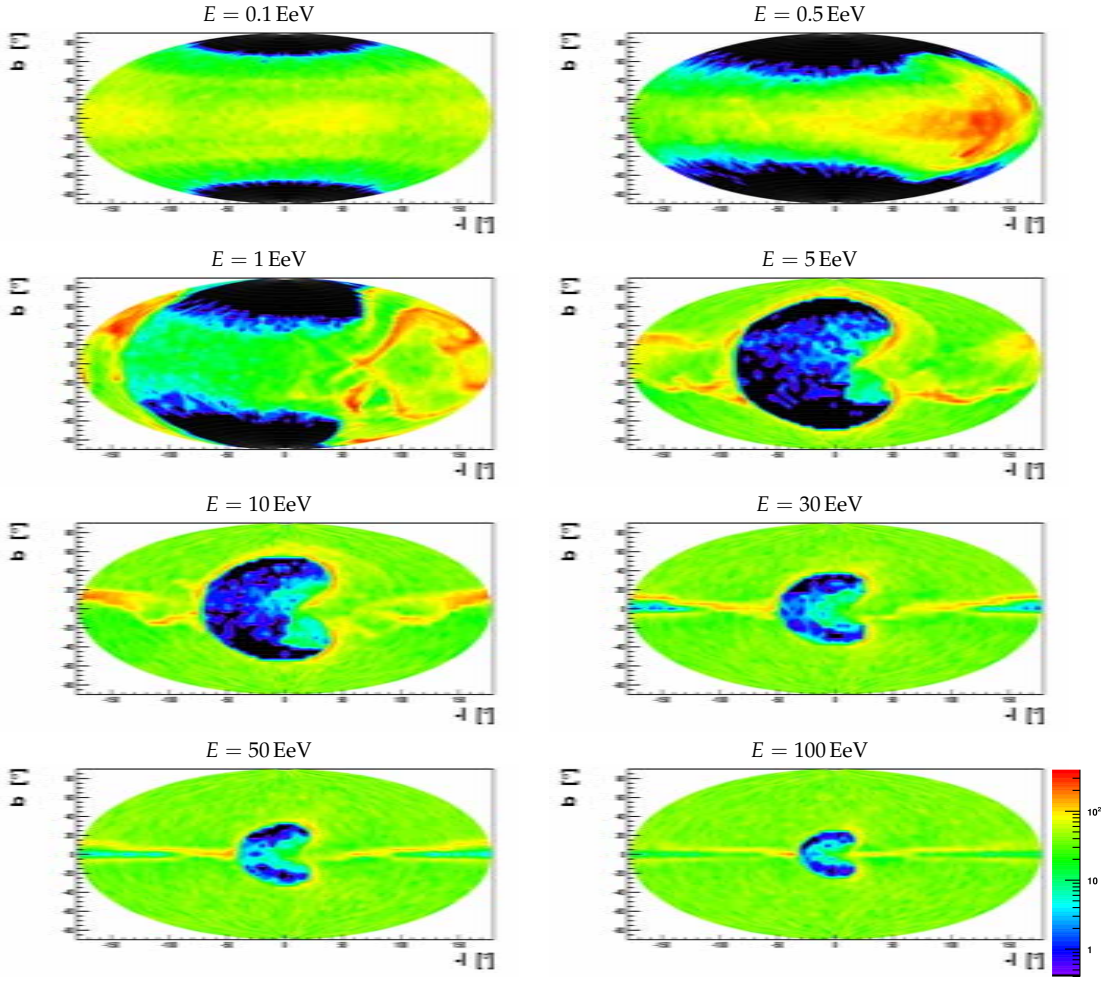

Figure 2.24: Extra-galactic exposure maps for the KST BSS-S model for different proton energies in Hammer-Aitoff projection. 50 000 random arrival directions are backtracked until they are outside the galaxy and the corresponding final directions of the tracks are histogrammed.

for $z = 0$ and $r^2 = x^2 + y^2$. This implies that even particles of large energies are significantly deflected.

From the plots for 30, 50, and 100 EeV it is clear that a high degree of isotropy prevails in region A and C.

2.6.5 Conclusion

The figures in sections 2.6.1 to 2.6.4 clearly show different degrees of isotropy. One of the many estimators of isotropy is the normalized information entropy S, defined as

$$S = -\sum \frac{\frac{N_i}{N} \ln\left(\frac{N_i}{N}\right)}{\frac{A_i}{4\pi} \ln\left(\frac{A_i}{4\pi}\right)}, \tag{2.72}$$

where N_i is the number of particles in sky bin i and A_i the fraction of the full solid angle of bin i (size of the corresponding patch). N is the total number of particles, in this case 50 000. The relation (2.72) is zero in the extreme anisotropy case where all the particles land in one bin.

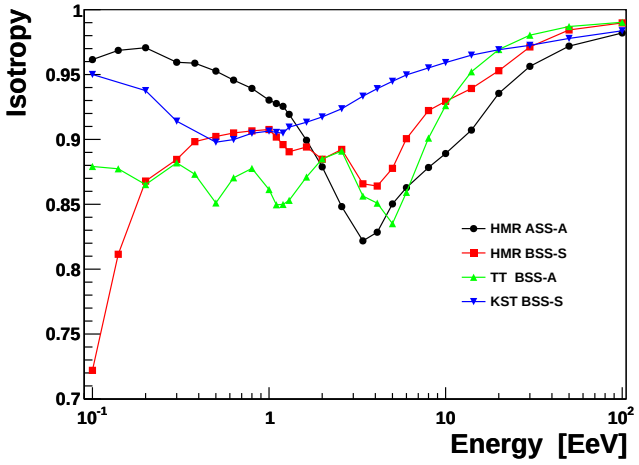

Figure 2.25: The entropy estimator of isotropy for different energies and models.

Conversely, it is one when the amount of particles in every bin is proportional to the bin size (isotropic distribution). In figure 2.25, the isotropy is lowest for the HMR BSS-S and TT BSS-A models for energies lower than 1 EeV. From 1 EeV and onwards all the models have more or less the same degree of isotropy that converges to 1 at higher energies. The exception is the KST model with its higher degree of isotropy in this energy range. Although the overall sky is isotropic for higher energies this is not true for the different sky regions. There are blind regions that have to be taken into account. For the HMR ASS-A and TT BSS-A models there are blind regions along the vicinity of the galactic equator for energies up to 100 EeV. For the KST model a large blind region around the galactic center remains even for the highest energies. As noted in section 2.5, for the KST BSS-S model the deflection of 100 EeV protons in region B is of order 6°, making any attempt for a source search with high accuracy impossible (under the working assumption that the models accurately describe the GMF).

Chapter 3

Magnetic Deflections at the Galactic Center

3.1 Introduction

Although the Galactic Center (GC) is not known for excesses of very high energy cosmic rays it has been a subject of anisotropy studies by several cosmic ray experiments, including PAO. In addition, the INTErnational Gamma-Ray Astrophysics Laboratory (INTEGRAL) measures positron-annihilation signal from the GC [87]. The GC is a source of positron-annihilation X-rays at 511 keV [88] (see figure 3.1).

The AGASA experiment reported a cosmic ray excess of 22% from a part of the GC region (see e.g. [89]), for energies around 1 EeV. By reexamining the data from the SUGAR experiment, Bellido *et al.* found another excess from a region around 10° around the GC [90, 91].

Although PAO rejected the claims of GC excesses found in data gathered by other experiments (see [92] and references therein), cosmic ray excess from the GC is recently found for an energy threshold of $E_{\text{th}} = 10^{17.8}$ eV and angular radius of $\gamma = 11^{\circ}$ by R. Bonino and G. Navarra [93], but at much smaller levels. They suggest a prescription for a cosmic ray excess search using the parameters E_{th} and γ.

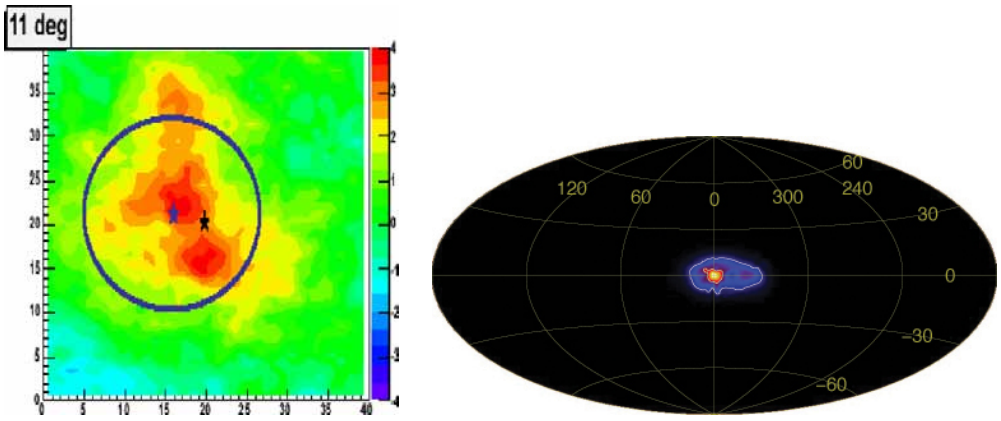

Figure 3.1: Left panel: The figure shows the GC excess for the parameters $E_{\text{th}} = 10^{17.8}$ eV and $\gamma = 11^{\circ}$. Black star is the GC while the blue star represents the point with maximum excess. Figure taken from Bonino and Navarra [93]. Right panel: The 511 keV X-ray signal due to positron annihilation, from the INTEGRAL measurement [94].

Due to the low energy threshold of the excesses reported it is often assumed that the cosmic

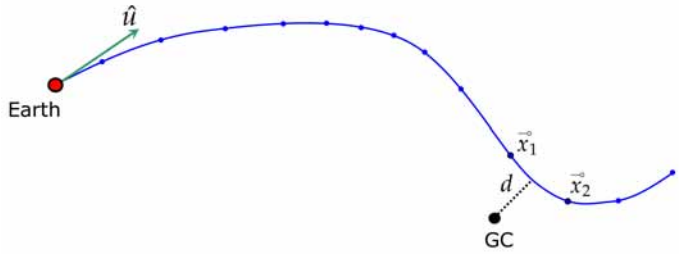

Figure 3.2: The impact parameter, d, between the GC and the path obtained by backtracking. $\hat{u}$ is the initial arrival direction as a function of l_0 and b_0 defined in the text.

rays originating from the GC are neutrons (see e.g. [89, 90, 91, 92] and the references therein). The production and decay of neutrons also involves production of protons [91, 95].

For an anisotropy search, establishing the size of the deflections of potential protons is crucial and many attempts are found in literature.

For example, G.A. Medina-Tanco and A.A. Watson [91] investigate the deflections of protons that are produced by propagating and decaying neutron primaries. Using different GMF models they are unable to reproduce at Earth the excesses reported by [89, 90] due to large deflections. They suggest the possibility of proton primaries being responsible for the observed excesses if the source is located closer than 1.6 kpc from Earth.

On the other hand, R.W. Clay [95] investigates the deflection of GC protons resulting from neutron production. Due to lack of a precise method some approximations are made by R.W. Clay. GC protons are said to be observed at Earth if they reach the radial distance of 8.5 kpc from the GC, and if their distance to the galactic plain is less than 1 kpc. Using a GMF model with both regular and random components deflections of order 10° are found for 10 EeV protons. R.W. Clay also concludes that a source in the GC is undetectable for protons with energies below 1 EeV.

The following chapters take these appraisals as a starting point. The goal is to assess the deflections of GC protons within the assumption that some of the GMF models are correct or at least quantitatively describing the GMF correctly.

A powerful procedure is constructed in section 3.2 that makes it possible to obtain the arrival directions at Earth of protons originating *exactly* from the GC. This makes it possible to calculate deflections precisely, unlike in [95] where the deflections are merely indicative.

The GC is located at the galactic disk and thus the symmetry of the magnetic field with respect to disk crossing is important in this study. In the following chapter the HMR ASS-A and BSS-S models are used. Since the TT BSS-A and KST BSS-S models have the same symmetries with respect to the disk as the HMR models, they are not used in the following considerations.

The results of this study are published in reference [96].

3.2 Shooting procedure

In order to establish the deflections of the cosmic rays originating from the GC region their incoming directions at Earth are needed. These are obtained by the shooting procedure described here.

Starting from the position of the Earth, given by $(-8.5, 0, 0)$ kpc, a single proton with fixed energy E is backtracked using the relativistic equations of motion (2.63). The *initial* direction $\hat{u}$ is given by the input parameters, galactic longitude l_0 and latitude b_0. Consequently, an *initial* path with a certain distance to the GC is acquired. What is required, however, is to find the proton trajectory with impact parameter d (see figure 3.2) equal to zero. For $d = 0$, the trajectory goes through the GC. Points $\vec{x_1}$ and $\vec{x_2}$ are the closest and the next closest points, respectively, to the path from the GC.

With a fixed energy the minimal impact parameter can only be obtained by varying the initial coordinates l_0 and b_0 until the subsequent backtracking yields a trajectory that is as close as possible to the GC. For this purpose `TMinuit` [97] is used. `TMinuit` is a multipurpose package in ROOT used for minimization of functions with respect to chosen parameters.

After the initial path is acquired, `TMinuit` varies the initial coordinates, l_0 and b_0. The new varied coordinates are used for backtracking and a new proton path that is closer to the GC is obtained.

The procedure continues until a minimal possible impact parameter d is obtained. As noted, the trajectories go through the GC only if $d = 0$.

The distance to the galactic center from the *interpolated* proton path is given by,

$$d^2 = \frac{1}{s^2}\left[|s|^2|p|^2 - (\vec{s}\cdot\vec{p})^2\right], \tag{3.1}$$

where $\vec{p}$ is the vector between the GC and $\vec{x_1}$ the closest point of the proton's path to the GC. $\vec{s}$ is the vector between $\vec{x_1}$ and the next closest point to the GC, $\vec{x_2}$.

The new directions yielding a zero for equation (3.1) are called shooting directions for an obvious reason. When shooting directions are backtracked they yield trajectories that go directly through the GC.

3.3 Shooting directions

Ten thousand proton events are generated with randomized energies between 0.1 to 150 EeV. The initial randomized directions $\hat{u}$, given by the input parameters l_0 and b_0, are chosen to be inside a window of $\pm$ 20° around the direction to GC and are then run through the `TMinuit` minimizer to find the final directions that produces trajectories going through the GC. Shooting directions obtained by the procedure described in section 3.2 are shown in figure 3.3.

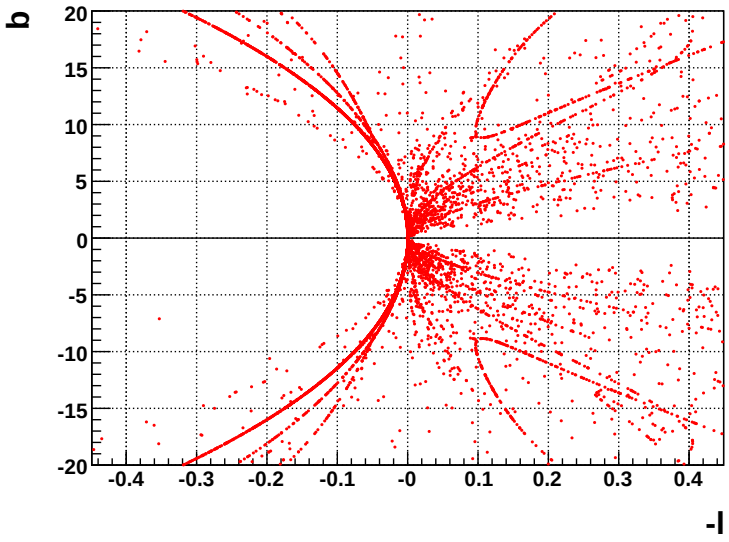

Figure 3.3: The shooting directions resulting in cosmic ray tracks going through the GC for the HMR ASS-A model for energies in the range 0.1 EeV to 150 EeV.

The HMR ASS-A model is used. As noted in section 3.2 these shootings directions, when backtracked, lead to propagation of particles through the GC. The shooting directions are thus the GC images as seen at Earth. In figure 3.3 there are shooting directions continuously moving with changing energy. In addition, figure 3.3 is filled with scattered shooting directions both

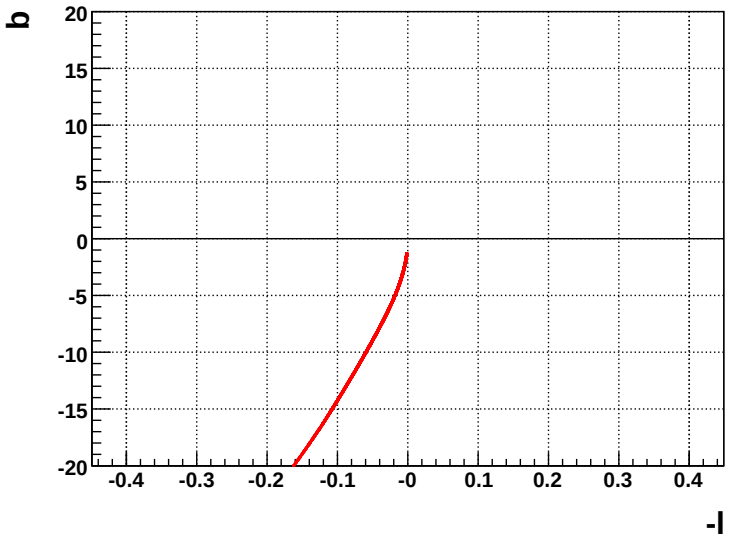

Figure 3.4: The shooting directions resulting in cosmic ray tracks going through the GC for the HMR BSS-S model for energies in the range 0.1 EeV to 150 EeV.

above and below the disk. For the HMR ASS-A model the shooting directions are symmetrical due to the field reversal with respect to the galactic disk.

For the HMR BSS-S model the shooting directions are only found below the galactic disk. This is due to the non-reversal of the field at disk crossing. The shooting directions for the HMR BSS-S model are shown in figure 3.4.

3.4 Deflections

Observing from Earth, the direction towards the GC is simply $\hat{u}_{\mathrm{GC}} = (1, 0, 0)$. The deflection α for particles arriving from the GC is thus given by,

$$\cos\alpha = \hat{u}_{\mathrm{sh}} \cdot \hat{u}_{\mathrm{GC}} = u_x, \tag{3.2}$$

where $\hat{u}_{\mathrm{sh}}$ is the shooting direction and u_x is its x-component. Since $\cos\alpha = (1 - \sin^2\alpha)^{1/2}$ and $u_x = (1 - u_y^2 - u_z^2)^{1/2}$ expression (3.2) is rewritten as,

$$\sin\alpha = \sqrt{u_y^2 + u_z^2}, \tag{3.3}$$

where u_y and u_z are given by the shooting directions. Figure 3.5 shows the deflections of protons from the GC in the energy range 0.1 EeV to 150 EeV.

From 5 EeV to 150 EeV the deflections change smoothly with changing energies. At 0.1 EeV to 1 EeV a chaotic regime prevails and the deflections are scattered with respect to changing energy. A transitional phase is seen between 1 EeV and 5 EeV. There also exists a set of deflections that are zero or close to zero covering the whole energy range. This trivial solution, like the chaotic deflection regime between 0.1 EeV and 1 EeV, is a result of the field reversal with respect to the z-axis. As shown in a figure 3.6 the field for the HMR ASS-A model goes to zero at $z = 0$. This makes it possible for protons with energies as low as 0.1EeV to propagate to Earth. In the next sections two energy ranges are investigated. The higher energy range from 10 EeV to 150 EeV, and the lower energy range from 0.1 EeV to 1 EeV.

For the HMR BSS-S model the deflections change smoothly with changing energy as seen in figure 3.7. The deflections are in the range 2 EeV to 150 EeV.

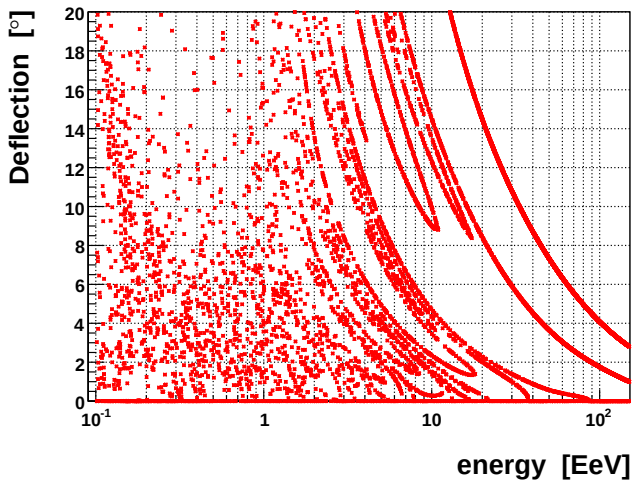

Figure 3.5: The energies and their corresponding deflections in the HMR ASS-A model for energies in the range 0.1 EeV to 150 EeV. Note the solution with no deflection.

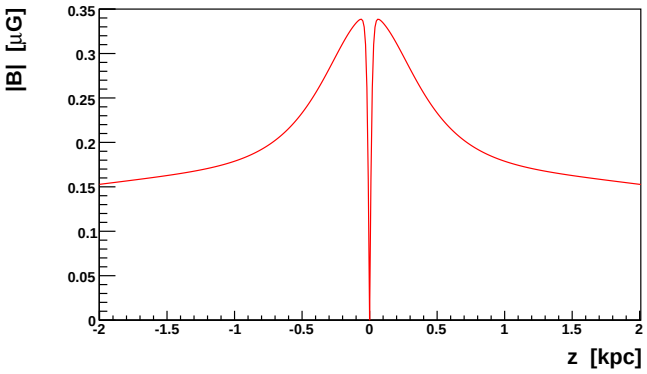

Figure 3.6: The magnitude of the magnetic field produced by the HMR ASS-A model at the position of the Earth as a function of the z-coordinate. Note the zero-field at $z = 0$. This ensures that cosmic rays with even the lowest energies originating from the GC are not deflected. The zero-field creates a "channel" that lies on the galactic disk between Earth and the GC where non-deflected particles propagate.

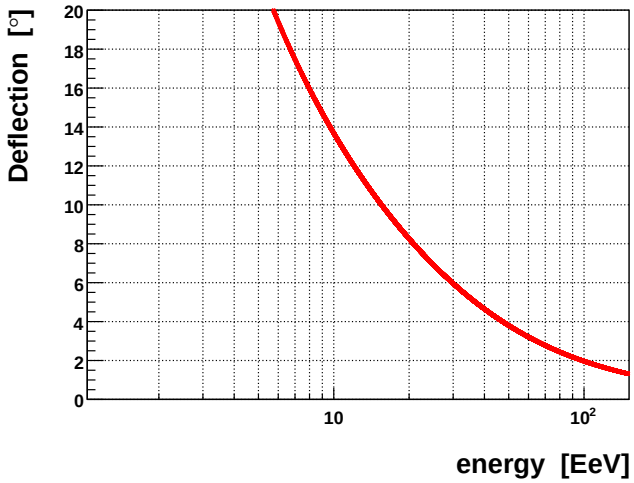

Figure 3.7: The energies and their corresponding deflections in the HMR BSS-S model for energies in the range 0.1 EeV to 150 EeV.

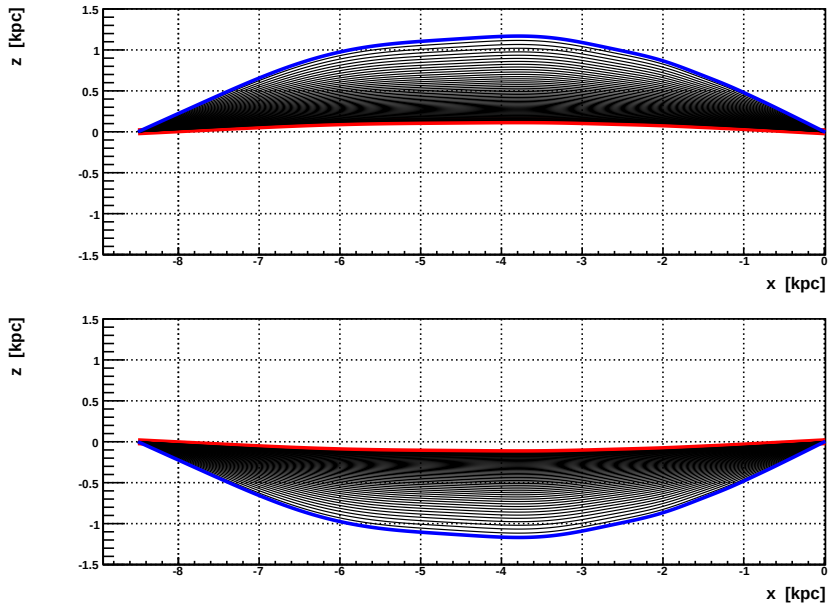

Figure 3.8: Upper and lower plots show trajectories in the xz plane for shooting directions with $0^\circ < b < 90^\circ$ and $-90^\circ < b < 0^\circ$, respectively. The energies are continuous between 10 (blue) and 150 EeV (red). HMR ASS-A model is used for GMF.

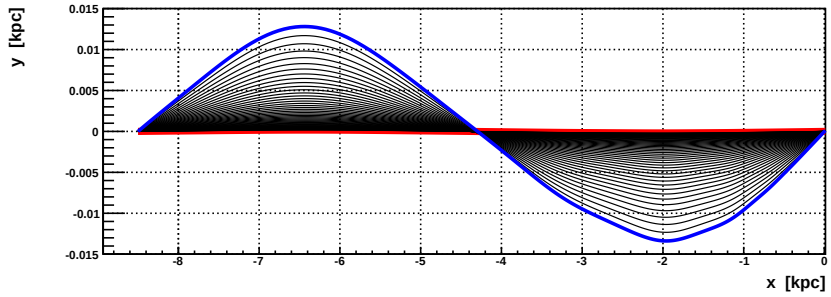

Figure 3.9: The xy plane trajectories for continuous energies between 10 (blue) and 150 EeV (red). HMR ASS-A model is used for GMF.

3.4.1 High energies

HMR ASS-A model

Figure 3.8 shows the tracks of proton trajectories in the xz plane ending at Earth at $x = -8.5\,\mathrm{kpc}$ and starting at the GC. The upper plot shows the trajectories for shooting directions with latitudes in the range $0^\circ < b < 90^\circ$, i.e. for positive $\hat{u}_z$ values. The lower plot shows trajectories when the $\hat{u}_z$ values are negative. Note that the trajectories are above and below the galactic disk for positive $\hat{u}_z$ and negative $\hat{u}_z$, respectively.

Figures 3.9 and 3.10 display the trajectories in the xy and yz plane, respectively.

The most striking feature in the two latter plots is the extent of the trajectories into the y-direction. The trajectories reach a maximum of only $y = \pm 0.014\,\mathrm{kpc}$. Clearly the deflections are negligible in y direction i.e. $\hat{u}_y \approx 0$. Effectively, the trajectories are restricted predominately into x and z-directions. In the following, this fact is used to derive a simplified picture of the force acting on a cosmic ray.

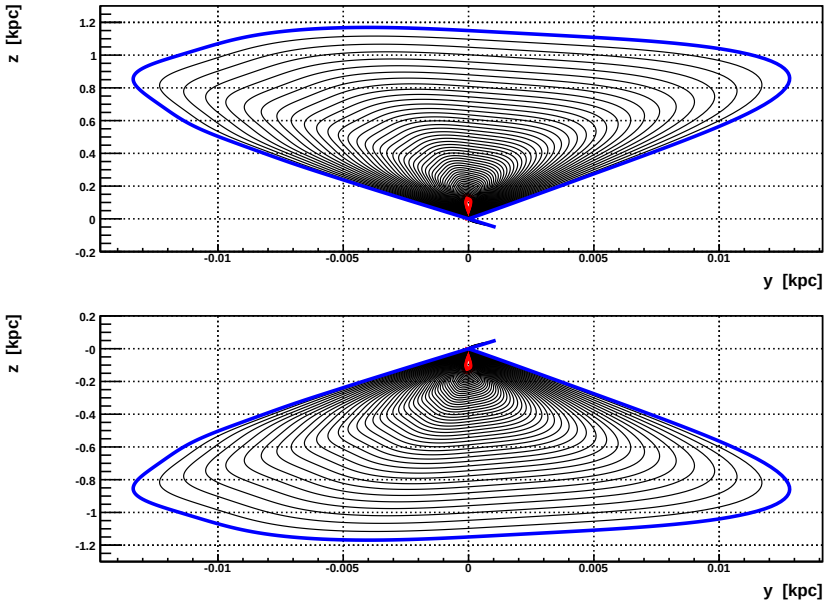

Figure 3.10: Upper and lower plots show trajectories for shooting direction with $0^\circ < b < 90^\circ$ and $-90^\circ < b < 0^\circ$, respectively, in the yz plane. The energies are continuous between 10 (blue) and 150 (red) EeV. HMR BSS-S used as GMF model. Note that the z and y axes are not given in the same scale.

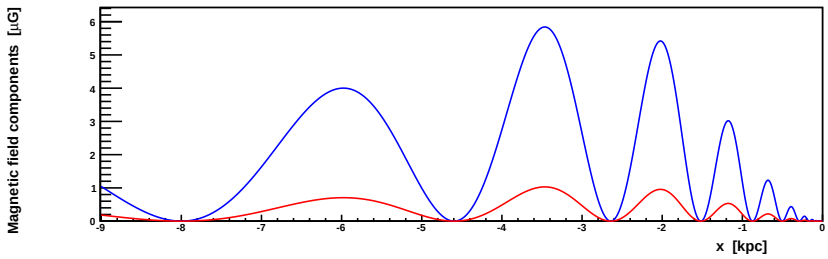

Figure 3.11: The magnitudes of the B_x and B_y components of the disk field from the HMR-ASS-A model in blue and red, respectively. The magnitudes are calculated 0.1 kpc above the disk and along the direction towards the GC.

The Cartesian components of the galactic magnetic field are expressed as,

$$\begin{aligned} B_x &= (x \sin p - y \cos p) B_{\text{halo}}, \\ B_y &= (y \sin p + x \cos p) B_{\text{halo}}, \end{aligned} \tag{3.4}$$

where the pitch angle is $p = -170^\circ$ and the field component B_{halo} is defined in chapter 2. Since $\sin p$ is negligible and the starting position of the backtracked particles is $\vec{x}_{\text{Earth}} = (-8.5, 0, 0)$ kpc equations (3.4) yield,

$$\begin{aligned} B_x &\approx 0, \\ B_y &\approx (x \cos p) B_{\text{halo}}. \end{aligned} \tag{3.5}$$

Figure 3.11 gives an idea of the discrepancy regarding the magnitudes of the components. The figure shows the B_x and B_y components 0.1 kpc above the disk and along the direction towards the GC.

Since the HMR models lack a B_z component and $\hat{u}_y \approx 0$, the Lorentz force becomes,

$$F_{\text{Lorentz}} \approx \hat{u}_x \, B_y \, \hat{z}. \tag{3.6}$$

The Lorentz force in (3.6) acts only in the z-direction. On the way to Earth the cosmic rays oscillate up and down around $z = 0$, as evident from figure 3.8. The Lorentz force is thus acting like a restoring force in a harmonic oscillator.

Low energies

The Lorentz force acting like a restoring force has repercussions for the low energy particles. As seen from figure 3.8 and equation (3.6), the particles are pulled back into the galactic disk. Taking into account the "channel" in figure 3.6 this yields "a particle in a box"-behavior for the low energy protons as seen in figure 3.12. For this figure the initial randomized directions are generated inside a window of $\pm 10^\circ$ around the galactic center. Energies are generated in the range of 0.1 EeV to 1 EeV.

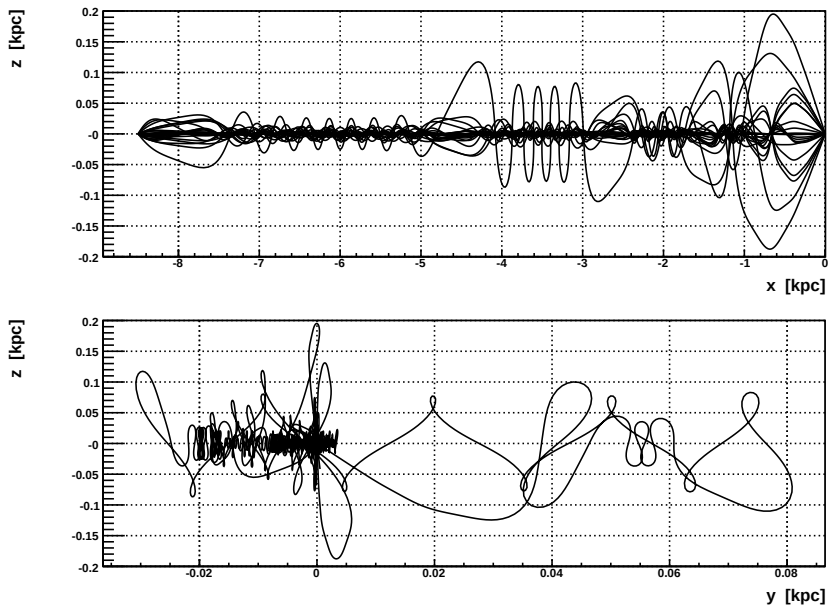

Figure 3.12: "Particle in a box" behavior of several generated cosmic ray protons in the "channel". Energies range from 0.1 EeV to 1 EeV. Initial directions are generated in the range $\pm 10^\circ$ around the GC.

The Lorentz force, drawing particles back towards the galaxy disk, acts as a potential wall, trapping the particles inside the region $-0.2\,\text{kpc} < z < 0.2\,\text{kpc}$ around the disk. Above 1 EeV, particles start to escape this region and enter the transitional regime in figure 3.5. For increasing energies the deflections begin to change continuously, yielding the trajectories in the figures 3.8 to 3.10. Note that the trivial solution with no deflection is always present due to zero-field caused by the field reversal with respect to z-direction.

The channel solution also implies that sources located in the GC are detectable at Earth, no matter how low the energy of the GC particles.

3.4.2 Deflections - HMR BSS-S

High energies

In contrast to the HMR ASS-A model the BSS-S version produces proton deflections only in the range 2 EeV to 150 EeV due to the non-changing field along the z-direction. Hence, the model is not interesting for lower energies. However, unlike the HMR ASS-A model the BSS-S model has field reversals between the spiral arms.

Figure 3.13 shows that the trajectories are both above and below the galactic disk in the xz plane. Compared to figure 3.8 it is clear that the particles are deflected less than in the HMR ASS-A model. Figures 3.14 to 3.15 show the trajectories in the xy and yz planes, respectively. Figure 3.16 shows the differences between the B_x and B_y components of the model 0.1 kpc above the disk and along the direction towards the GC. The magnitudes alternate between positive and negative values. This is due to the field reversals between the spiral arms.

The deflections in the two HMR models are compared in figure 3.17. The deflection of 10 EeV protons in the HMR BSS-S model is comparable to the deflections found in [95]. In the case of the HMR ASS-A model, however, the deflections are around 10° larger.

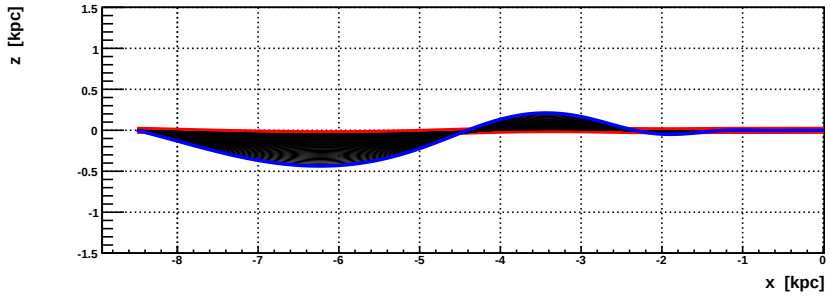

Figure 3.13: The xz plane trajectories for continuous energies between 10 (blue) and 150 EeV (red). HMR BSS-S is used as GMF model.

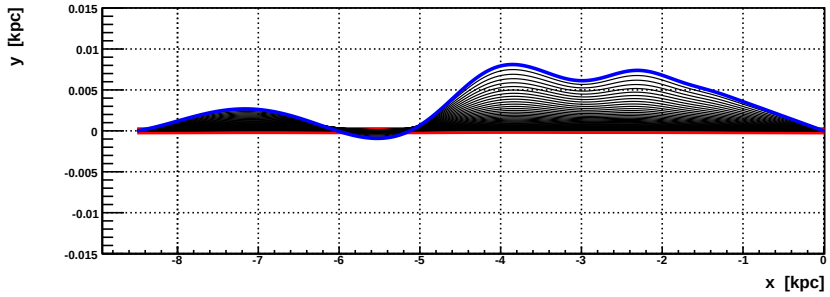

Figure 3.14: The xy plane trajectories for continuous energies between 10 (blue) and 150 EeV (red). HMR BSS-S used as GMF model.

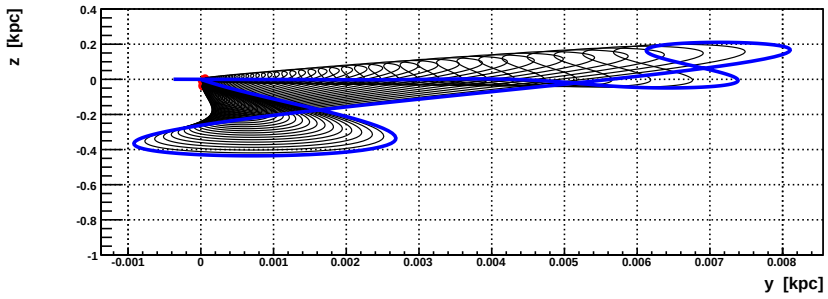

Figure 3.15: The yz plane trajectories for continuous energies between 10 (blue) and 150 EeV (red). HMR BSS-S is used as GMF model.

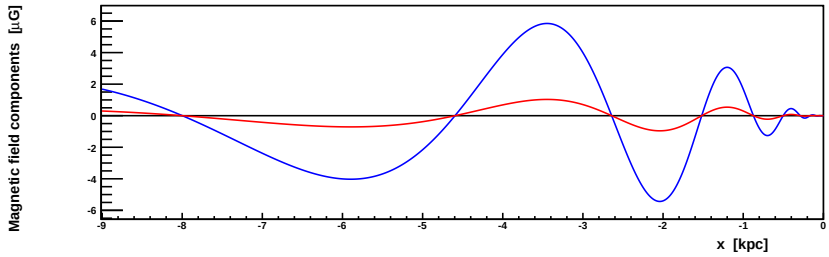

Figure 3.16: The magnitudes of the B_x and B_y components of the HMR BSS-S model in blue and red, respectively. The magnitudes are calculated 0.1 kpc above the disk and along the direction towards the GC. The field alternates between positive and negative values since the BSS configuration ensures sign reversals between the spiral arms.

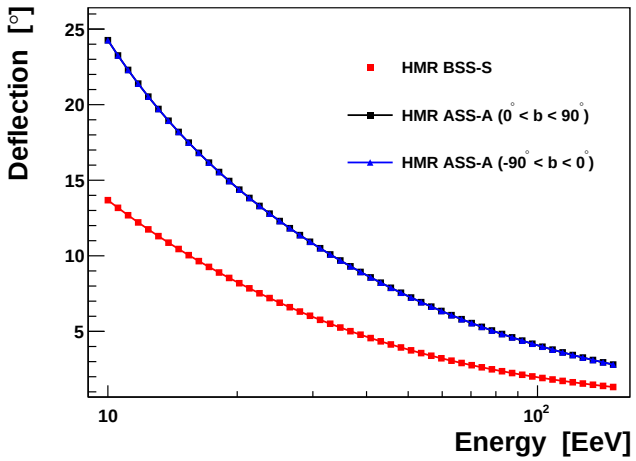

Figure 3.17: The difference in deflections in the HMR ASS-A and BSS-S models as a function of energy. For the HMR ASS-A model the deflections for positive and negative values of $\hat{u}_z$ are shown. The deflections are related to the tracks in the figures showing the xz, xy and yz planes. Note that the deflections in the HMR ASS-A model are overlapping for positive and negative values of $\hat{u}_z$.

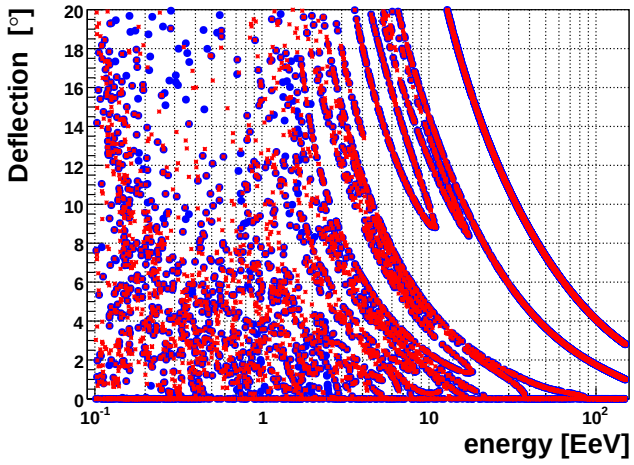

Figure 3.18: Deflections calculated by the equations (3.3) (red dots) and (3.7) (blue dots).

3.5 Simplified equations of motion

As shown in the previous section, the deflections in the y direction are negligible. By assuming $\hat{u}_y \approx 0$ the deflection α for particles originating from the GC in equation (3.3) is now given by,

$$\sin\alpha = u_z, \tag{3.7}$$

where $\arcsin(u_z)$ is just the galactic latitude b obtained from the shooting procedure. The deflections as given by equations (3.3) and (3.7) are compared in figure 3.18. In the transitional range between 1 EeV and 5 EeV discrepancies appear, especially between 1 EeV and 2 EeV. In the chaotic range these discrepancies are clearly visible. However, there is a full agreement for energies in the range from 5 EeV to 150 EeV. The global structure of the deflections for high energies is thus well described by equation (3.7). The assumption $\hat{u}_y \approx 0$ is thus perfectly valid for high energies. The deflections for high energies are thus *equivalent* to the galactic latitudes b as seen in equation (3.7).

From section 3.4.1 it is clear that $y \approx 0$ and $B_x \approx 0$. These facts are used in the following to derive an effective propagation model.

By assuming $y \approx 0$, $u_y \approx 0$ and $B_x \approx 0$ and $u_x \approx 1$ (since $u_x = \cos l \cdot \cos b$ where l is galactic longitude and b is galactic latitude) the equations of motion are rewritten in the following form,

$$\begin{aligned}
\frac{\mathrm{d}x'}{c\mathrm{d}(t)} &= u_x, \\
\frac{\mathrm{d}z}{c\mathrm{d}(t)} &\approx u_z, \\
\frac{\mathrm{d}u_z}{c\mathrm{d}(t)} &\approx -\frac{qc}{E} B_y(x', z).
\end{aligned} \tag{3.8}$$

The first equation is integrated analytically. At $t = 0$ the position of the particles is at Earth. Integrating yields

$$x' = ct - 8.5\,\mathrm{kpc}. \tag{3.9}$$

From equations (3.8) it is clear that there are no deflections when $z = 0$ since $B_y(x', 0)$ is zero. Hence only the first equation remains, showing that the cosmic rays travel linearly from the GC to Earth when $z = 0$. Figure 3.19 compares the galactic latitudes obtained by the shooting procedure when ordinary and simplified equations of motions are used. As noted the deflections are equivalent to the galactic longitudes for high energies. From 5 EeV and higher, there is no

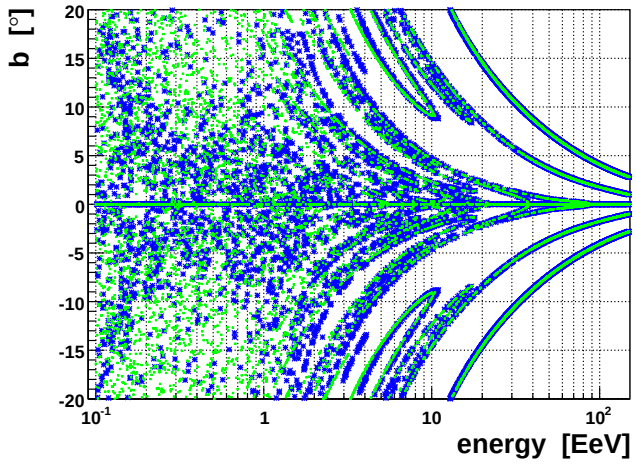

Figure 3.19: Shooting latitudes versus energy. The latitudes obtained by the ordinary equations of motion and the simplified equations in blue and green, respectively.

difference between the two sets of latitudes. Hence the effective propagation model is valid for high energies. As expected, this agreement deteriorates as the energy decreases.

3.6 Conclusion

As noted in the introduction, a prescription for GC excess search is under development by the PAO. The scan parameters suggested in [93] include an energy threshold of $10^{17.8}$ eV and an angular radius of 11°. Section 3.4.1 established that the B_y component of the magnetic field is dominating, ensuring propagation mainly in the xz direction. If propagation in only x direction is assumed, the Lorentz force yields,

$$B_y = -\frac{E \sin\left(\frac{\alpha}{2}\right)}{qcL/2}, \tag{3.10}$$

where α is the observed deflection and L is the distance to the GC, 8.5 kpc. Substituting the constants and the variables for their magnitudes and units, yields,

$$\left(\frac{B_y}{\text{nG}}\right) \approx -252 \sin\left(\frac{\alpha}{2}\right) \left(\frac{E}{\text{EeV}}\right), \tag{3.11}$$

where E is the energy of the particles. Using the parameters maximizing the GC excess found in reference [93] sets a boundary on B_y of 15 nG. Assuming that $B_x \approx 0$ (see equation (3.5)) and that the GC is really the source of this excess, the average *magnetic field* thus is only 15 nG, putting a constraint on the models.

This estimated value is low compared to the B_y components of the HMR models in figures 3.11 and 3.16. Fortunately, as seen in figure 3.11 there exists in the HMR ASS-A model a channel where the field is zero or extremely low, yielding a trivial solution with no deflection. The low estimation of B_y in equation (3.11) is thus compatible with the HMR ASS-A model. The trivial solution also implies that a source in the GC is indeed observable at Earth, no matter how low energy the GC cosmic rays have.

The BSS-S configuration yields smaller deflections for higher energies than the ASS-A, as seen in figures 3.13 - 3.17. But this is irrelevant for the search of a cosmic ray excess from the GC as 10 EeV particles are deflected around 15° in this model! For the HMR ASS-A model the

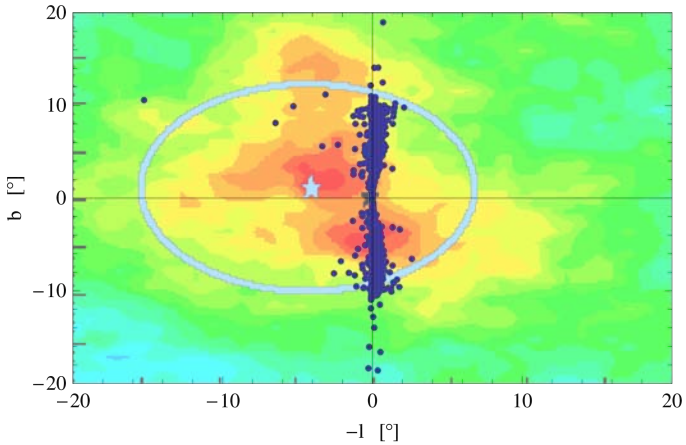

Figure 3.20: Shooting directions for energies lower than 10 EeV (blue) are superimposed on an event excess map from GAP-2008-008 [93].

deflections for 10 EeV particles range from 25° down to almost zero due to the existence of the trivial solution.

The field reversal with respect to the disk in the HMR ASS-A model also looks appropriate when the excess map of the GC from [93] is scrutinized. Clearly the excesses above and below the disk plane in figure 3.20 might be explained by a field reversal in the z direction. Shooting directions in the energy range from 10 EeV and lower, obtained for the HMR ASS-A model are superimposed on the excess map. Although the shooting directions are not smeared out as much as the excess, they are compatible with the two excess clouds above and below the galactic disk. Each of the clouds are smeared out around 10°. For $E = 10^{17.8}$ eV and $\alpha = 10°$ equation (3.11) yields a magnitude of 14 nG.

If the parameters in the proposed prescription are kept, models with non-changing field with respect to the z direction *and* a field strength as strong as implied by the HMR BSS-S model are excluded. Conversely, a $10^{17.8}$ eV threshold makes sense within models like the HMR ASS-A.

If it turns out that our galaxy indeed has a BSS-S configuration and a magnitude as large as predicted in the HMR BSS-S model the excess observed from the GC can only be explained by emissions of neutral primaries, like neutrons. The neutron primary assumption has been suggested before by many papers.

Any verified excess from the GC will have a huge impact on not only the constraining of the models of the GMF but also on the composition of the cosmic rays from the GC.

Chapter 4

Magnetic Deflections and Active Galactic Nuclei

4.1 Introduction

In 2007 PAO reported an observed correlation of UHECR events and Active Galactic Nuclei (AGN) in Science [98]. A long and more detailed paper was published in 2008 [99]. A description of the search method is found in appendix B.2. After an exploratory scan on data from the period January 2004 to May 2006 anisotropy was confirmed [98, 99, 100]. The anisotropy was reconfirmed using data from May 2006 to August 2004 [98, 99]. The scan was repeated on the full data set from January 2004 till the end of August 2007. The scan parameters yielding *maximum anisotropy* were $E_{\text{th}} = 57\,\text{EeV}$, $z_{\text{max}} = 0.017$ and $\Psi = 3.2^\circ$ [98, 99], where E_{th} is the minimum energy and z_{max} the maximum redshift. Ψ is the correlation maximizing angular separation between the Auger events and the AGNs. A total of 5.6 events were expected to correlate by chance. Instead, 20 out of a total 27 events above 57 EeV correlated with 20 AGNs with a minimum binomial scan probability of 4.6×10^{-9} (non-penalized). Some of the Auger events correlated to two or more AGNs making the total number of correlations 25 (see table 4.1). The real chance probability after penalizing for scanning was calculated to be $P = 10^{-5}$. The difference between the two probabilities is explained in appendix B. Significant anisotropy is also observed for angular separations up to 6°. This range was denoted as the "angular scale of correlation" [99]. Following the Auger Collaboration's report a huge debate ensued challenging those claims.

The effect of the galactic magnetic field was briefly mentioned in reference [99]. Using the HMR BSS-S model under the assumption that the cosmic rays are protons, Auger events were backtracked until their distance to the galactic center reached 20 kpc. It was concluded that the deflections were compatible with the angular range of correlation provided that the HMR BSS-S model is more or less reliable and that the correlating cosmic rays are protons. The deflections are shown in figure 4.1. However, this conclusion was based on using only the HMR BSS-S model. In addition, the backtracked Auger events were not used for calculating the new "corrected" correlation.

The goal of this chapter is to check if the correlation between the UHECR – AGN is reasonable after taking into account the magnetic deflections. This is done in three analyses. In all of them it is assumed that the cosmic rays are protons.

The first analysis in section 4.3 investigates the deflections of generated protons that originate *exactly* from the AGNs in table 4.1. In order to get the arrival directions of protons originating exactly from the AGNs a shooting procedure is constructed (section 4.2). These arrival directions (shooting directions) are then used to calculate the deflections caused by different GMF models. The deflections are compared with the angular distance $\Psi = 3.2^\circ$.

In the second analysis (section 4.4) the arrival directions of generated protons originating exactly from the AGNs are compared to the Auger data directions. In addition, the backtracked

Auger Event	Energy [EeV]	l [°]	b [°]	AGN	l_{AGN} [°]	b_{AGN} [°]
200719304931	90.3	12.2	−49.0	4627	10.1	−50.7
200719304931	90.3	12.2	−49.0	4624	9.9	−50.4
200603501150	85.2	−165.9	−46.9	1030	−169.6	−46.5
200603501150	85.2	−165.9	−46.9	1045	−169.4	−45.6
200414200633	84.5	−50.8	27.6	3285	−47.2	28.1
200505400622	83.6	−75.6	−78.6	556	−76.8	−78.3
200433900105	83.4	−27.9	−17.0	4427	−27.7	−14.7
200618504666	82.9	88.8	−47.1	4837	85.8	−49.4
200714500527	77.8	−163.8	−54.4	968	−165.8	−55.5
200506300054	71.1	58.8	−42.4	4673	63.0	−41.8
200722101059	70.9	−21.8	54.1	3516	−20.9	53.8
200706903088	69.8	−51.4	19.2	215	−50.5	19.4
200629900147	69.0	−51.2	17.2	215	−50.5	19.4
200629900147	69.0	−51.2	17.2	3312	−48.5	16.2
200629604873	68.5	−170.6	−45.8	1015	−173.6	−46.2
200629604873	68.5	−170.6	−45.8	1030	−169.7	−46.5
200629604873	68.5	−170.6	−45.8	1045	−169.4	−45.6
200428200333	66.1	−49.6	1.7	3370	−50.2	1.5
200708401685	64.0	−109.4	23.8	1900	−107.0	26.0
200434300218	63.3	−34.4	13.0	114	−33.9	14.0
200530601050	58.7	48.8	−28.7	4547	50.5	−26.0
200605500287	58.6	−27.6	−16.5	4427	−27.7	−14.7
200705100383	57.7	63.5	−40.3	4673	63.0	−41.8
200508101056	57.6	−52.8	14.1	3090	−54.7	13.3
200529501100	57.4	4.2	−54.9	4671	8.0	−54.8

Table 4.1: Auger data [98, 99] and their correlating AGN(s) from the Véron-Cetty-Véron catalog [101].

positions of the correlating Auger data are compared to the positions of their correlating AGNs. Two tentative "criteria" are made:

- The directions of the correlating Auger events should match the arrival directions (shooting directions) of generated protons originating *exactly* from the original AGNs in table 4.1. Here this criterion is fulfilled if the angular separation between the correlating Auger events and the generated protons originating exactly from the original AGNs is 1° or less. This number corresponds to the angular resolution of PAO.

- The positions of the backtracked correlating Auger events should lie inside a circle of radius 3.2° around their correlating AGN.

The criteria taken together imply that the measured correlating data have indeed its origin at the original AGNs, if the GMF models are correct. The first criterion checks if the path traveled by the Auger event points directly to its correlating AGN or not. The second criterion checks if the backtracked Auger event is inside the correlation circle defined by [98, 99]. Generally, the positions of backtracked events outside the galaxy, obtained by the *constant* velocity directions outside the galaxy, are viewed upon as pointing towards the source position, provided that the extra-galactic field is negligible.

Thirdly, in section 4.5, the correlation is recalculated after taking into account the galactic magnetic field. The code and procedure for the calculation of the correlation is the same as used in [98, 99, 100] and is found in reference [102]. The positions and red-shift distances of AGNs used in [98, 99] are found in the Véron catalog [101].

The results from the three analyses are discussed in section 4.6.

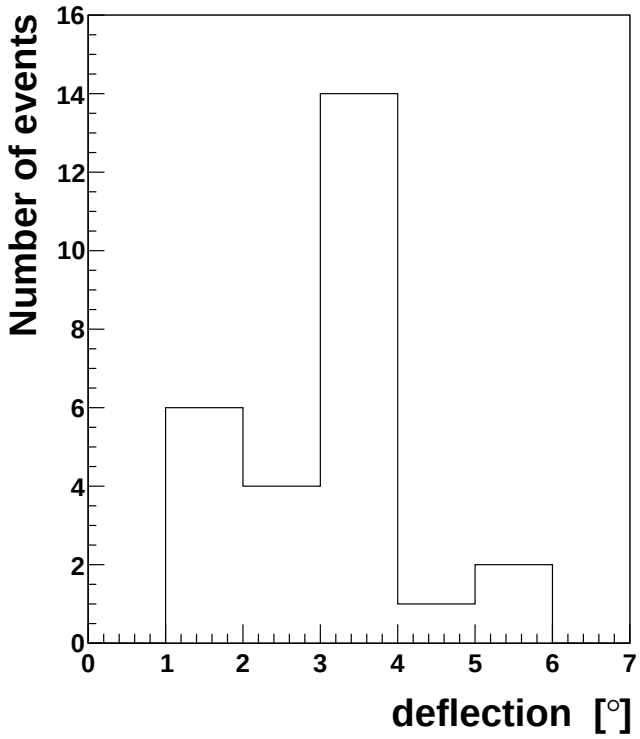

Figure 4.1: The deflections of Auger events under the proton assumption. The energy is above 57 EeV and the HMR BSS-S model is used. Note that this figure, produced here, is identical to the right plot in figure 8 in reference [99].

4.2 Shooting

Starting at Earth, protons with fixed energies and *initial* directions expressed in galactic longitude l_0 and latitude b_0 are backtracked until they are outside the galaxy. The directions of the backtracked protons just outside the galaxy are denoted as $\hat{u}_{\text{last}}$.

Unlike in the case of the galactic center there is no way to define a distance between the trajectories of the backtracked particles and their corresponding AGNs, that might be subsequently minimized.

However, knowing the direction of the AGNs, $\hat{u}_{\text{AGN}}$, and the directions of the backtracked particles outside the galaxy, $\hat{u}_{\text{last}}$, the following scalar magnitude is defined and minimized with `TMinuit`,

$$\Delta u = |\hat{u}_{\text{last}} - \hat{u}_{\text{AGN}}|. \tag{4.1}$$

When protons are backtracked out of the galaxy with the initial galactic coordinates l_0 and b_0, an Δu is acquired. `TMinuit` varies the initial coordinates until a minimum Δu_{min} is found. For $\Delta u = 0$ the direction of the backtracked protons outside the galaxy points directly to the AGNs. The new initial coordinates after minimization are the coordinates of incoming protons originating from the AGNs. Due to the finite numerical accuracy, however, a limit on the minimum is set to $\Delta u_{\text{min}} < \varepsilon$ where $\varepsilon = 0.5^\circ$ is the accuracy. In the following, the directions (given by galactic coordinates) of incoming protons originating from the AGNs are called shooting directions. The shooting directions are thus the AGN images at Earth as conveyed by the protons. The shooting procedure is demonstrated in figure 4.2.

Protons with 500 randomly chosen (l_0, b_0) and fixed energies in the range 0.1 to 150 EeV are generated and backtracked in the HMR ASS-A configuration.

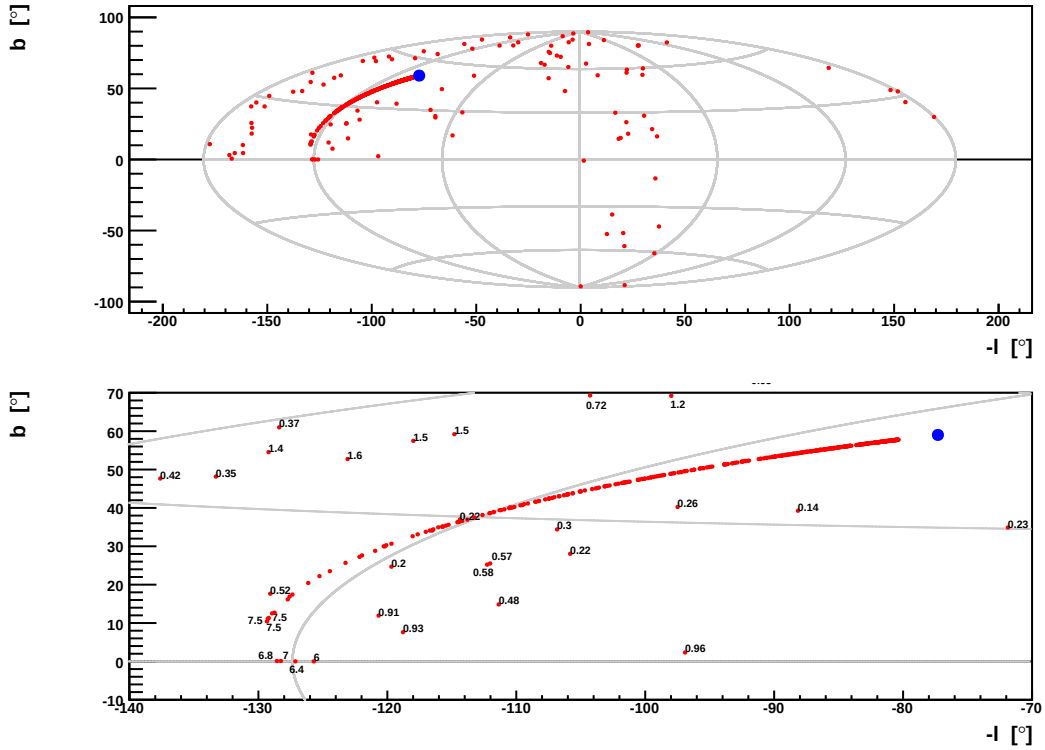

Figure 4.2: Upper plot shows the shooting directions (red) obtained for protons with energies from 0.1 EeV to 150 EeV in the HMR ASS-A configuration. The AGN (blue) was chosen arbitrarily from the Véron-Cetty-Véron catalog [101]. It has ID number 108 and its position in equatorial coordinates is RA $= 217.9279°$, DEC $= 63.0367°$. With its redshift quoted as zero this AGN lies closer than 4.2 Mpc from our galaxy and thus lies inside the local group of galaxies. Lower plot shows the thread-like shooting directions for protons in the range 7.5 EeV to 148 EeV. Note the three shooting directions of the 7.5 EeV protons at the end of the string. The transitional directions are seen on the galactic disk below the end of the thread-like string. The energies above 7.5 EeV are not labeled (i.e. the shooting directions in the thread-like string).

The $\hat{u}_{\mathrm{AGN}}$ is given by the position of an AGN from the Véron-Cetty-Véron catalog with the ID number 108 (chosen arbitrarily for this illustration). In the upper plot in figure 4.2 the shooting directions obtained by the procedure are shown. The blue dot represents the position of AGN 108. A thread-like string of shooting directions is seen. These move closer to the AGN position with increasing energies in the range 7.5 EeV to 148 EeV. An enlarged view of this string is seen in the lower plot. Labels for energies above 7.5 EeV are not shown. Three shooting directions for 7.5 EeV protons are seen at the end of the thread-like string. This pileup of shooting directions of 7.5 EeV protons indicates a cutoff. The energy range of the thread-like string (7.5 EeV to 148 EeV) corresponds approximately to the "ballistic limit" defined in chapter 2 where the deflection is a function of $\sim 1/E$. Just below the pileup and on the galactic disk, four shooting directions for protons in the energy range 6 EeV to 7 EeV are seen. These are not part of the thread-like string. Due to their proximity to the string these shooting directions might be regarded as transitional directions between the thread-like string and the more chaotic random shooting directions. Below 6 EeV the shooting directions become completely random. These random shooting directions are also not a part of the thread-like string and are seen in both plots.

Figure 4.3 shows 50 trajectories in the xz plane obtained by backtracking protons with the shooting directions from figure 4.2. Earth is located at $(-8.5, 0)$ kpc. The bundle with large number of trajectories to the left, below $x < -8.5$ kpc, is a result of backtracking part of the

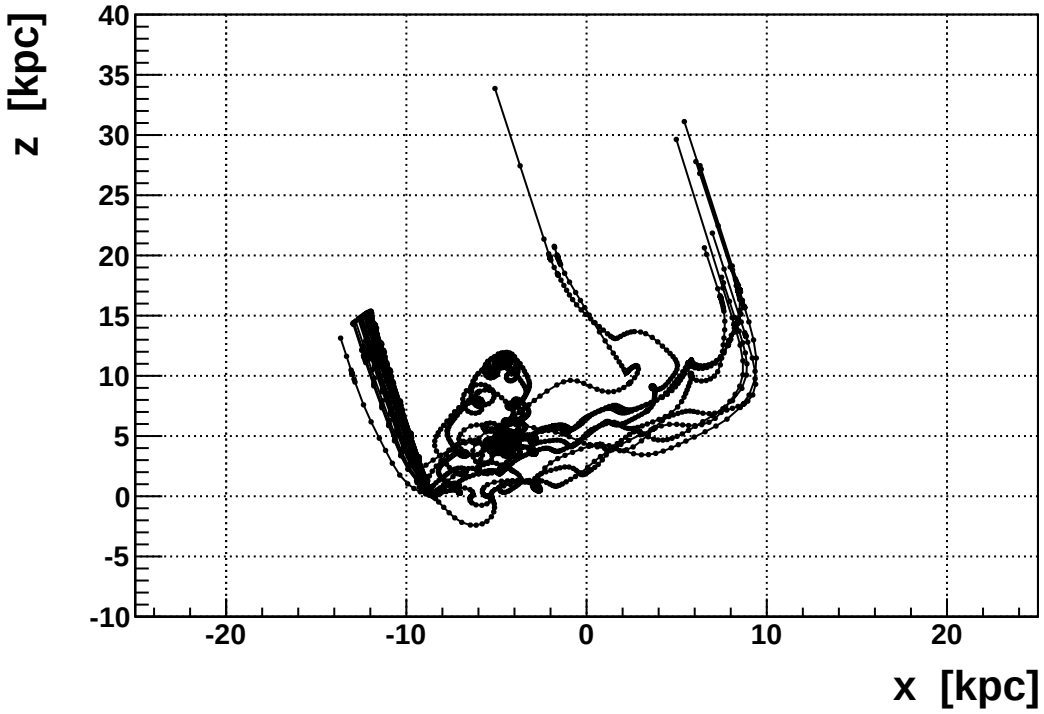

Figure 4.3: The trajectories in the xz plane aiming at the AGN. The trajectories are obtained by backtracking 50 shooting directions in figure 4.2 until the galaxy boundary (set at distance of 20 kpc). The thick bundle of trajectories to the left (below $x < -8.5$ kpc) is a result of backtracking part of the thread-like string of shooting directions. The single trajectory to the left of the bundle is due to one of the transitional shooting directions. The trajectories to the right, above $x > -8.5$ kpc, are due to the random shooting directions. Note that x and z axes are not given in the same scale.

thread-like string of shooting directions in figure 4.2. The trajectories start at Earth ($x = -8.5$ kpc) and leave the galaxy almost linearly, pointing to the AGN. The single trajectory to the left of the bundle is due to the backtracking of one of the transitional shooting directions in figure 4.2. The trajectory seems to have broken off from the bundle, implying its transitional character. The remaining trajectories above $x > -8.5$ kpc are due to the random shooting directions. These trajectories start at Earth position and traverse a large part of the disk before escaping the galaxy in the direction of the AGN. All the trajectories satisfy $\Delta u_{\min} = \epsilon$.

Assuming that the HMR ASS-A model gives a reasonable magnetic field strength, it is clear from this example how thread-like structures are produced. For protons with extremely high energies the shooting directions are inseparable from the AGN position. When the energies are lowered the AGN image is shifted on the sky as the thread-like structure in figure 4.2 shows. For protons in the energy range 6 EeV and lower, the AGN "image" is spread all over the sky. Shooting directions are from now on referred to as "AGN images". The issue of multiple images of cosmic ray sources is thoroughly discussed in reference [78].

Thread-like structures are further discussed and analysed in chapter 5. A similar shooting procedure is constructed by G. Golup *et al.* , see reference [103] for details.

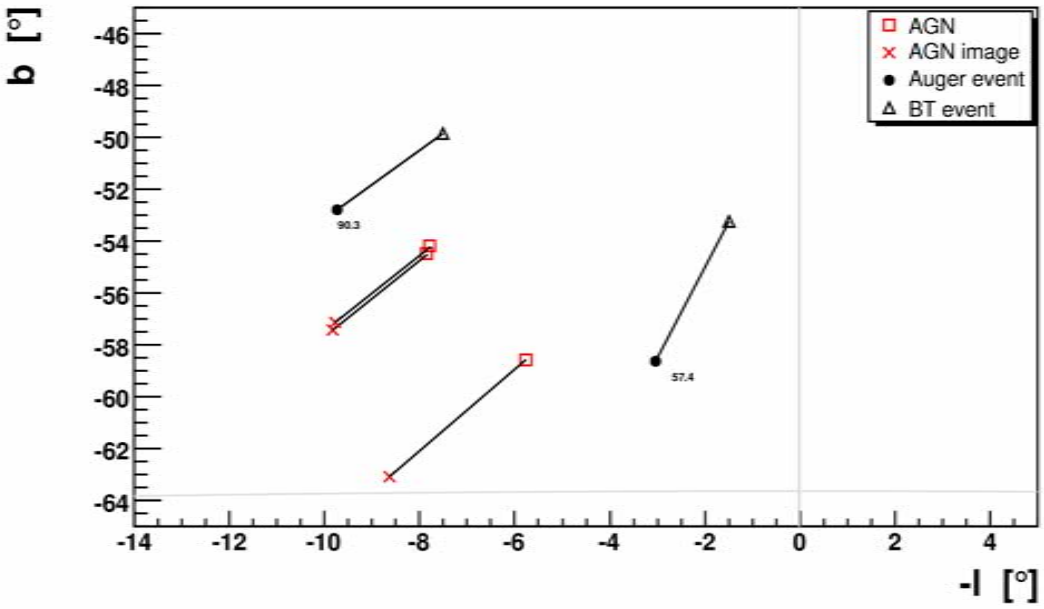

Figure 4.4: The 90.3 EeV and 57.4 EeV Auger events (black dots) and their correlating AGN(s) (red squares). The backtracked positions of the Auger events (triangles) are also seen. The AGN images (red crosses) are obtained by the shooting procedure and represent the arrival directions of protons that originate exactly from the AGNs. Here the HMR ASS-A model is used.

4.3 Magnetic deflections and Ψ

As mentioned in the introduction it was found that the observed angular range of correlation (1° to 6°) is compatible with the deflections of the Auger events in the HMR BSS-S model [99] if the Auger events are assumed to be protons. The deflections in reference [99] were calculated as,

$$\cos\alpha_{\text{data}} = \hat{u}_{\text{data}} \cdot \hat{u}_{\text{last}} \tag{4.2}$$

where $\hat{u}_{\text{data}}$ is the direction of the Auger events and $\hat{u}_{\text{last}}$ is the direction of the backtracked proton outside the galactic magnetic field.

In this section the size Ψ of the circles yielding maximum correlation, found by the PAO [98, 99], is compared to the deflections of generated protons that originate from the original AGNs.

What is therefore needed is the arrival direction of these protons, i.e. the AGN images. For this purpose the shooting procedure from section 4.2 is used.

In table 4.1 there are 20 Auger events correlating with 20 AGN. Some of the Auger events correlate to two or more AGNs making the total number of correlations 25.

25 protons are thus generated with the energies of the corresponding Auger events. For example, the 90.3 EeV Auger event in table 4.1 correlates with two AGNs. An energy of 90.3 EeV is thus assigned to the generated protons from these AGNs. This is shown in figure 4.4.

Figure 4.4 shows the 90.3 EeV and 57.4 EeV Auger events together with their correlating AGNs. AGN images at Earth, as conveyed by the arrival directions of two 90.3 EeV and one 57.4 EeV generated protons originating exactly from the AGNs are seen. The backtracked positions of the Auger events are also shown. The HMR ASS-A model is used.

Some mismatches are seen in figure 4.4. The AGN images (the arrival directions of protons originating exactly from the AGNs), shown as red crosses, are far away from the Auger data events. Provided that the HMR ASS-A model is more or less correct this indicates that the Auger events in figure 4.4 do not originate from the particular (claimed) AGNs. In addition, the back-

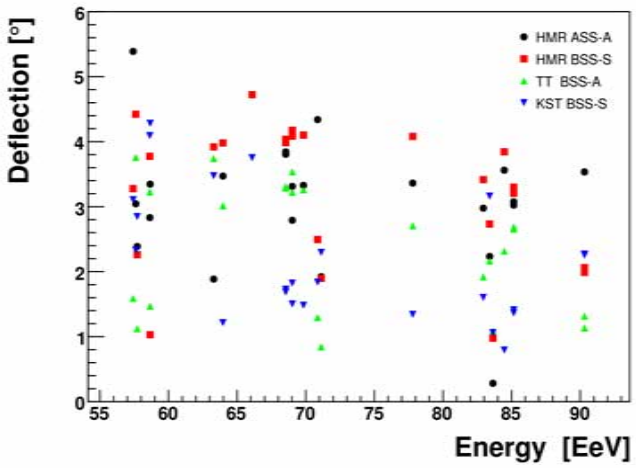

Figure 4.5: Deflection angles α_{image} between the AGN images at Earth and the real directions of the corresponding AGNs calculated for different models.

tracked positions of the Auger events should be close to their correlating AGNs. This is also not the case in figure 4.4.

The deflections of protons originating exactly from the AGNs are calculated by taking the scalar product of the AGN images and the directions of the AGNs,

$$\cos \alpha_{\text{image}} = \hat{u}_{\text{image}} \cdot \hat{u}_{\text{AGN}}, \tag{4.3}$$

where $\hat{u}_{\text{image}}$ is the AGN image (the arrival direction of a proton originating from a given AGN) and $\hat{u}_{\text{AGN}}$ is the AGN direction. The deflections, calculated for all the 25 generated protons using different models, are shown in figure 4.5.

The average deflections are 3.1, 3.3, 2.4, and 2.2° for HMR ASS-A, HMR BSS-S, TT BSS-A and KST BSS-S, respectively. The use of 3.2° circles in [99] is thus acceptable when magnetic deflections, as produced by the models here, are taken into account. This is however not sufficient to conclude that the Auger events originate from the particular AGNs. The AGN images should also be compatible with the directions of the Auger events (the first criterion in section 4.1). This is certainly not the case for the AGN images in figure 4.4. As noticed in chapter 2, different models and their configurations have different impacts on different energies and different regions of the sky. So, even if the deflections of the generated protons originating exactly from the original AGNs are compatible with Ψ, it is not given that their arrival directions (shooting directions) are compatible with the directions of the Auger events. As seen in figure 4.4 even the shooting direction of the generated 90.2 EeV proton fails the first criterion. Either the field strength is too large or the observed correlation between the 90.2 EeV Auger event and its corresponding AGNs is inaccurate.

In the next section the criteria defined in section 4.1 are checked for different models.

4.4 Magnetic deflections and Active Galactic Nuclei

Figure 4.6 shows the AGN images as observed on Earth, the true positions of the AGNs, Auger events and backtracked Auger events. The Auger events seem to be clustered together in three regions of the sky. These three regions are given by the red, blue and green rectangles. Here only the red region is studied. The figures of blue and green regions for different models are found in appendix B.

The energies of the Auger events are indicated in all the figures.

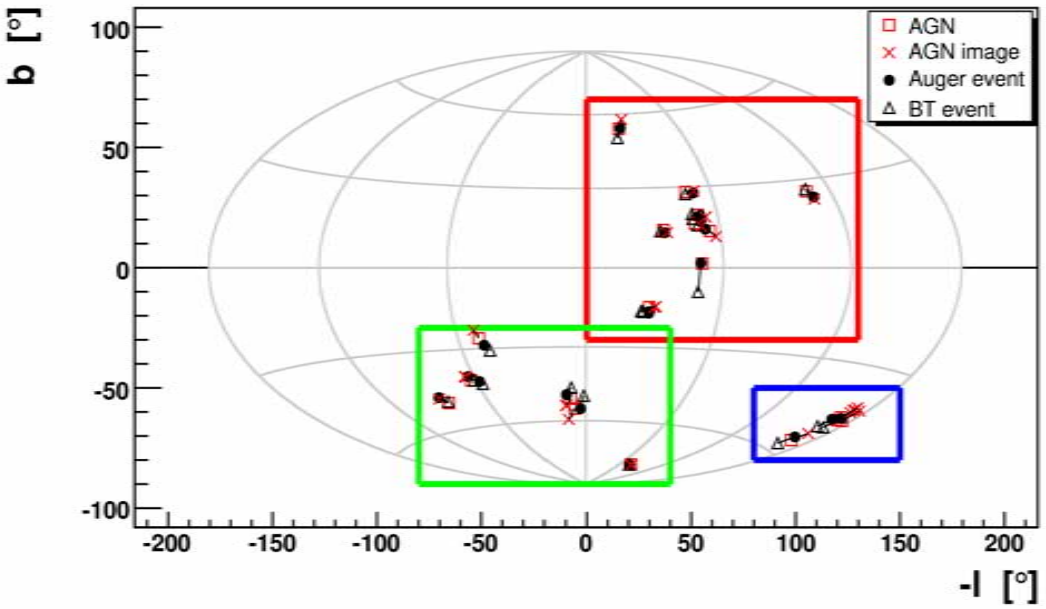

Figure 4.6: Sky map including the Auger data events (black dots), the backtracked Auger events (triangles), AGN images obtained with the shooting procedure (red crosses) and the AGN (red squares). Here the HMR ASS-A model is used. Three regions that will be enlarged in the following plots are denoted with rectangles of different color.

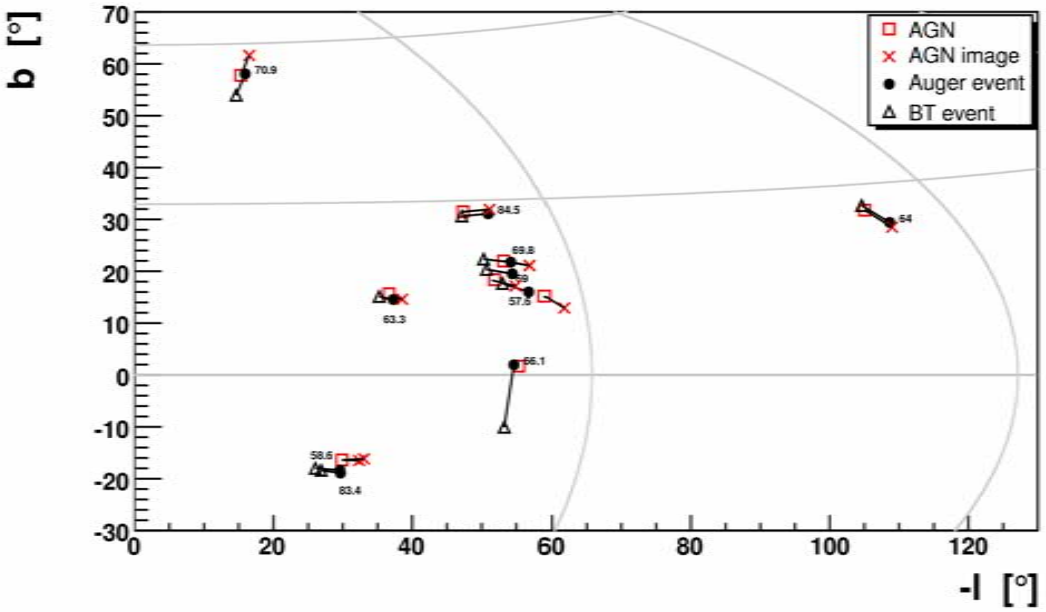

Figure 4.7: The first rectangle with red boundaries taken from figure 4.6. Here the HMR ASS-A model is used.

In figure 4.7 (HMR ASS-A model) the backtracked positions of the Auger events with energies of 64 and 84.5 EeV fulfill the second criterion. The first criterion is also satisfied as the Auger

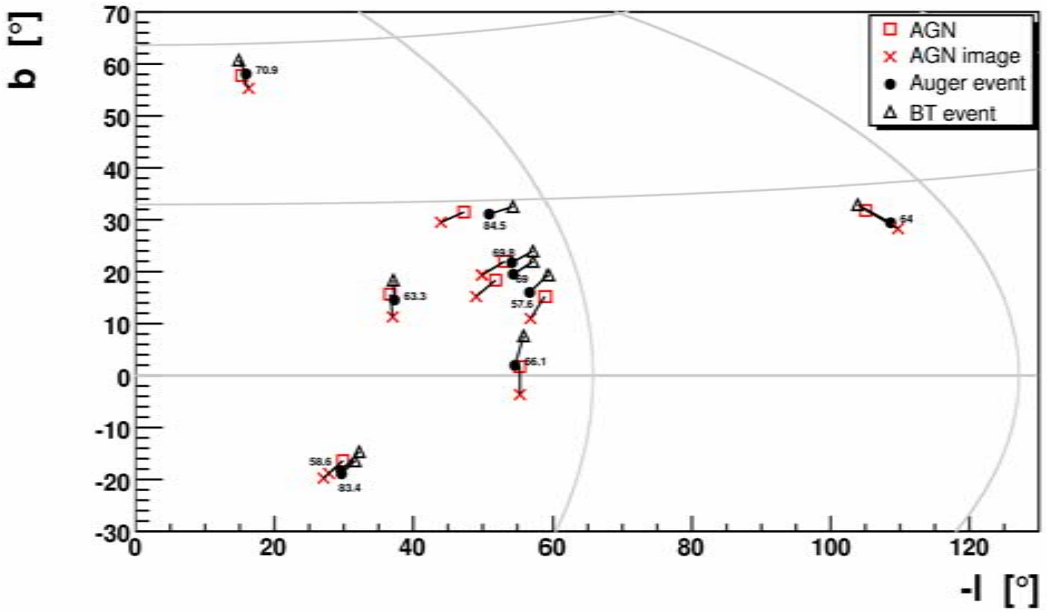

Figure 4.8: The first rectangle with red boundaries taken from figure 4.6. Here the HMR BSS-S model is used.

events practically have the same directions as the AGN images with less than 1° difference. The second criterion is fulfilled due to the high energies of these events. When backtracked these events are not sufficiently bent by the GMF model and thus their backtracked directions lie inside the 3.2° limit.

The remaining seven Auger events and their corresponding backtracked directions fail to meet one or both of the criteria. In the galactic regions around $b \approx 20°$ and $b \approx -20°$, the main deficiency is that the AGN images lie at lower galactic longitudes than the Auger events. Note that the AGN near the 66.1 EeV event in the vicinity of the galactic equator lacks its image at Earth. No minimum of equation (4.1) was found by the shooting procedure that could yield a shooting direction for a proton originating from this AGN. This is not surprising when looking at the exposure map in figure 2.21 in chapter 2. As mentioned before the huge black region in figure 2.21 is a blind spot for observers at Earth i.e. cosmic rays originating from extra-galactic sources in this region are unobservable at Earth. Clearly, the AGN in question lies in the middle of the blind region stretching several degrees in galactic latitude above and below the galactic equator. The angular separation between the backtracked 66.1 EeV event and its corresponding AGN is 10°, stressing the large size of the blind region.

While two Auger events (with their corresponding backtracked positions) in figure 4.7 passed the criteria when the HMR ASS-A model is used, only one of them does the same when the HMR BSS-A model is used, namely the 64 EeV event on the right side of figure 4.8. The backtracked positions of the 58.6, 63.3, 70.9, and 83.4 EeV events pass the second criterion. Note that the AGN near the galactic equator now has its image at Earth. As is seen in figure 2.22 there are no blind regions for the HMR BSS-S model at higher energies. Thus, in contrast to the HMR ASS-A model, it is perfectly well that the correlating AGN is situated near the galactic equator. However, the 66.1 EeV event and its backtracked position do not pass the criteria. The AGN image is located far below the Auger event position, while the backtracked position of the Auger event is located far above the AGN position. This implies that the field near the galaxy disk is too strong and of the opposite direction. A near-zero field is needed like in the HMR ASS-A case but with an extra-galactic exposure as high as in the HMR BSS-S case.

The 64 EeV Auger event (and its backtracked position) passes the criteria for the third model

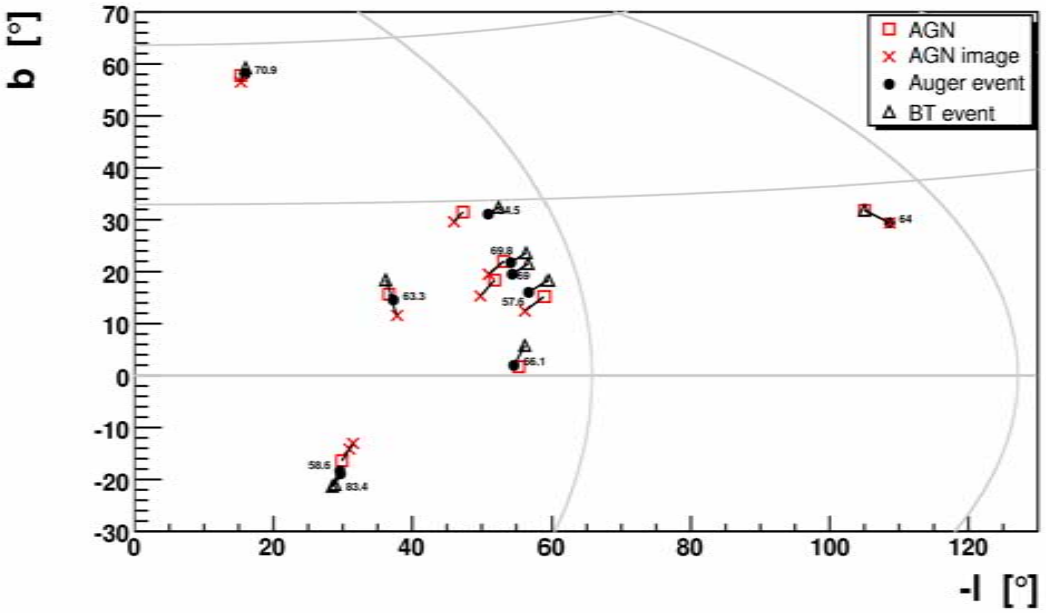

Figure 4.9: The first rectangle with red boundaries taken from figure 4.6. Here the TT BSS-A model is used.

in a row in figure 4.9. The backtracked positions of the 70.9, 63.3, 57.6, and 69 EeV events pass the second criterion.

The most striking feature with the TT BSS-A model is the region near the galactic equator. As is the case with HMR ASS-A model, the AGN in this region does not have an image at Earth. The blind region for the TT BSS-A model is smaller than the HMR ASS-A model for energies above 50 EeV as seen not only in figure 2.23 but also by comparing the backtracked positions of the 66.1 EeV event in figure 4.7 and 4.9. The backtracked position in figure 4.9 is closer to the plane since the blind region for the TT BSS-A model ends nearer to the plane. While the angular separation between the backtracked position of the 66.1 EeV event and its corresponding AGN is 10.5° in the HMR ASS-A model, in the TT BSS-A model this number is reduced to 3.7°.

The 64 EeV event and its backtracked position in figure 4.10 fails the criteria for the first time. The elaborate structure of the KST model also makes sure the 69 EeV event and its backtracked position passes both criteria for the first time for one of its correlating AGNs.

Finally, the backtracked positions of the 84.5 EeV, 83.4 EeV, 70.9 EeV, and 69.8 EeV events pass the second criterion.

The findings for all models and all regions in figure 4.6 are summarized in figures 4.11 to 4.14. The left plots show the angular distances between the backtracked positions of the Auger events and the their corresponding AGNs (second criterion) while the right plots show the angular distances between the AGN images and the corresponding correlating Auger events (first criterion).

The average angular separation between the backtracked positions of the Auger events and their corresponding AGNs is 3.6°, 3.7°, 3.0°, and 2.8° for HMR ASS-A, HMR BSS-S, TT BSS-A, and KST BSS-S models, respectively. However, the *number* of times criterion two is passed is very similar for all the models. This number is 12, 11, 14, and 15 for HMR ASS-A, HMR BSS-S, TT BSS-A, and KST BSS-S models, respectively.

Criterion one is satisfied only once for the HMR BSS-A and TT BSS-S models while this number for the HMR ASS-A and KST BSS-S models is four.

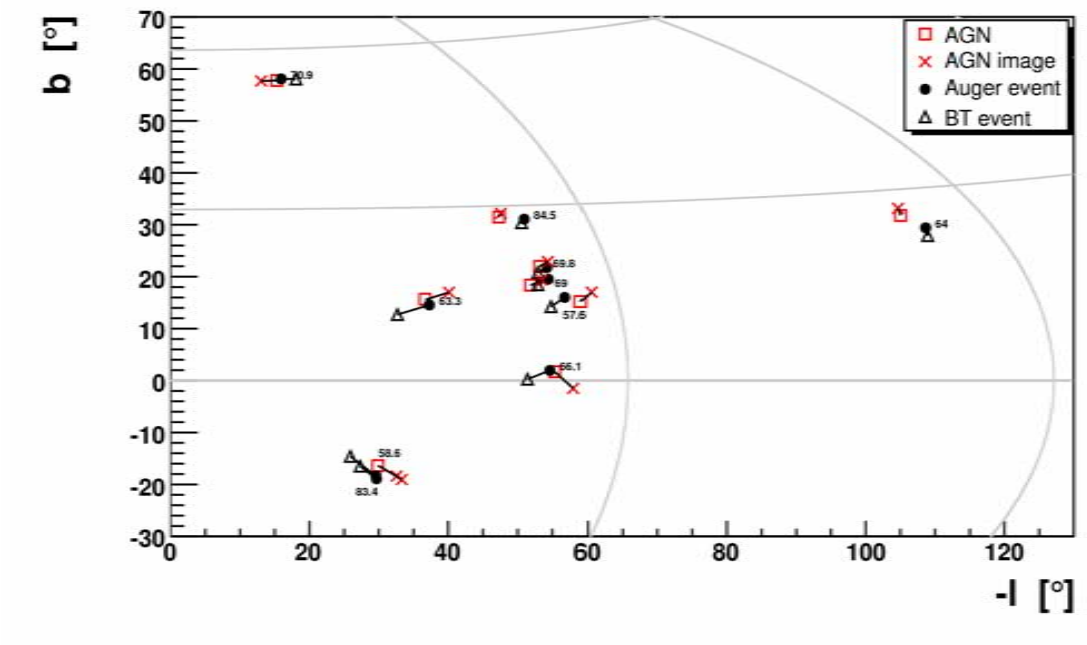

Figure 4.10: The first rectangle with red boundaries taken from figure 4.6. Here the KST BSS-A model is used.

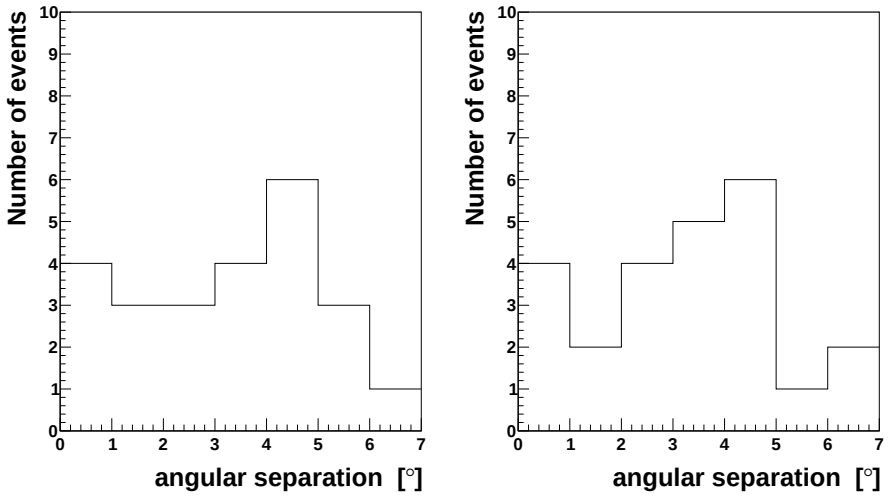

Figure 4.11: Left plot: The angular separations of the backtracked Auger events to their corresponding AGNs. Right plot: The angular distances between the AGN images and the corresponding correlating Auger events. The HMR ASS-A model is used for both plots. These plots should be compared to figure 4.1.

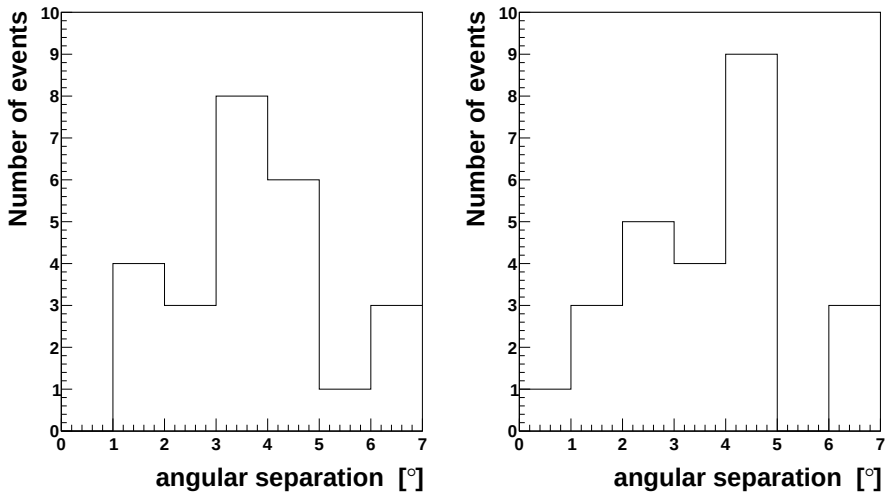

Figure 4.12: Left plot: The angular separations of the backtracked Auger events to their corresponding AGNs. Right plot: The angular distances between the AGN images and the corresponding correlating Auger events. The HMR BSS-S model is used for both plots. These plots should be compared to figure 4.1.

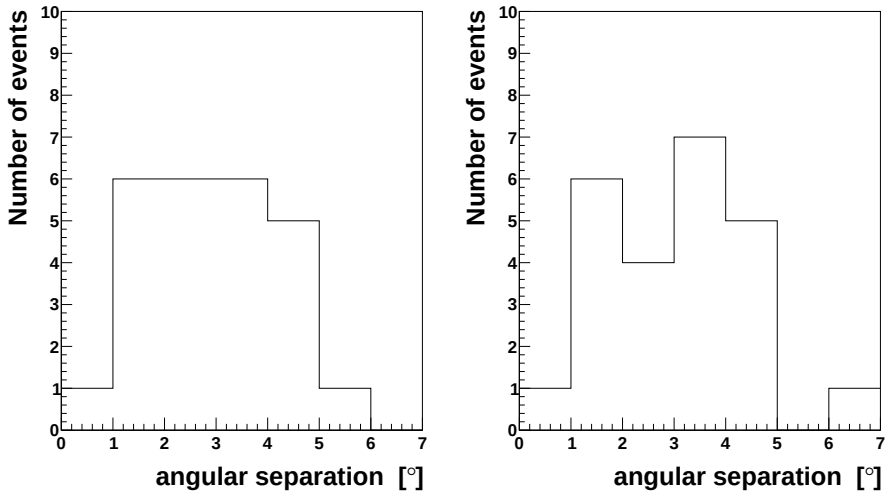

Figure 4.13: Left plot: The angular separations of the backtracked Auger events to their corresponding AGNs. Right plot: The angular distances between the AGN images and the corresponding correlating Auger events. The TT BSS-A model is used for both plots. These plots should be compared to figure 4.1.

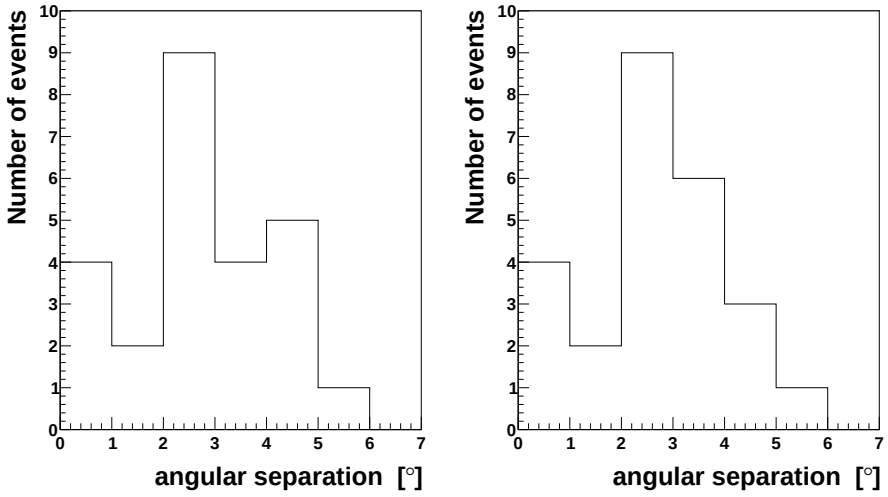

Figure 4.14: Left plot: The angular separations of the backtracked Auger events to their corresponding AGNs. Right plot: The angular distances between the AGN images and the corresponding correlating Auger events. The KST BSS-S model is used for both plots. These plots should be compared to figure 4.1.

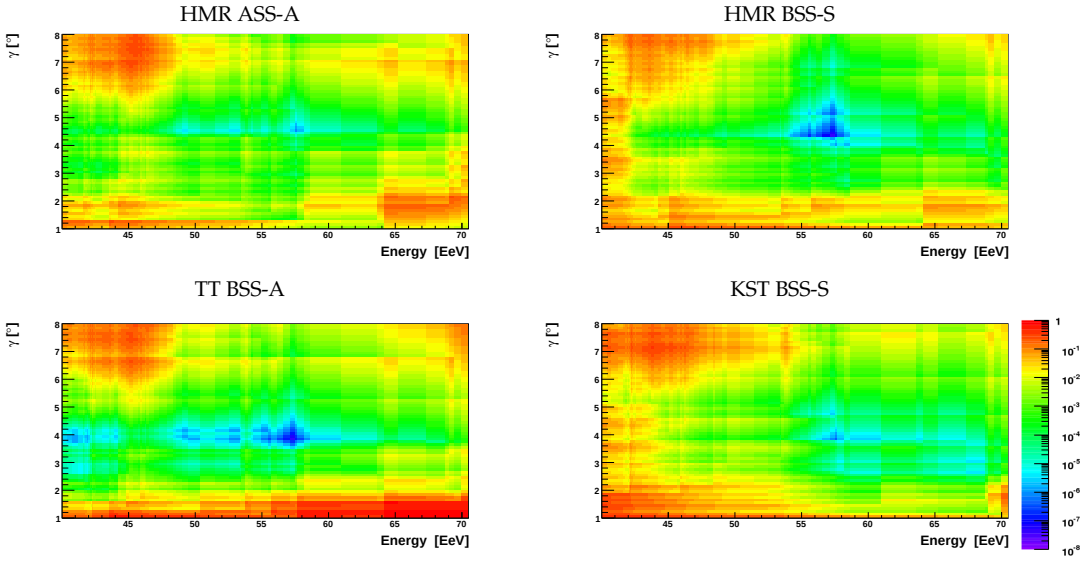

Figure 4.15: Plots showing the scan probabilities for different GMF models as a function of angular distances and energy. The minimum probability in all the plots is set to 10^{-8}.

4.5 Magnetic deflections and UHECR-AGN correlation

In this section the scan is repeated for Auger data from the period of 1 January 2001 to 31 August 2007. The data set is first backtracked in different models before scanning. The data is thus corrected for magnetic deflections caused by the GMF models. As in [98, 99, 100] only Auger events with larger energies than 40 EeV are used. Figure 4.15 shows the scan probabilities for different angles and energies and for different models. The cut is made on $z_{\max}$ obtained by the scanning procedure for different models. The results are summarized in table 4.2.

The minimum probability is obtained for angular distances that are remarkably similar to the one found by the PAO, lying in the range 3.8 to 4.5 degrees. The same holds true for the minimum energy of $E_{\min} = 57.4$ EeV for the HMR ASS-A and TT BSS-A models. This is exactly the same minimum as the one found for uncorrected data. The HMR ASS-A and KST BSS-S models yield a slightly larger cut, $E_{\min} = 57.6$ EeV. Consequently, there are 26 Auger events above $E_{\min} = 57.6$ EeV while there are 27 for the former cut. Due to these cuts the minimum scan probability differs between the models.

For the HMR ASS-A model the minimum probability in the scan is obtained by an angular separation of 4.5 degrees. As a result more Auger events are expected to correlate with the AGNs compared to the other models. An expected number of 8.6 events and a total of 21 observed events yield a minimum scan probability that is higher relative to the other models. This is also seen in figure 4.15. A minimum probability of $7.95 \cdot 10^{-7}$ is seen for the HMR ASS-A model at around 57 EeV. For the KST BSS-S model the minimum probability is very similar, namely $4.73 \cdot 10^{-7}$. In comparison, the minimum probability from [98, 99] is $4.5 \cdot 10^{-9}$.

These minimum probabilities are around one order of magnitudes larger than the minimum probabilities obtained for the TT BSS-A ($3.83 \cdot 10^{-8}$) and HMR BSS-S ($4.06 \cdot 10^{-8}$) models.

The similarities of the minimum probabilities of the HMR ASS-A and KST BSS-S models on one hand, and HMR BSS-S and TT BSS-A on the other might be explained by the minimum energy cut, $E_{\min}$. As noted $E_{\min}$ is 57.6 EeV for the HMR ASS-A and KST BSS-S models, and 57.4 EeV for the HMR BSS-S and TT BSS-A models.

This energy cut might also be used to make a judgment on the UHECR-AGN correlation and the GMF models. The energy cut was originally introduced in the scan to remove Auger events that are susceptible to large magnetic deflections [98, 99]. By correcting the Auger events for

Model	$E_{\min}$ [EeV]	N	$\Gamma_{\max}[^\circ]$	$z_{\max}$	N_{obs}	N_{exp}	$P_{\min}[\cdot 10^{-10}]$
No model	57.4	27	3.2	0.017	20	5.6	45
HMR ASS-A	57.6	26	4.5	0.017	21	8.6	7950
HMR BSS-S	57.4	27	4.3	0.013	20	6.4	406
TT BSS-A	57.4	27	3.8	0.017	21	7.1	383
KST BSS-S	57.6	26	3.8	0.013	17	5.1	4734

Table 4.2: The new scan parameters after correcting for magnetic deflections for different models. N is the total number of events above the energy cut, N_{exp} is the expected number of chance correlations, $z_{\max}$ is the maximum redshift, $\Gamma_{\max}$ is the maximum angular separation between the AGNs and the Auger events, and $P_{\min}$ is the minimum binomial scan probability.

magnetic deflections a smaller energy cut is expected *if* the UHECR-AGN correlation is correct. As seen in table 4.2 the $E_{\min}$ for the different models, however, is either equal or close to equal the value for $E_{\min}$ found in data. This has two implications. Either the UHECR-AGN correlation is not real or the GMF models are not accurate descriptions of the field.

4.6 Conclusion

In section 4.3 it is established that the size of the correlation circles $\Psi = 3.2^\circ$ found by PAO [98, 99] is reasonable after calculating the magnetic deflections of protons originating exactly from the AGNs.

In section 4.4 the criteria defined in the introduction are checked. The models meet the criteria poorly.

After correcting the incoming directions of data for the deflections as predicted by the four models, 11 to 15 backtracked events remain inside the correlation circles of size 3.2°.

Only four AGN images match the directions of the corresponding correlated Auger events in the HMR ASS-A and KST BSS-S model, while for the other two models this number is only one.

More importantly only 4 Auger events meet both criteria for the HMR ASS-A and KST BSS-S models. This number is only 1 for the TT BSS-A and HMR BSS-S models.

It is also shown that for models with field reversals along the z-directions, protons originating from AGNs close to the galactic equator do not reach Earth. Hence, if these models describe a realistic configuration of the GMF the 66.1 EeV event and its corresponding AGN in table 4.1 are not correlated.

As noted, the number of Auger events passing both criteria is highest for the HMR ASS-A and KST BSS-S configurations. This did not prevent the scanning procedure to yield the highest scan probabilities for these two models. This is clearly due to the slightly higher energy cuts obtained for the HMR ASS-A and KST BSS-S models. Conversely the TT BSS-S yields the lowest minimum probability despite only one events passed both criteria for this model. The HMR BSS-S model yields the second lowest minimum probability.

The corrected minimum scan probabilities for the different models are comparable to the minimum probability found by PAO. If the observed UHECR-AGN correlation is real the probabilities in table 4.1 should be lower, and a lower value of $E_{\min}$ would be expected, provided that the models are accurate. Since this is not the case two scenarios are possible:

- The GMF models are not accurate descriptions of the field.
- The Auger data do not correlate with AGNs but most probably with some other astronomical objects.

Here it is assumed that the UHECRs are protons. How the UHECR-AGN correlation changes when other composition assumptions are made, is discussed in the references [104, 105, 106].

Chapter 5

Thread-like Multiplets

5.1 Introduction

One of the main goals of the Pierre Auger experiment is to find the sources of UHECRs. Assuming that the highest energy cosmic rays have an extra-galactic origin any enhancement of the cosmic ray flux for a given direction or region might also indicate the position of the source. But this is difficult to detect due to the rarity of such energetic events. In addition, it was shown in chapter 2 that the galactic magnetic field makes the exposure to the extra-galactic sky highly non-uniform even for high energetic protons. Regional flux enhancement induced by the galactic magnetic field might therefore be confused for detection of a source, making it even more vital to collect as many cosmic rays with the highest energies as possible. The Auger aperture and its superior detection area will ensure that more charged particles at EeV-scale are collected than in all previous experiments. Still, this rate is lower than what is needed for a direct detection.

One of the expected possible effects of the galactic magnetic field is the forming of thread-like multiplets of arrival directions. Theoretically, this should occur when cosmic rays of different energies originate from a common point-like source, as shown in section 4.2. Particles with sufficient energy in such a cluster point straight back to the common source due to the relatively small deflections. For decreasing energies the arrival directions are shifted and a thread-like structure of multiplet should appear. A linear fit to such a structure should in principal yield the source position. Thread-like multiplets might thus become a powerful tool in cosmic ray astronomy.

In the search for thread-like multiplets, Harari, Mollerach and Roulet [108, 109, 110] constructed a Minimal Spanning Tree (MST) by using the arrival directions of the Auger data. The MST does not in itself find thread-like multiplets, rather it yields localized clusters of arrival directions. The clusters are investigated further and consequently some thread-like structures and their potential sources are found. Appendix C explains this method in detail.

Here the MST is constructed with the arrival directions of the Auger data events from January 2004 until the end of 2008. A MST is constructed from these arrival directions in such a way that the total length between the first chosen arrival direction and last is minimal [108, 109, 110]. The MST has no loops and is unique [108]. The size of the tree, i.e. the number of arrival directions constituting the tree, is governed by the energy cut $E_{\min}$ where energies below this cut are removed. The angular distance d between two arrival directions constituting the MST is called a "branch" length. The average branch length of the MST is denoted as $\langle d \rangle$. In order to get clusters of arrival directions, branches in the MST are cut away if they are larger than some defined fraction of the mean length. These clusters are projected into a tangential plane on the celestial sphere through the gnomonic projection [111] and rotated so that thread-like clusters are found along a longitudinal coordinate z (see appendix C for details). As the deflection at high energies is a function of $1/E$, the correlation coefficient $C\left(z, 1/E\right)$ for the longitudinal coordinate z and $1/E$ is calculated. The clusters are more and more elongated for higher values of $C\left(z, 1/E\right)$. Here the limit of the correlation coefficient is set to $C\left(z, 1/E\right) > 0.95$ and thus only the very thread-like

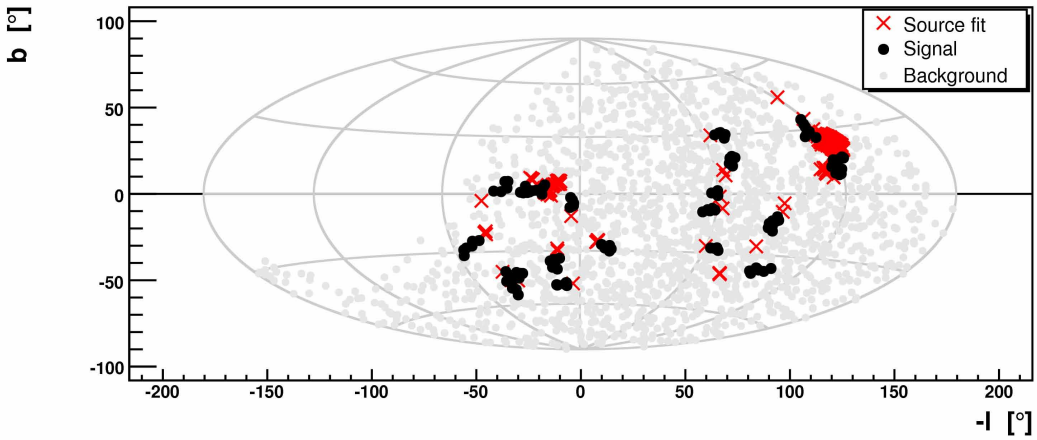

Figure 5.1: Thread-like multiplets obtained for $E_{\min} = 15\,\text{EeV}$ and $d_{\max} = \langle d \rangle$. Multiplicity of the multiplets is larger than or equal to 5. The sources obtained by linear fits are denoted by the red crosses (source fit).

clusters remain. These are denoted as thread-like multiplets or simply *threads*. In large clusters, however, several threads might be found as the events in the cluster can satisfy $C\,(z, 1/E) > 0.95$ by combining with each other in different ways. Auger events forming threads are called signal events. Auger events not forming threads are called background events. Threads are fitted with a linear function in $1/E$ (inverse energy). This is denoted as *source fit*. The source fit gives the source position of the thread and deflection power D, indicating the deflection size.

To sum up, the following definitions are used in the following sections.

- $E_{\min}$ is the minimum energy cut removing arrival directions of Auger events with energies below this cut.
- $d_{\max}$ is the cut on the maximum branch length and is given by some fraction of the average branch length $\langle d \rangle$ of the MST. Branch lengths above $d_{\max}$ are removed.
- Signal event is an Auger event that is part of a thread-like multiplet.
- Background event is an Auger event that is not part of a thread-like multiplet.
- Source fit gives the source position of the events in the thread.

In the following sections the positions of the sources, obtained by source fits, are compared to the positions of the backtracked signal events constituting the threads. Also here the signal events are assumed to be protons.

5.2 Cuts

As noted in the introduction and in appendix C, the total number of threadlike multiplets is a function of the $E_{\min}$ and $d_{\max}$ cuts. This is demonstrated in figures 5.1 to 5.7, showing the Auger events forming thread-like multiplets, denoted as "signal", and the sources obtained by fitting. "Background" designates all the Auger events surviving the energy cuts but are not part of any thread-like multiplets. It is also noted that there is no way to know what the appropriate values of these cuts are, i.e. the cut values that produce genuine thread-like multiplets. To determine if a thread-like structure is genuine or not, the probability of finding such a structure by chance (section 5.6) has to be evaluated. Another way to check if thread-like multiplets are genuine or not is by assuming that the MST procedure produces sources accurately *and* that the GMF

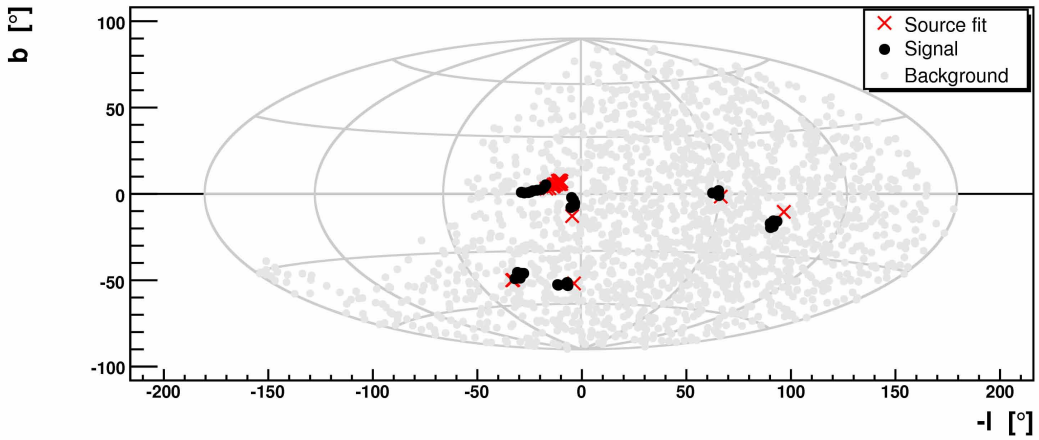

Figure 5.2: Thread-like multiplets obtained for $E_{\min} = 15\,\text{EeV}$ and $d_{\max} = 0.8\,\langle d \rangle$. Multiplicity of the multiplets is larger than or equal to 5. The sources obtained by linear fits are denoted by the red crosses (source fit).

is accurately described by a given model (section 5.3). If this assumption is correct then the backtracked position of the signal events forming a given thread should converge at the source position. In this section, cuts are applied in order to find thread-like multiplets that are further investigated in section 5.3 and 5.6.

The cuts are set to $E_{\min} = 15\,\text{EeV}$ to $E_{\min} = 30\,\text{EeV}$ for the energies and $d_{\max} = \langle d \rangle$ and $d_{\max} = 0.8\,\langle d \rangle$ for the branch lengths. The minimum multiplet size is set to five events.

The 15 EeV cut yields 1799 events from data. Out of these, 125 events form the multiplets in figure 5.1. Two large groups of sources around the $l \approx -120°$ and near the galactic center are observed. As noted in appendix C, after the tree is cut some clusters may contain a large number of events. The MST procedure is only able to produce the source position by fitting threads. The events in a large cluster thus might combine in many ways yielding several threads and several sources. However, it is an implicit assumption that threads found in each large cluster has a common source. This common source position of the threads in a cluster is thus unknown but the distribution of the sources obtained by fitting might indicate approximately where the source of the threads is located. Events of the clusters not being part of any thread, denoted as "background", are also seen in figure 5.1. Disjoint groups of threads are clearly visible. These groups are the remaining parts of the original clusters given by the MST procedure.

The two mentioned source groups are a result of two corresponding large groups of threads.

In figure 5.2 the branch length cut of $d_{\max} = 0.8\,\langle d \rangle$ reduces the amount of thread-like multiplets substantially. The remaining multiplets are constituted by 35 signal events. An interesting long string of signal events is situated near the galactic center. These nine events form, by different combinations, three septuplets, twelve sextuplets and twenty-nine quintuplets. This configuration is analysed in the next section.

For the 20 EeV cut, figures 5.3 and 5.4 display no large number of sources. In figure 5.4 three quintuplets remain. The 15 signal events constituting the three quintuplets are also present in figures 5.1 and 5.3. In figure 5.2 two of these events with the energies 38 EeV and 53.8 EeV, are present near the galactic center.

By increasing the cut to $E_{\min} = 25\,\text{EeV}$ only 13 signal events are present. However, a new large grouping of sources, caused by seven signal events, appears near the galactic center in figure 5.5. In addition, the two signal events with the energies 38 EeV and 53.8 EeV are again present, demonstrating the resiliency of these events after having appeared on all figures except for figure 5.6. The other 6 signal events are responsible for a sextuplet and three quintuplets. These signal events are also the sole survivors of the $d_{\max} = 0.8\,\langle d \rangle$ cut as shown in figure 5.6.

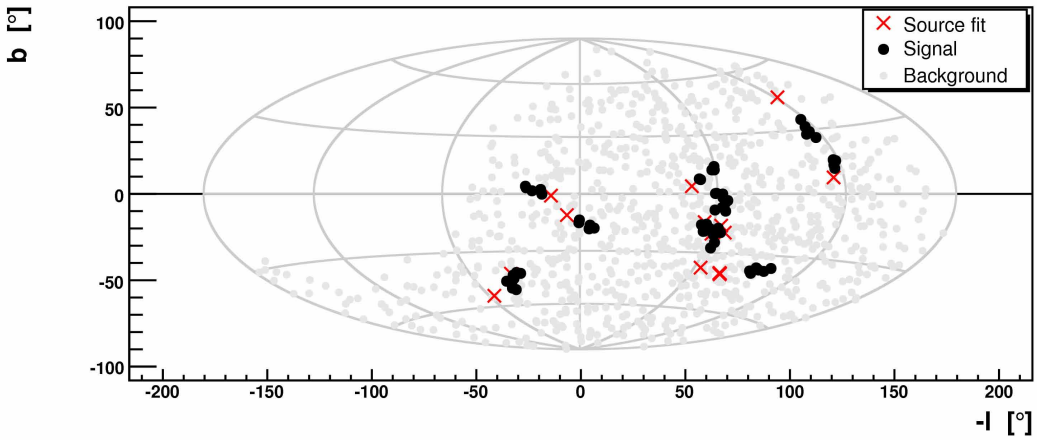

Figure 5.3: Thread-like multiplets obtained for $E_{\min} = 20\,\text{EeV}$ and $d_{\max} = \langle d \rangle$. Multiplicity of the multiplets is larger than or equal to 5. The sources obtained by linear fits (source fit) are denoted by the red crosses.

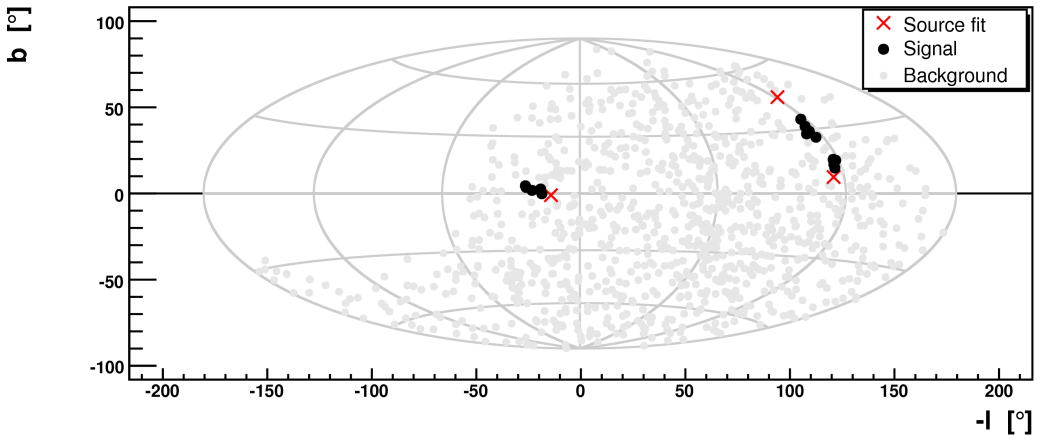

Figure 5.4: Thread-like multiplets obtained for $E_{\min} = 20\,\text{EeV}$ and $d_{\max} = 0.8\,\langle d \rangle$. Multiplicity of the multiplets is larger than or equal to 5. The sources obtained by linear fits (source fit) are denoted by the red crosses.

Figure 5.7 is showing four sources due to four quintuplets and is by far the most interesting plot in this section. After the publication of the Science paper [98] of the Pierre Auger Collaboration, demonstrating the correlation between cosmic rays and AGNs, T. Wibig and A. W. Wolfendale [112] noted that the majority of the Auger data events are scattered into three regions as seen in figure 5.8. Each region is associated with distinctive nearby radio galaxies or possible known/unknown radio contenders, favored by the authors as sources of the cosmic rays. Region A is associated with Centaurus A. Two radio galaxies in the Fornax cluster are thought to be the possible sources in region B while in region C there are no clear candidates. The potential sources present in figure 5.7 correspond nicely to region A. Centaurus A, marked as a green cross, is partly hidden by one of the multiplets.

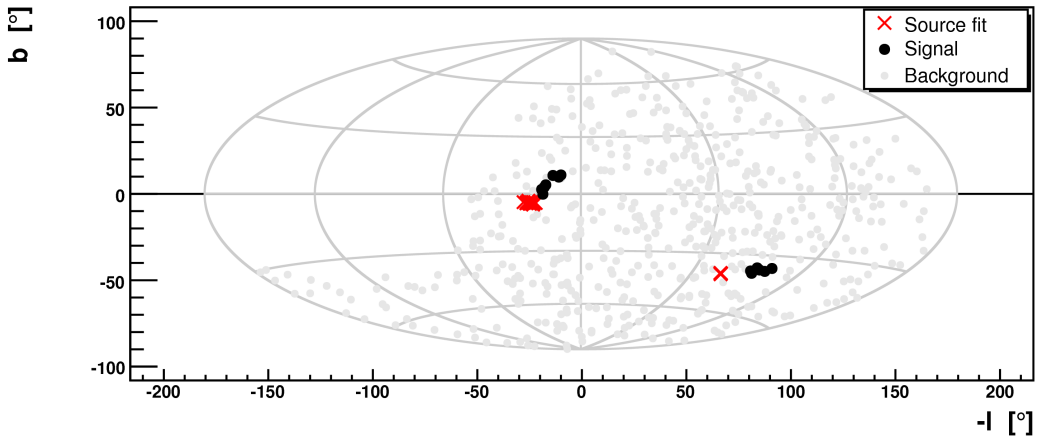

Figure 5.5: Thread-like multiplets obtained for $E_{\min} = 25\,\text{EeV}$ and $d_{\max} = \langle d \rangle$. Multiplicity of the multiplets is larger than or equal to 5. The sources obtained by linear fits (source fit) are denoted by the red crosses.

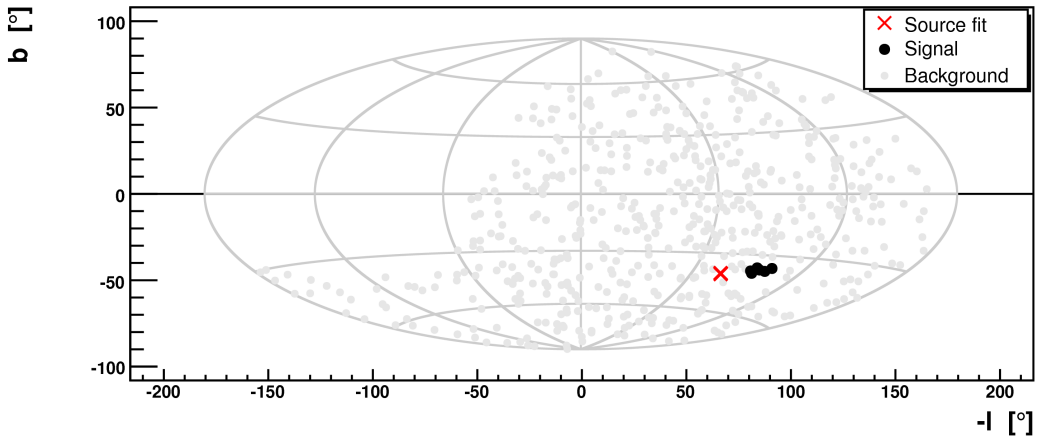

Figure 5.6: Thread-like multiplets obtained for $E_{\min} = 25\,\text{EeV}$ and $d_{\max} = 0.8\,\langle d \rangle$. Multiplicity of the multiplets is larger than or equal to 5. The sources obtained by linear fits (source fit) are denoted by the red crosses.

5.3 The galactic magnetic field models and threadlike multiplets

In this section the cuts in section 5.2 are applied on Auger data. The resulting signal events forming the multiplets/threads are then backtracked in different galactic magnetic field configurations and compared to the sources obtained by fitting. If the MST procedure produces the sources accurately and if the GMF is described accurately by a model, then the signal events forming the multiplets, when backtracked, should converge at the source positions.

The multiplets are tracked until a distance of 20 kpc from the galactic center is exceeded. The velocities of the tracked events and the sources obtained are shown in the figures 5.10 to 5.16.

A similar study was conducted in [109] where a single octuplet was backtracked in a modified Stanev BSS-A model with $B_z = 0.15\,\mu\text{G}$ yielding a common "source". In addition, similar results were achieved by changing the periodicity of the same model [109].

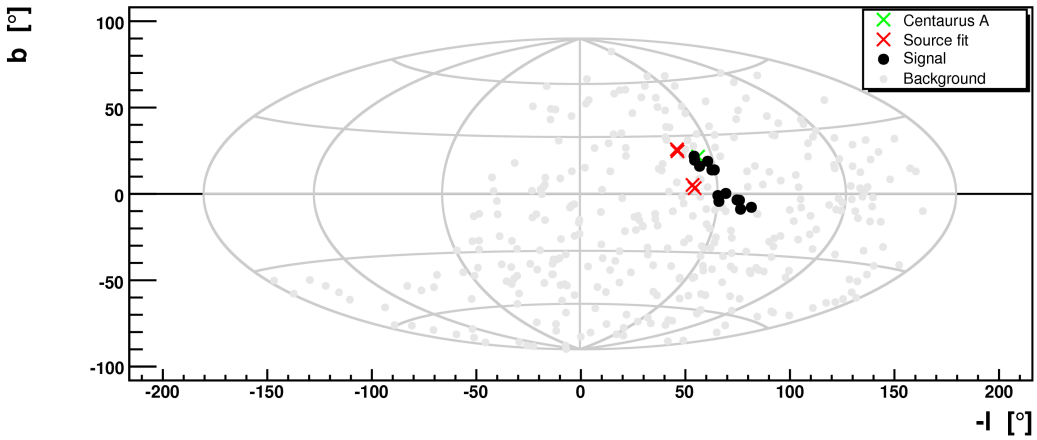

Figure 5.7: Thread-like multiplets obtained for $E_{\min} = 30\,\text{EeV}$ and $d_{\max} = 1\,\langle d \rangle$. Multiplicity of the multiplets is larger than or equal to 5. The sources obtained by linear fits (source fit) are denoted by the red crosses. Centaurus A is indicated by a green cross.

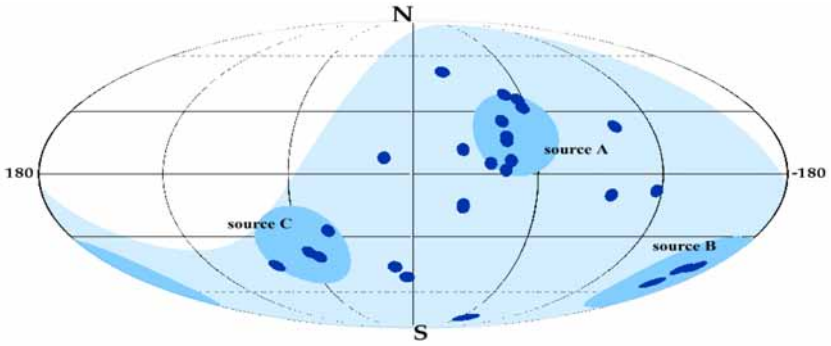

Figure 5.8: Sky map from [112] showing Auger events from [98] in three regions.

5.3.1 Cut: $\mathbf{E_{min} = 15\,EeV}$ and $\mathbf{d_{max} = 0.8\,\langle d \rangle}$

The cuts applied in this section yield the groups with thread-like multiplets in figure 5.9. The signal events with the highest energy in every thread are also shown. Note the group of nine signal events at the galactic plane. As noted in section 5.2, it is assumed that the threads in a group have a common origin. However after fitting, all the threads yield a source each. Luckily the source positions are highly focused, as seen in figure 5.3, indicating the source position of the entire group. If the signal events in a given group indeed originate from a common source the backtracked positions of these events thus should focus into the source positions obtained by a linear fit to the threads themselves. The signal events are backtracked in different models and the results are shown in the next figures.

In figure 5.10 the HMR ASS-A model yields particle velocities that, when projected to the sky, are either moving perpendicularly to the source positions or that are moving in the opposite direction, away from the sources.

For signal events near or at the galactic plane the perpendicular direction of the velocities is due to the extra-galactic exposure produced by the HMR ASS-A model. As was shown in figure 2.21 in chapter 2, cosmic rays originating from extra-galactic sources located around a large part of the galactic equator are not accessible to observers at Earth. This blind region, however, gets smaller with higher energies. By backtracking signal events with different energies situated in

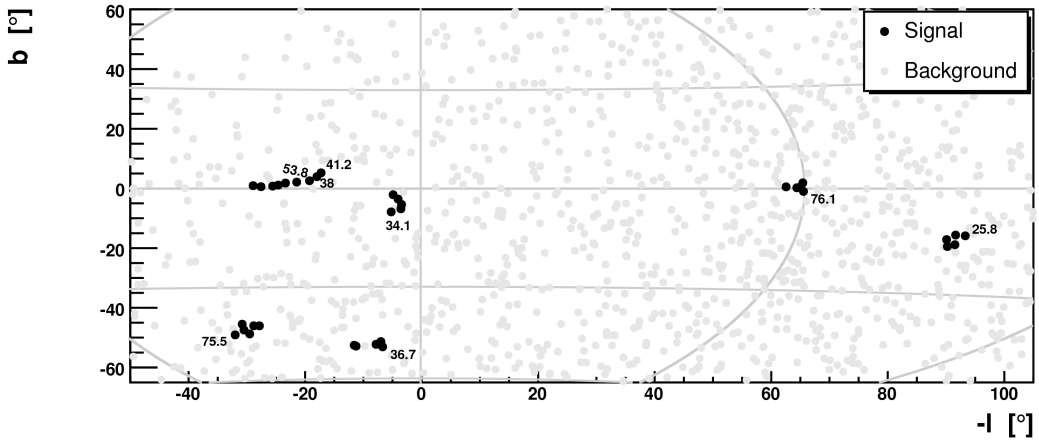

Figure 5.9: Thread-like multiplets obtained by $E_{\min} = 15\,\text{EeV}$ and $d_{\max} = 0.8\,\langle d \rangle$. Multiplicity is equal or larger than 5. The numbers indicate the energies of the highest energy events in the threads.

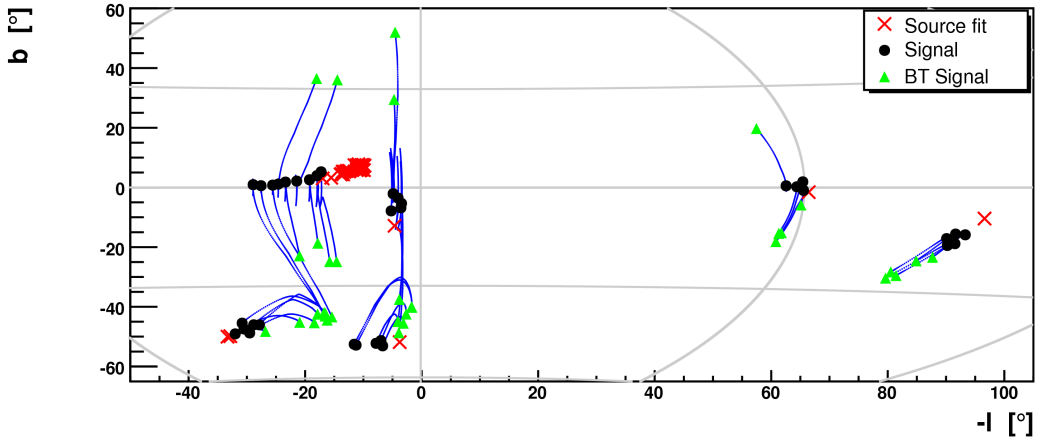

Figure 5.10: Thread-like multiplets obtained by $E_{\min} = 15\,\text{EeV}$ and $d_{\max} = 0.8\,\langle d \rangle$. Multiplicity is equal or larger than 5. The sources obtained by linear fits are denoted by the red crosses (source fit). HMR ASS-A model is used. The blue dots indicate the evolution of the velocity vector.

the blind region a spectroscopic effect is seen. As an illustration of this effect the backtracked positions of the three highest energy signal events in the string of nine events in figure 5.9 should be compared to each other. These three signal events have the energies 38 EeV, 41.2 EeV and 53.8 EeV. With figure 2.21 in mind a spectroscopic effect is clearly seen for the backtracked positions of these signal events near the galactic plane in figure 5.10. The 38 EeV and 41.2 EeV signal events are backtracked further away than the 53.8 EeV event. Events with lower energies are backtracked further away since the extra-galactic exposure is lower at these energies. Thus, the backtracked positions of the highest energy events are closer to the galactic disk. The remaining multiplets at situated well inside the extra-galactic exposure.

For the group with the 36.7 EeV signal event at $(l = 10°, b = -55°)$ the velocities, initially moving away from the source, make a turn of almost 90° around $l = 5°$ and propagate towards the source. The position of the source is not reached but at least the propagation direction is correct.

In figure 5.11 the velocities tend to point towards the galactic north pole since the field does

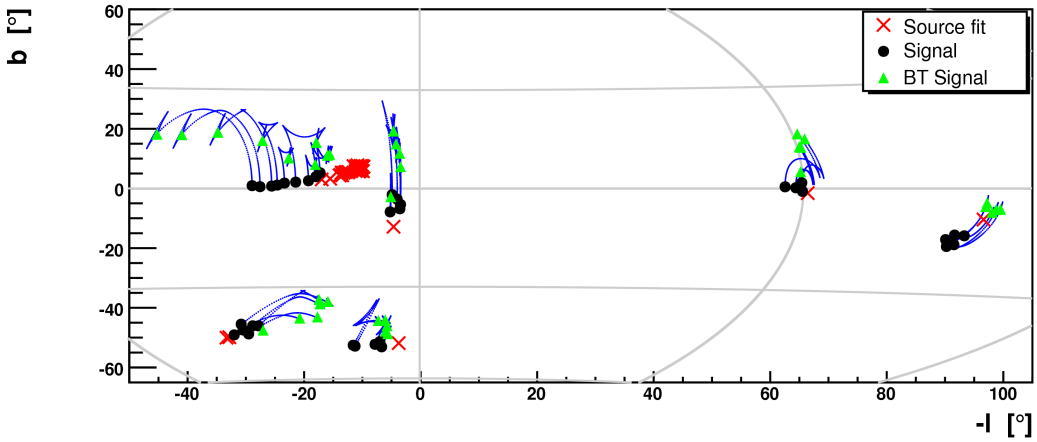

Figure 5.11: Thread-like multiplets obtained by $E_{\min} = 15\,\text{EeV}$ and $d_{\max} = 0.8\,\langle d \rangle$. Multiplicity is equal or larger than 5. The sources obtained by linear fits are denoted by the red crosses (source fit). HMR BSS-S model is used. The blue dots indicate the evolution of the velocity vector.

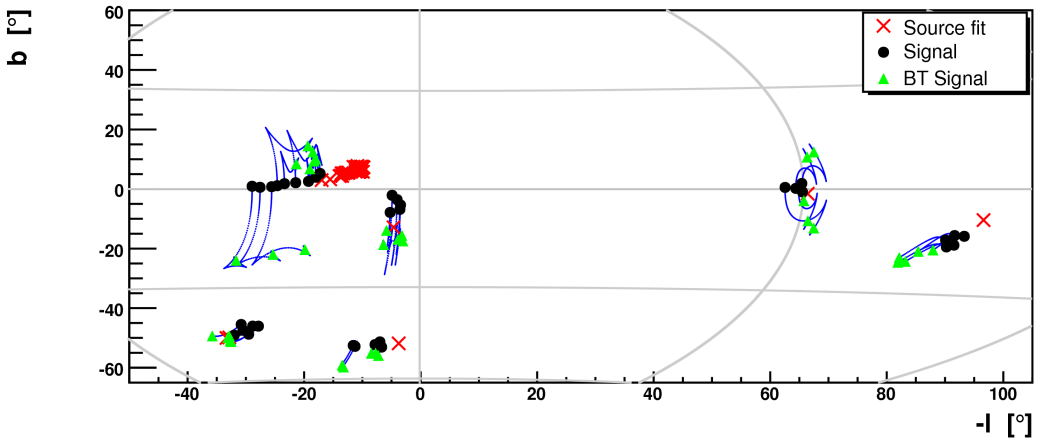

Figure 5.12: Thread-like multiplets obtained by $E_{\min} = 15\,\text{EeV}$ and $d_{\max} = 0.8\,\langle d \rangle$. Multiplicity is equal or larger than 5. The sources obtained by linear fits are denoted by the red crosses (source fit). TT BSS-A model is used. The blue dots indicate the evolution of the velocity vector.

not change sign with respect to the z direction. Although the BSS-S configuration is very different from ASS-A, as its extra-galactic exposure shows in figure 2.22, most of the backtracked events are scattered away from the sources. Just like in figure 5.10 the backtracked signal events of the group at $(l = 10°, b = -55°)$ show a reasonable proximity to the source. The velocities bounce towards the source and the backtracked position of the events are much more focused and closer to the source than in figure 5.10. The backtracked positions of the (signal) events in the thread to the right at $(l = -95°, b = -20°)$ almost coincide with the source position[1].

The TT BSS-A model produces a highly non-uniform exposure, ensuring a high degree of scattering of the backtracked events. However, two exceptions are seen in figure 5.12. The backtracked positions of the threads at $(l = 30°, b = -50°)$ and $(l = 5°, b = -20°)$ coincide with the

[1]In the next section the spread of the backtracked positions of the signal events (in different groups) are calculated with respect to the positions of their respective sources. This is done in order to determine qualitatively how well the backtracked positions of the signal events match the source positions.

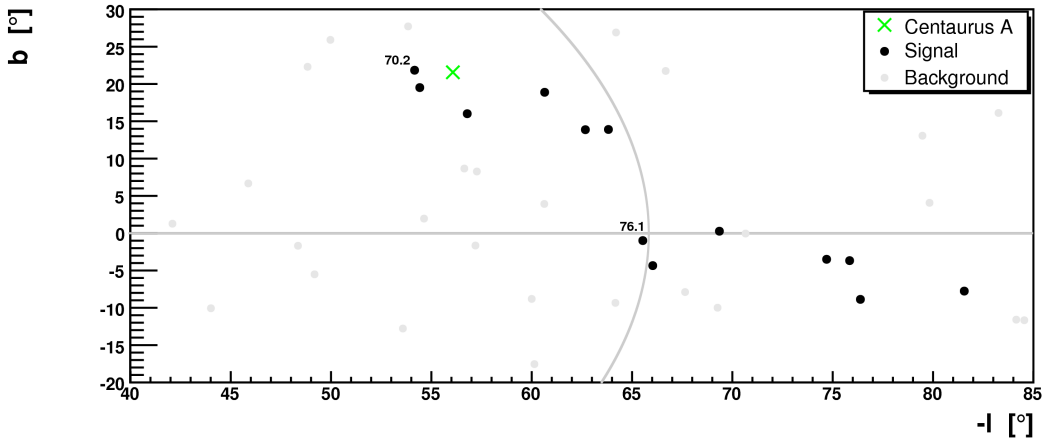

Figure 5.13: Thread-like multiplets obtained by $E_{\min} = 30\,\text{EeV}$ and $d_{\max} = \langle d \rangle$. Multiplicity is equal or larger than 5. The numbers indicate the energies of the highest energy events in the threads. The green cross shows the position of Centaurus A.

sources obtained by fitting.

If it is assumed that the MST produces the sources accurately then none of the models describe the real GMF accurately. The majority of the threads are found at the galactic disk in the figures above. As noted before, models with field reversals with respect to z produce highly non-uniform extra-galactic exposure at the galactic equator. Even if the HMR BSS-S model produces a much more uniform exposure, nevertheless only the single thread at $(l = -95°, b = -20°)$ has a backtracked position that corresponds to the source obtained by fitting.

If it is assumed that the models used in this sections are more or less accurate description of the galactic field, then the MST method is not yielding satisfactory results. In this case the multiplets formed are a result of chance or coincidence. This issue is further discussed in section 5.6.

5.3.2 Cut: $\mathbf{E_{min} = 30\,EeV}$ and $\mathbf{d_{max} = \langle d \rangle}$

The cuts applied in this section yield groups with thread-like multiplets in the Centaurus A region, as shown in figure 5.13. The position of Centaurus A is also indicated.

The backtracked events in the figures 5.14 to 5.16 miss the mark completely. However, in figure 5.14 the velocities of the backtracked events above the galactic plane propagate in the right direction but it seems that the deflections should be at least two times larger.

In figure 5.15 all the velocities point northwards and are in no way focusing towards the sources. In figure 5.16 all the velocities are moving away or perpendicular to the sources. If the threads from the Centaurus A region (region A) are genuine then the models are inaccurate. The probability of finding multiplets in region A is discussed in section 5.6.

5.4 Adjustment of the models

In this section the strength of the models is adjusted so that the backtracking of the Auger events yield positions that hopefully converge towards the source positions obtained by fitting threads.

Groups of signal events are chosen from figure 5.9 and 5.13. These are backtracked for different magnetic field strengths given by the adjusted models.

Four groups of signal events are selected for backtracking in the adjusted models. These are shown in figure 5.17 and 5.18. Group A (black rectangle) consists of 6 events that lay in a region

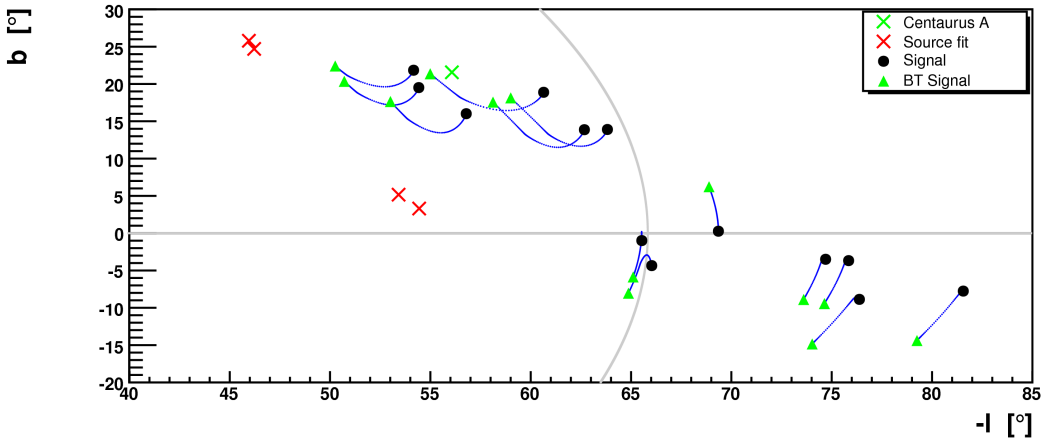

Figure 5.14: Thread-like multiplets obtained by $E_{\min} = 30\,\text{EeV}$ and $d_{\max} = \langle d \rangle$. Multiplicity is equal or larger than 5. The sources obtained by linear fits are denoted by the red crosses (source fit). HMR ASS-A model is used. The blue dots indicate the evolution of the velocity vector. The green cross shows the position of Centaurus A.

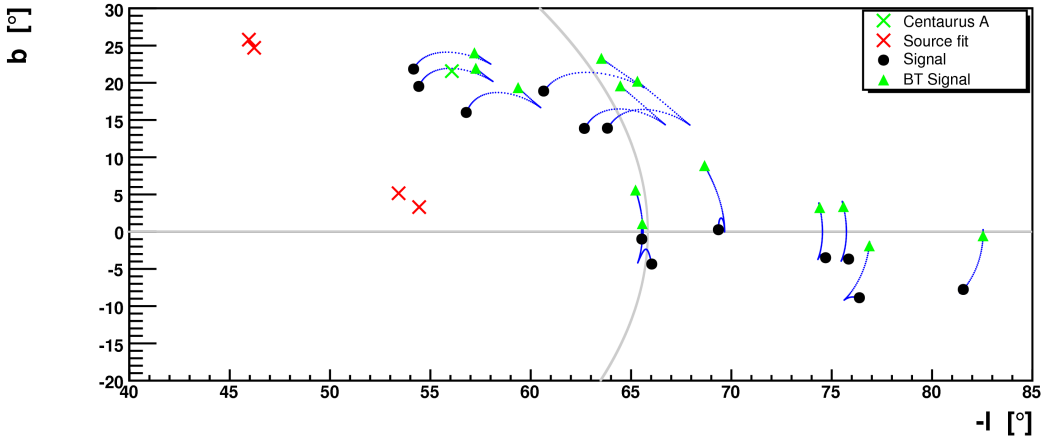

Figure 5.15: Thread-like multiplets obtained by $E_{\min} = 30\,\text{EeV}$ and $d_{\max} = \langle d \rangle$. Multiplicity is equal or larger than 5. The sources obtained by linear fits are denoted by the red crosses (source fit). HMR BSS-S model is used. The blue dots indicate the evolution of the velocity vector. The green cross shows the position of Centaurus A.

close to Centaurus A in figure 5.17. The 6 events combine in two different ways, giving two threads (quintuplets) and thus two sources after fitting.

In figure 5.18 three groups are selected. Group B (blue rectangle) is located at $(l = 30°, b = -50°)$ and has a highest energy signal event of 75.5 EeV. The group consists of 6 events forming two quintuplets.

Group C is located to the far right in figure 5.9 and has a highest energy signal event of 25.8 EeV. The group consists of a single thread (quintuplet) with a single source.

The string of nine events near the galactic center constitutes group D. As noted these nine events form, by different combinations, three septuplets, twelve sextuplets and twenty-nine quintuplets.

The fitting procedure also yields the deflection power D as defined in appendix C. The aver-

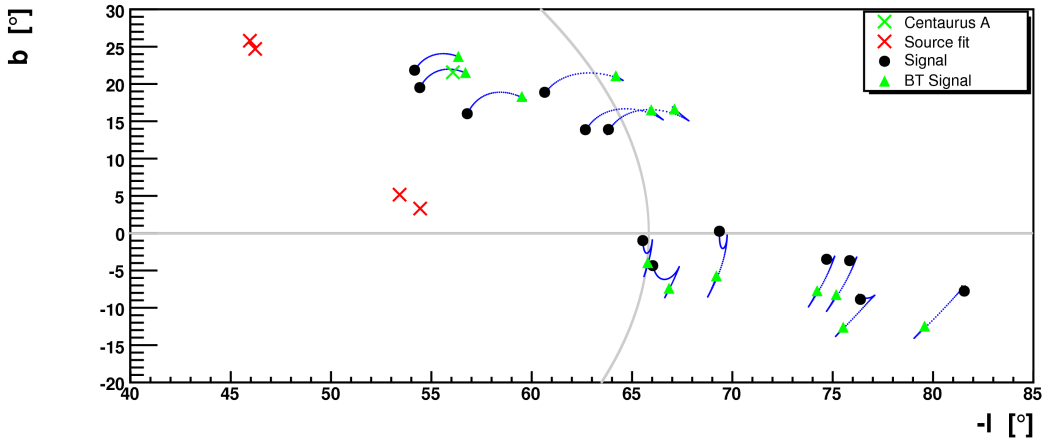

Figure 5.16: Thread-like multiplets obtained by $E_{\min} = 30\,\mathrm{EeV}$ and $d_{\max} = \langle d \rangle$. Multiplicity is equal or larger than 5. The sources obtained by linear fits (source fit) are denoted by the red crosses. TT BSS-A model is used. The blue dots indicate the evolution of the velocity vector. The green cross shows the position of Centaurus A.

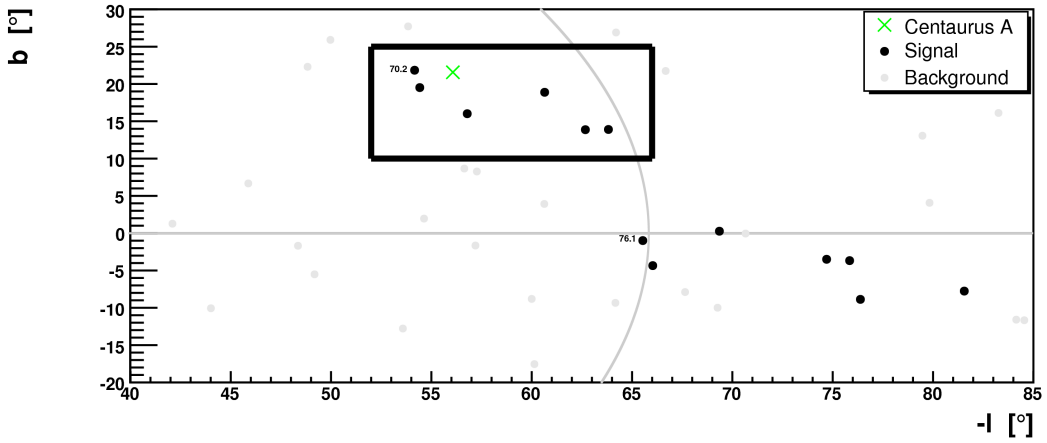

Figure 5.17: Thread-like multiplets obtained by $E_{\min} = 30\,\mathrm{EeV}$ and $d_{\max} = \langle d \rangle$. Multiplicity is equal or larger than 5. The numbers indicate the energies of the highest energy events in the multiplets. The green cross shows the position of Centaurus A. The black rectangle indicates group A that is backtracked in this section.

Group	$\langle D \rangle$
A	568.9
B	124.5
C	125.9
D	249.2

Table 5.1: The average deflection power $\langle D \rangle$ in units of [° EeV]. $\langle D \rangle$ is calculated by taking the average of the deflection powers of the threads in the groups.

age deflection power for each group is shown in table 5.1.

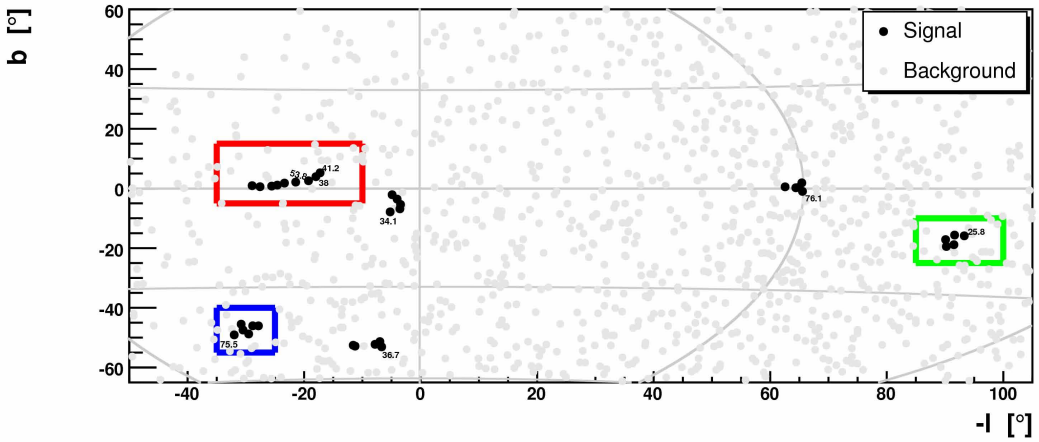

Figure 5.18: Thread-like multiplets obtained by $E_{\min} = 15\,\text{EeV}$ and $d_{\max} = 0.8\,\langle d \rangle$. The rectangles indicate the groups that are backtracked in this section. Group B (blue), group C (green) and group D (red).

5.4.1 Spread of the backtracked groups

Here it is assumed that the MST procedure is correct, i.e. the threads are created due to magnetic deflections. If a GMF model is accurate then the backtracked positions of the signal events in the groups should focus into the source position(s). As shown in section 5.3.1 and 5.3.2 the HMR ASS-A, HMR BSS-S, and TT BSS-A models produce different and contradictory results due to the different field configurations. For example in figure 5.10 (HMR ASS-A model) and 5.11 (HMR BSS-S model) the backtracked positions in group B fail to converge at the source positions while in figure 5.12 (TT BSS-A model) this procedure succeeds.

In the following the models are tuned so that the backtracked positions of the groups, hopefully, converge into the source positions obtained by fitting the threads in the groups. The groups are thus used to adjust or "correct" the models for their strength.

In reference [109] the periodicity of the Stanev model was varied in order to produce tracked trajectories of a correlated octuplet that converged into a single point. Here the field strengths, given by the GMF models, are varied by a factor f. This is expressed as,

$$B_f = f\, B_{\text{GMF}}, \tag{5.1}$$

where B_{GMF} is the field strength given by the GMF models. The goal is to find a field strength B_f, given by factor f, that produces backtracked event positions that are maximally focused into a source position. As an illustration, the events in group A are backtracked in different modified versions of the HMR ASS-A model in figure 5.19.

The field strength of the HMR ASS-A model is modified with factor f in the range [-10, 10]. Blue and red dots denote backtracked positions in the different modifications of the model.

A blue backtracked position is obtained by using a modification of the HMR ASS-A model that is produced by a positive factor f. Conversely, a red backtracked position is obtained by using a modification of the HMR ASS-A model that is produced by a negative factor f.

Note that the position of Centaurus A and the sources obtained by linear fits are obscured by the backtracked positions. Group A is denoted with the black dots and located in the middle where the backtracked positions for positive and negative factors meet.

Figure 5.20 is an enlargement of figure 5.19. Some of the backtracked event positions focus for positive values of f, at the source positions. In order to quantify how well this focusing is, the spread of the backtracked group is calculated.

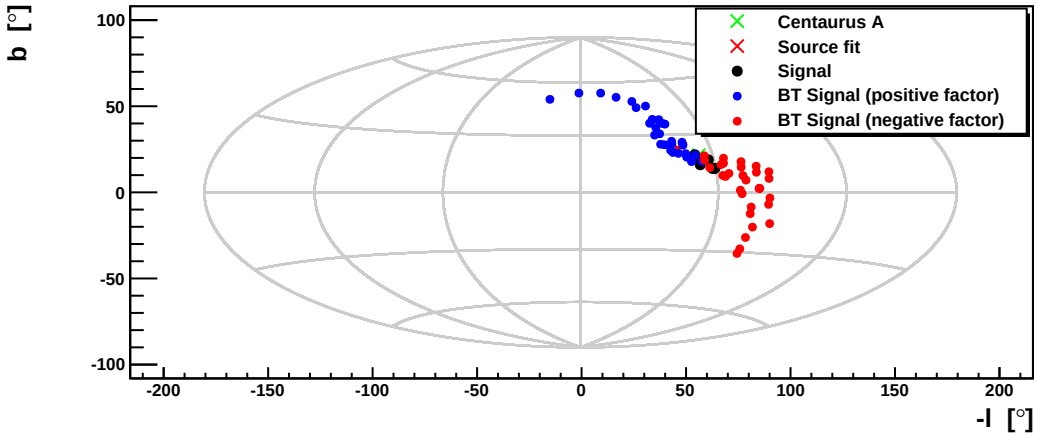

Figure 5.19: The events from group A backtracked in different modifications of the HMR ASS-A model. The field strength is modified by factors f in the range [-10, 10]. A blue backtracked position is obtained by using a modification of the HMR ASS-A model that is produced by a positive factor f. A red backtracked position is obtained by using a modification of the HMR ASS-A model that is produced by a negative factor f. The sources obtained by linear fits to the threads of group A are denoted by the red crosses. The (obscured) green cross shows the position of Centaurus A.

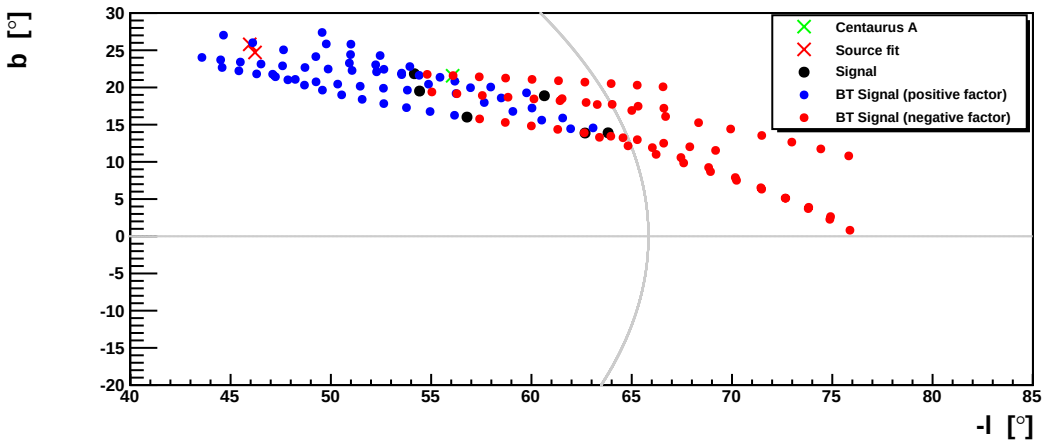

Figure 5.20: The events from group A backtracked in different modifications of the HMR ASS-A model. The field strength is modified by factors f in the range [-3, 3]. A blue backtracked position is obtained by using a modification of the HMR ASS-A model that is produced by a positive factor f. A red backtracked position is obtained by using a modification of the HMR ASS-A model that is produced by a negative factor f. The sources obtained by linear fits to the threads of group A are denoted by the red crosses. The (obscured) green cross shows the position of Centaurus A.

The *spread* of the backtracked group defined as,

$$\sigma = \sqrt{\frac{1}{N-1}\sum_i |\vec{n}_{\text{cms}} - \hat{n}_i|^2}, \tag{5.2}$$

where $\hat{n}_i$ are the backtracked positions of each event in a given group and the average direction

$\vec{n}_{\text{cms}}$ is given by,

$$\vec{n}_{\text{cms}} = \frac{\sum_i \hat{n}_i}{N}. \tag{5.3}$$

Zero spread means that all the backtracked events converge into a common *point* while large values of (5.2) indicate high degree of dispersion of the backtracked group. In addition, the spread of the backtracked groups is also calculated with respect to the source positions obtained by fitting.

The equations (5.2) and (5.3) are rewritten as,

$$\sigma_{\text{sou}} = \sqrt{\frac{1}{N}\sum_i |\vec{n}_{\text{sou}} - \hat{n}_i|^2}, \tag{5.4}$$

where $\hat{n}_i$ are still the backtracked positions of each event in a given group and $\vec{n}_{\text{sou}}$ is defined as

$$\vec{n}_{\text{sou}} = \frac{\sum_j \hat{n}_j}{N}, \tag{5.5}$$

where j runs over all source directions. $\vec{n}_{\text{sou}}$ is thus the barycenter of the sources. σ_{sou} is the spread of the backtracked events with respect to the barycenter of the sources.

The barycenter of the sources might be interpreted as the source position of the *group*. Thus, when σ_{sou} is zero, all the backtracked events converge into the "source position" as given by the threads.

Figure 5.21 shows the spreads obtained for different groups by varying the field strengths of different models. The left plots show the spreads for the factor range [-20, 20] while the right plots spotlight the region where the global and local spread minima are found. Table 5.2 shows the factors f yielding the minimum spread, as defined in equation (5.2), for different models. Table 5.3 shows the corresponding minimum spreads for the modified versions of the models. Table 5.4 shows the factors f yielding the minimum spreads between the source barycenter and the backtracked events. Table 5.5 shows the corresponding minimum spread σ_{sou}.

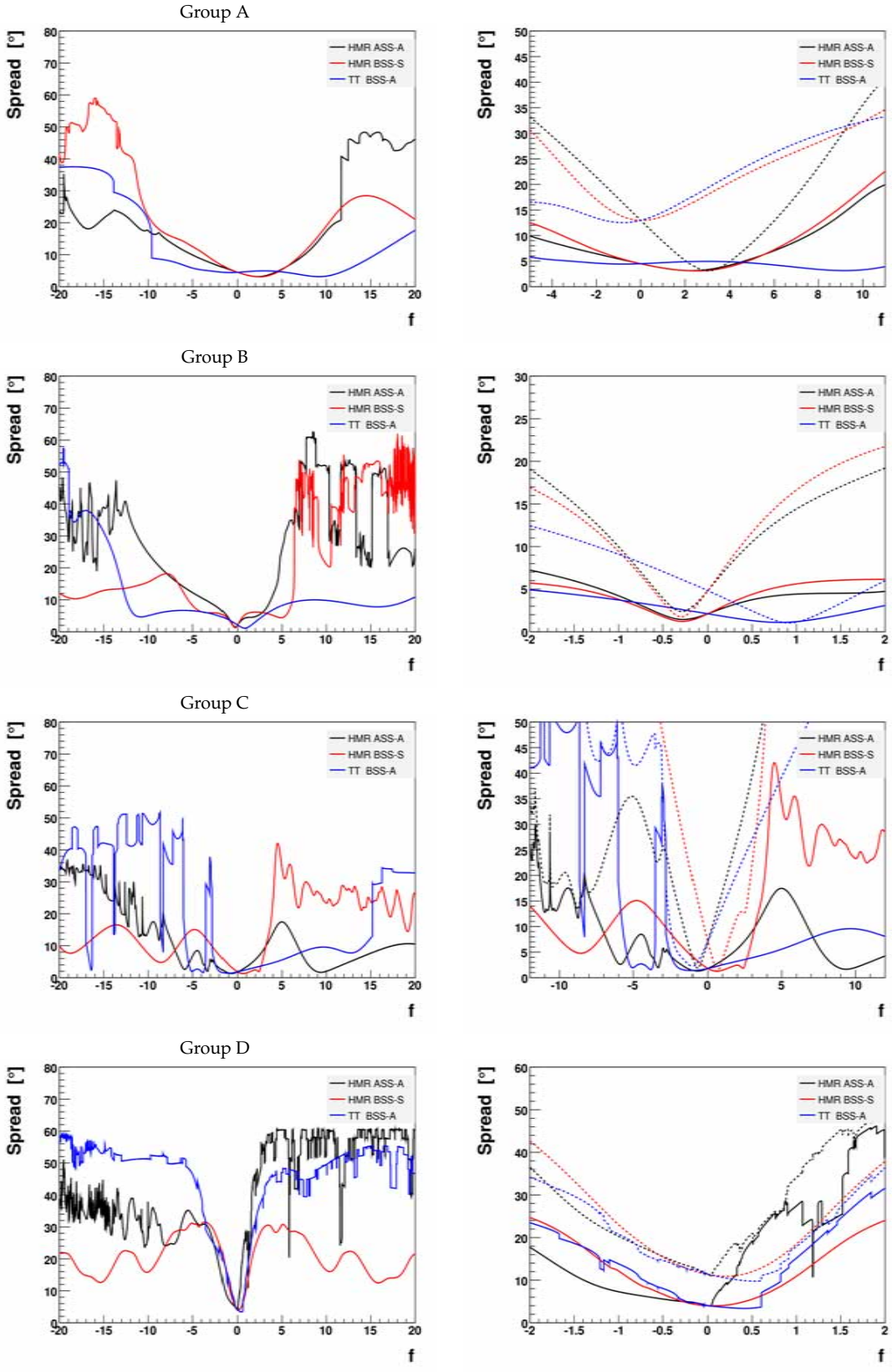

Figure 5.21: Left panel: The spread in equation (5.2) is calculated for the groups backtracked in different modifications of the models, given by factor f. The factors used are in the range [-20, 20]. Right panel: The regions where the minimum spreads are found. The dotted lines yield the spread of the backtracked events with respect to the source barycenter, as expressed in equation 5.4. The colour of the dotted lines indicate the model used.

Model	Group A	Group B	Group C	Group D
HMR ASS-A	2.3	-0.3	-0.7	0.0
HMR BSS-S	2.5	-0.3	0.6	0.1
TT BSS-A	9.0	0.8	-1.1	0.4

Table 5.2: Factors f in equation (5.1) yielding minimum spread as defined in equation (5.2).

Model	Group A	Group B	Group C	Group D
HMR ASS-A	3.2°	1.4°	1.3°	3.9°
HMR BSS-S	3.1°	1.2°	1.3°	4.0°
TT BSS-A	3.2°	1.1°	1.4°	3.3°

Table 5.3: The spreads given by the minimum factors in table 5.2. The spread is calculated with equation (5.2).

Model	Group A	Group B	Group C	Group D
HMR ASS-A	3.0	-0.3	-0.7	0.0
HMR BSS-S	0.1	-0.3	0.7	0.2
TT BSS-A	-0.8	0.8	-1.0	0.5

Table 5.4: Factors f in equation (5.1) yielding minimum spread as defined in equation (5.4).

Model	Group A	Group B	Group C	Group D
HMR ASS-A	3.1°	2.4°	1.9°	11.0°
HMR BSS-S	13.0°	1.7°	1.2°	10.9°
TT BSS-A	12.5°	1.0°	2.3°	9.8°

Table 5.5: The minimum spread given by the minimum factors in table 5.4. The spread is calculated with equation (5.4).

In order to compare the differences in spread before and after modification of the models, the groups are examined more closely.

As shown in table 5.2 the backtracked positions of the events in group A have a minimum spread when the field strengths of the HMR ASS-A, HMR BSS-S and TT-BSS-A models are modified by a factor 2.3, 2.5, and 9, respectively. The corresponding minimum spreads, σ, have the values 3.2°, 3.1°, and 3.2°, respectively (see table 5.3). Figure 5.22 shows group A backtracked in the HMR ASS-A model when its field strength is modified by a factor 2.3, yielding a minimum spread of the backtracked events.

Naturally, the backtracked events of group A in figure 5.22 are more focused compared to backtracked events of the same group in figure 5.14 where the original HMR ASS-A model is used. But the backtracked events in the modified model HMR ASS-A model are also closer to the sources than in figure 5.14.

However, the spread produced by the original HMR ASS-A model for group A, i.e. when $f = 1$, is 3.7° while the spread produced in the modified model is 3.2°. The difference in spread when the original HMR ASS-A model is used and when its field strength is a factor $f = 2.3$ stronger, is thus minimal.

In comparison, a minimum spread of only 1.4° is produced when group B is backtracked in the HMR ASS-A model that is modified with a factor $f = -0.3$. For $f = 1$ the spread is 4.0°, that is a 2.6° difference. The backtracked positions of the events in group B are shown in figure 5.23 where the field strength of the HMR ASS-A model is modified by a factor $f = -0.3$.

The negative sign of the minimum factor also ensures that the group B is backtracked towards the sources rather than away from them as in figure 5.10 where the original HMR ASS-A model is used.

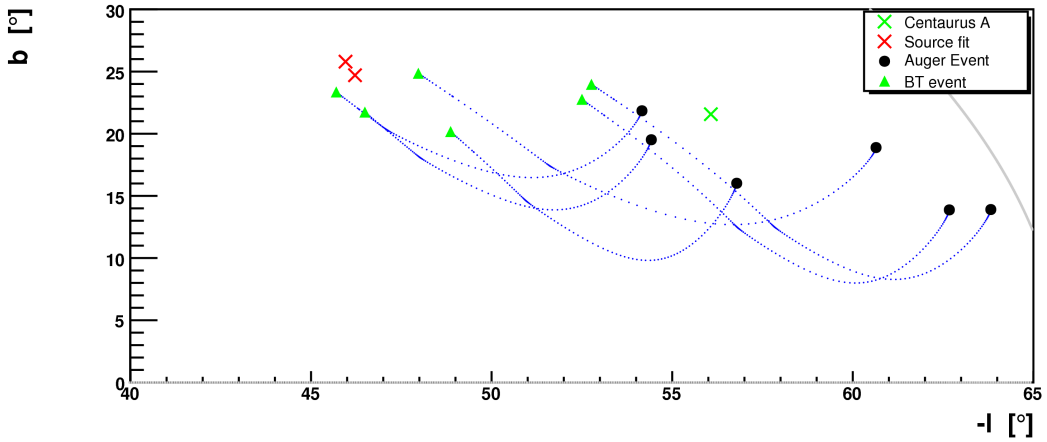

Figure 5.22: The events from group A backtracked in the modified HMR ASS-A model. The field strength is modified by a factor $f = 2.3$. Blue dots show the evolution of the velocity vector.

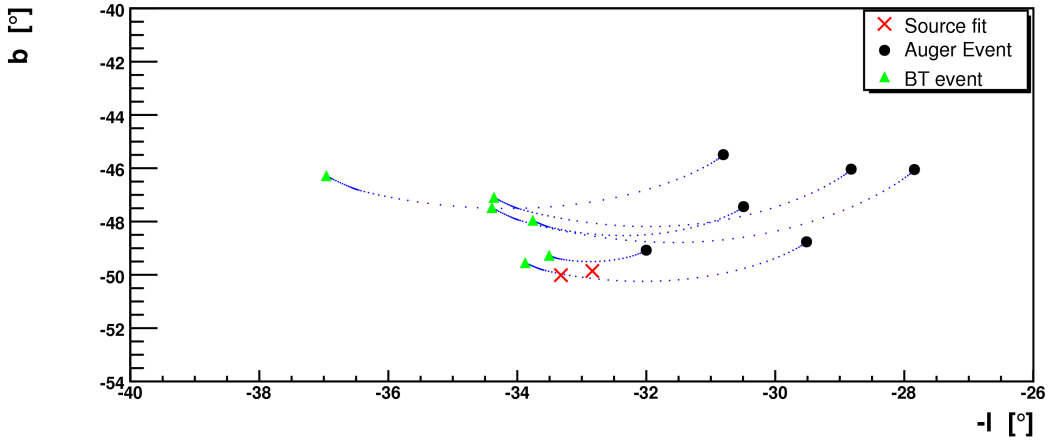

Figure 5.23: The events from group B backtracked in the modified HMR ASS-A model. The field strength is modified with a factor $f = -0.3$. Blue dots show the evolution of the velocity vector.

Group D is distinct from the others due to the low minimum factors in table 5.2. Here the factors are zero or close to zero. Hence, none of the models are able to focus this group, and the minimum spread is just the spread of the original Auger events.

The right panel in figure 5.21 shows the relation between the spreads as defined in equations 5.2 and 5.4.

For group A the minimum spreads are $\sigma = 3.2°$ and $\sigma_{\text{sou}} = 3.1°$. These are obtained by backtracking the group events in the HMR ASS-A model that is modified by a factor 2.3 and 3.0, respectively. However, the field strengths produced by the factors 2.3 and 3.0 are similar. Thus, the barycenter of group A backtracked is equal to the barycenter of the sources. This indicates that group A has a common source if the modified HMR ASS-A model is correct. This agreement does not exist when group A is backtracked for the modified HMR BSS-S and TT BSS-A models (see tables 5.3 and 5.5).

For group B the agreements are even better. The minima are in agreement with each other in figure 5.21. This is also true for group C. The factors in table 5.2 and 5.4 for group B are identical. This is again also true for group C. In addition, the factors have very low values, varying from

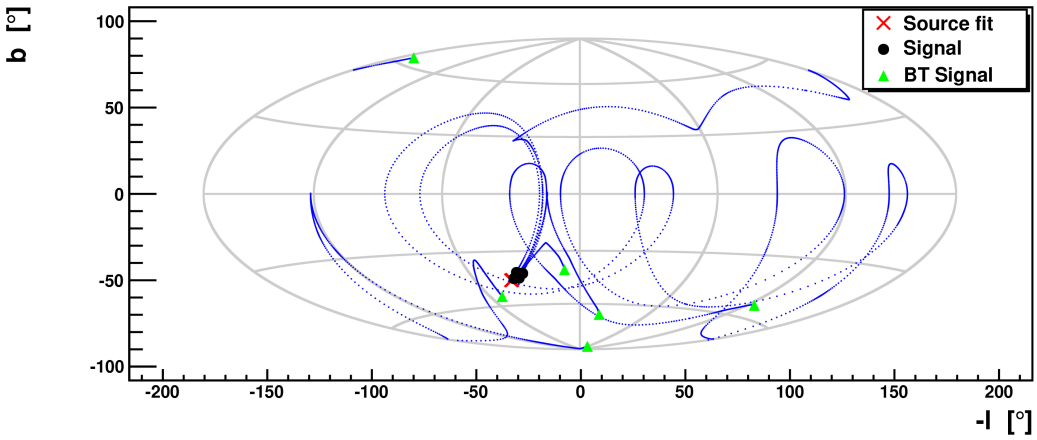

Figure 5.24: The backtracked events from group B given by the field strength of HMR ASS-A model with factor $f = 9$. Blue dots show the velocities of the group events.

-1.1 to 0.8. For group D the spread of the backtracked events with respect to the sources is not reliable. Group D, consisting of the nine string-like Auger events, produces 44 sources scattered along a part of the galactic disk. The source position of group D is thus most likely randomly located.

5.5 Conclusion

In table 5.2 all the minimum factors are in the range [0.1, 2.5] except for the minimizing factor of 9 for group A backtracked in the TT BSS-A model. Hence, in order to obtain maximum focusing of the groups, the original field strengths of the models need not to be substantially changed. But precisely because of this proximity of the minimum yielding factors to $f = 1$, the reduction of the spread is not large. From the models, the field in the vicinity of the Earth is approximately in the range from 1.4 μG to 2 μG. Apparently, these values seem small even when multiplying them with a factor of 2.5 or even 9. However, as seen in figure 5.21, even though $f = 9$ yields minimal spread for group A when the TT BSS-A model is used, a factor $f = 9$ yields a much larger spread for the same group when HMR ASS-A model is used. More strikingly, backtracking group B in the HMR ASS-A model with factor $f = 9$ yields almost a maximum spread. This is demonstrated in figure 5.24.

In figure 5.24 backtracked events are scattered in an extreme way. A factor $f = 9$ thus produces not only a minimum spread for group A when the TT model is used, but also a maximum spread for group B when the HMR ASS-A model is used. In both cases, however, the field in the vicinity of the Earth is almost the same.

Another striking feature is that all the values in table 5.2, except for group D, yield backtracked directions that converge towards the sources. For example, in figure 5.10 (HMR ASS-A model) group B is tracking away from the sources. The tuning gave a minimizing factor of $f = -0.3$. The negative sign implies field reversal. By multiplying the original field strength with $f = -0.3$ group B is backtracked towards the sources, as seen in figure 5.23.

For the TT-model in figure 5.12 the direction of propagation is correct, and this direction is kept after tuning since the minimizing factor is positive. The minimizing factors for group C tell the same story. In figure 5.10 (HMR ASS-A model) group C is backtracked away from the sources. The tuning yielded a negative factor, $f = -0.7$. When the field strength is multiplied by this factor the group is backtracked towards the sources. In figure 5.11 the propagation is correct and the tuning gives a positive factor, keeping the field direction invariant.

For group A all the backtracked directions are towards the sources and thus the minimizing factors are also positive. In addition, the minimum factors in tables 5.2 and 5.4 are approximately equal for group B and C, respectively. Tables 5.3 and 5.5 also show that the minimum spreads with respect to the barycenter of the backtracked group B are approximately equal to the minimum spreads with respect to the source barycenter of group B. Similar results are produced for group C. In addition, the minima are found in modified models that are produced with similar factors f, as seen in figure 5.21. This implies that the source position of group B and C is given by $\vec{n}_{\text{sou}}$ in equation 5.5, if the modified models are correct. Similar results are also found for group A when the HMR ASS-A model is used.

5.6 Simulations

5.6.1 Introduction

Finding thread-like structures in data with the MST procedure does not prove that these structures are solely a result of magnetic bending of particles originating from a common source. They might be a result of chance or coincidence. In the sections above several cuts on Auger energy and minimal branch lengths of the MST were analyzed. Each of them yields different number of clusters containing the arrival directions of Auger events. Arrival directions combine with each other and threads are constituted.

In order to establish whether the threads found for a given set of cuts are genuine or not, a large number of uniform arrival directions over the sky (isotropic) are generated with the same energy cut E_{min} as used for Auger data. The cosmic-ray energy spectrum approximately follows a power law. Here, the energies are thus generated according to a power law. These isotropically generated arrival directions are denoted as background.

PAO is located in Argentina in the southern hemisphere. Part of the sky is thus unavailable for cosmic ray detection. The relative exposure to arrival directions are given by a probability function ω (see equation (D.1)).

The isotropic arrival directions are thus generated in accordance to both the relative exposure of PAO and the energy spectrum (see appendix D) for details.

The MST procedure is applied to each simulated background, and fake threads from the background are obtained. All fake threads in the simulations that share one or more events are considered here as a single group. Accordingly, all threads in Auger data that share one or more Auger events are considered as a single group originating from a common source. Thus, as in the sections above, each group might contain several threads. The correlation coefficients measuring the elongation of the fake threads in the groups from the simulations are compared with the coefficients found in the threads in the data groups.

Harari, Mollerach, and Roulet [109] found in Auger data from January 2004 to October 2006 an octuplet with the chance probability of $8 \cdot 10^{-4}$. The correlation coefficient of the octuplet was found to be $C_{\text{octuplet}} = 0.977$. The chance probability was calculated by taking the fraction of all octuplets from the simulations with correlation coefficients higher or equal to C_{octuplet}, and the total number of simulations.

5.6.2 Cuts

Cuts used for the simulations are the same as in section 5.3.2, i.e. the cuts that yield the four quintuplets near Centaurus A in figure 5.17 namely,

- $E_{\text{min}} = 30\,\text{EeV}$.
- $d_{\text{max}} = \langle d \rangle$.
- $N_{\text{multiplicity}} \geq 5$

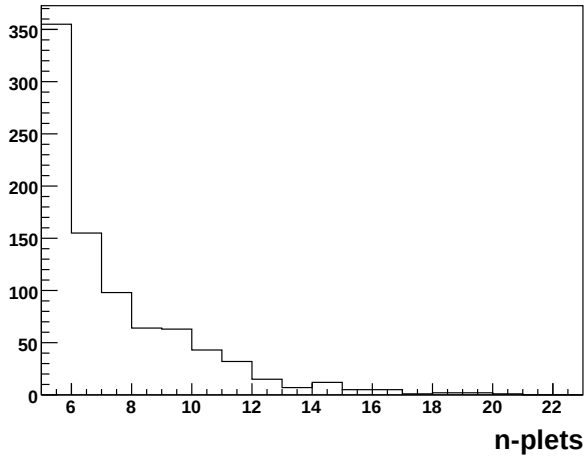

Figure 5.25: The frequency of groups of different sizes, denoted as n-plets, appearing at least once in the simulations.

An additional cut is imposed on the MST procedure in order to save time. After the tree is cut, as described in Appendix C, clusters of different number of events are formed. In order to find thread-like multiplets the events are combined in different ways with each other causing a combinatorial explosion for large clusters. Here clusters larger than twenty events are cut so that new clusters with fewer events than twenty are formed. This might cause loss of information. However, the number of clusters containing more than twenty events are negligible and thus this cut has minimal impact on the results. The cuts yield 349 events in data that sequently form the four quintuplets in figure 5.7. Thus, 349 background events are simulated 10 000 times.

The four quintuplets in figure 5.17 are considered to be part of two groups. Group A has already been defined and consists of six events above the galactic disk. The second group, group E, has seven events that are below the disk.

5.6.3 Size of the groups

As mentioned earlier, in the data the cuts yield two groups of 6 and 7 events each. Figure 5.25 shows the frequency of groups of different sizes appearing in the simulations. Groups of six and seven background events appear at least one time in around 150 and 100 simulations, respectively. This corresponds to 1.5 and 1% of the total simulation, respectively. Thus, the actual sizes of the groups found in data are not significant.

5.6.4 Correlation coefficients

In data, two groups in figure 5.7 contain two quintuplets each. The threads in group E have the correlation coefficients of 0.956 and 0.967. For group A the numbers are 0.974 and 0.980. Thus, the maximal correlation coefficient found in group A and E is 0.980 and 0.967, respectively. Figure 5.26 shows the distribution of maximal correlation coefficients of the threads from the simulated backgrounds, regardless of their size, inside the groups simulated. The maximal coefficients found in the data groups A and E are marked with blue and red arrows, respectively. The total number of coefficients is 866. In the 10 000 simulated backgrounds thus only 866 groups of threads are found.

A total of 344 threads (3.4%) have coefficients equal or larger than the maximal coefficient found in group A. The number for group E is 592 (5.9%).

Figure 5.27 compares the average coefficients found in group A and E to the averages found in the simulated groups. Now 130 groups or only 1.3% have an average equal or higher than

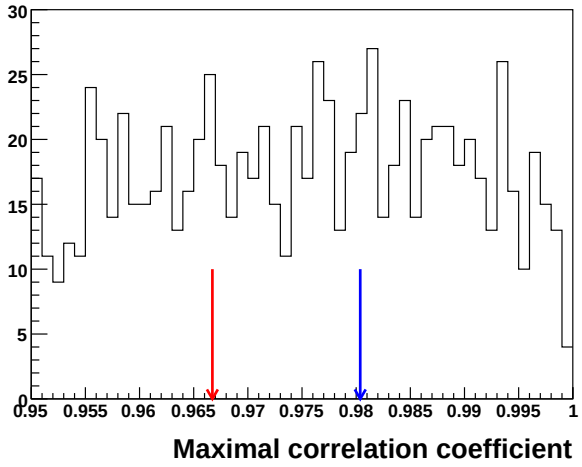

Figure 5.26: Maximal correlation coefficients of the threads inside the simulated groups compared to maximal coefficients found in the data group A (blue) and E (red). Note that the simulations containing groups with no threads are not shown.

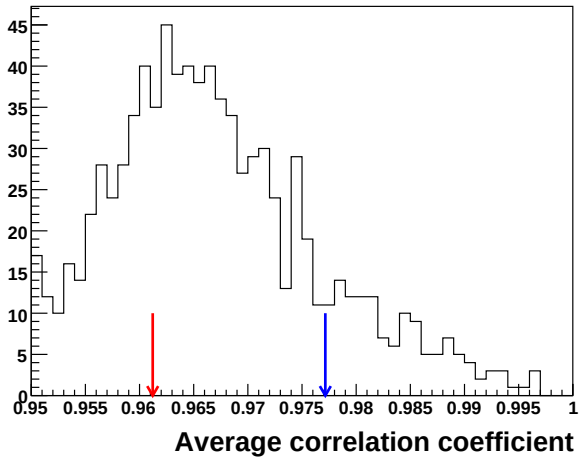

Figure 5.27: Average correlation coefficients found in the simulated groups compared to average correlation coefficients found in group A (blue) and E (red). Note that the simulations containing groups with no threads are not shown.

group A. The number for group E is 615 6.2%.

5.7 Conclusion

From the limited simulations conducted in this study the signal in the Centaurus A region is most likely just a fluctuation. However, more extensive simulations of changing fractions of mock signals and background are needed before any definitive conclusions can be drawn.

Chapter 6

Conclusion and Outlook

In this study the consequences of the galactic magnetic field on the propagation of UHECR is investigated in detail for different areas of research. The GMF models are studied and compared to each other. The deflections and the extra-galactic exposure is established for the different models.

The deflections of protons originating from the galactic center are calculated via constructing a shooting procedure. The shooting procedure is a powerful tool that establishes the arrival directions of cosmic rays of different energies originating exactly from the galactic center.

A shooting procedure is also constructed for the study of deflections of cosmic rays originating from AGNs. For different models the AGN images are compared to Auger data, and the UHECR–AGN correlation found by the Pierre Auger collaboration [98, 99] is recalculated after correcting the Auger events for deflections.

Thread-like multiplets are obtained via the MST method on Auger data. The multiplets obtained with different cuts are studied.

Galactic Magnetic Field models

Although the local magnetic field strength is similar in all models their different symmetries, with regards to the field directions in the spiral arms and at the galactic disk, have a huge impact on the propagation of the UHECRs. It is shown that for observers at Earth, the extra-galactic exposure has relatively large blind regions even for 100 EeV protons originating from sources in these regions, if configurations with field reversal at the disk are assumed.

The deflections for protons with energies of 10 EeV and larger are proportional to $\sim 1/E$ which makes cosmic ray astronomy possible if the models are accurate.

Galactic Center

It is shown that 10 EeV protons are deflected 15° and 25° in the HMR BSS-S and HMR ASS-A models, respectively. As the cosmic ray excesses from the galactic center are reported for energies in the range of 1 EeV this indicates that the cosmic rays from this region might be neutral particles, like neutrons. However, due to field reversals at disk crossing the HMR ASS-A model produces a channel near the galactic disk where the field is negligible or zero. If the GMF indeed changes sign at the galactic disk then even charged particles with the lowest energies might reach Earth.

It is also shown that the magnetic field, as predicted by the models, has a dominating y-component. This allows for rewriting and simplifying the equations of motion. There are no disagreements between deflections produced by ordinary and simplified equations of motion for protons with energies larger than 5 EeV.

Active Galactic Nuclei

It is established that the protons originating exactly from the original AGNs in references

[98, 99] have an average deflection of around 3° which is comparable to the size of the correlation circles $\Psi = 3.2^\circ$ found by the Pierre Auger collaboration. However, the AGN images as predicted by the models match the directions of the Auger data very poorly. In addition, by backtracking the Auger events in different models, only 11 to 15 Auger events remain inside the limit of $\Psi = 3.2^\circ$ around their correlating AGNs.

After correcting Auger data for magnetic deflections the UHECR-AGN correlation is recalculated. It turns out that the correlation found, for all models, is weaker than the original correlation in [98, 99]. This indicates that either the models are inaccurate (even for energies above 57 EeV) or the Auger data correlates to other astronomical objects than AGNs.

Thread-like Multiplets

Groups of thread-like multiplets are found in data by using the MST procedure. Interesting groups are handpicked and corrected for deflections in different models in order to check if the backtracked groups focused towards the sources. Overall contradictory results are obtained due to the complexity of the models. Backtracked groups focusing in one model are spread apart in other models.

A group of thread-like multiplets is found in the Centaurus A region. Simulations are used to verify if this group is genuine or not. The conclusion based on the simulations is inconclusive. Additional and more extensive simulations are needed in order to clarify the matter.

Outlook

The GMF is poorly understood due to some weaknesses in the observational methods and insufficient amount of rotation and synchrotron measurements. In the near future the construction of the Low Frequency Array (LOFAR) [60] and Square Kilometre Array (SKA) [60, 113] telescopes would greatly improve the amount of rotation and synchrotron measurements. With the SKA telescope it would be possible to measure 20 000 rotation measures from pulsars in the galaxy, yielding a full description of the regular galactic magnetic field component [113]. The LOFAR telescope will provide complementary information by measuring very weak rotation measures down to 5.7° [60]. In addition, LOFAR and SKA will have capabilities to measure synchrotron emission [60].

With the LOFAR and SKA telescopes a radically improved understanding of the GMF is indeed possible. As a result we will be one step closer to charged particle astronomy. In addition, the PAO can also improve the understanding of the GMF by, for example, searching for thread-like multiplets. The shooting procedures developed in this thesis can be applied to establish the arrival directions of cosmic rays originating from different varieties of sources, from the GC to AGNs, under different GMF configurations. If the GC excess found by reference [93] and the AGN–UHECR correlation found by the PAO is real, then it might be possible to infer the correct strength and the correct configuration of the GMF by comparing the arrival directions of Auger data and the arrival directions given by the shooting procedures.

Appendix A

The Lorentz force

The generalized Newton's Second Law [114, 115] is given by

$$\frac{\mathrm{d}P^{\mu}}{\mathrm{d}t} = q\,F^{\mu}{}_{\nu}v^{\nu}, \tag{A.1}$$

where m is the mass of the particle, v^{ν} is the four-velocity, and P^{μ} is the four-momentum. $F^{\mu}{}_{\nu}$ is the electromagnetic tensor [114],

$$F^{\mu}{}_{\nu} = \begin{bmatrix} 0 & E_x & E_y & E_z \\ E_x & 0 & B_z & -B_y \\ E_y & -B_z & 0 & B_x \\ E_z & B_y & -B_x & 0 \end{bmatrix} \tag{A.2}$$

The Lorentz force is derived by writing equation (A.1) in vector form. Right hand side of equation (A.1) yields

$$q\,F^{\mu}{}_{\nu}v^{\nu} = q\,F^{j}{}_{i}v^{i} = q\,\epsilon_{ijk}B_k v_i = q\,\vec{v}\times\vec{B}, \tag{A.3}$$

where ϵ_{ijk} is the Levi-Civita density [114, 116] given by

$$\epsilon_{ijk} = \begin{cases} 0 & \text{for } i=j,\ j=k, \text{ or } k=i, \\ +1 & \text{for } (i,\,j,\,k) \in \{(1,\,2,\,3)\,,\,(2,\,3,\,1)\,,\,(3,\,1,\,2)\}, \\ -1 & \text{for } (i,\,j,\,k) \in \{(1,\,3,\,2)\,,\,(3,\,2,\,1)\,,\,(2,\,1,\,3)\}. \end{cases} \tag{A.4}$$

Writing out the left hand side yields,

$$\frac{\mathrm{d}\vec{p}}{\mathrm{d}t} = \frac{\mathrm{d}}{\mathrm{d}t}\left(m\vec{v}\gamma\right) = m\gamma\frac{\mathrm{d}\vec{v}}{\mathrm{d}t} + m\vec{v}\cdot\frac{\mathrm{d}\vec{v}}{\mathrm{d}t}\gamma^3/c^2, \tag{A.5}$$

where $\gamma = (1-\vec{v}^2/c^2)^{-1/2}$. For the energy of a relativistic particle with mass m, momentum $\vec{p}$ and energy E the following relation holds,

$$E^2 = \vec{p}^{\,2}c^2 + m^2c^4. \tag{A.6}$$

Isolating $\vec{p}^{\,2}$ and deriving with respect to time yields,

$$\frac{\mathrm{d}}{\mathrm{d}t}\left(\vec{p}^{\,2}\right) = 2\vec{p}\cdot\frac{\mathrm{d}\vec{p}}{\mathrm{d}t} = 0. \tag{A.7}$$

Equation (A.7) yields,

$$\gamma\vec{v}\frac{\mathrm{d}\vec{v}}{\mathrm{d}t} + v^2\frac{\mathrm{d}\gamma}{\mathrm{d}t} = 0. \tag{A.8}$$

Since $\mathrm{d}\gamma/\mathrm{d}t = -\vec{v}\cdot(\mathrm{d}\vec{v}/\mathrm{d}t)\gamma^3/c^2$, equation (A.8) is rewritten as,

$$\vec{v}\cdot\frac{\mathrm{d}\vec{v}}{\mathrm{d}t}\left(\gamma - v^2\gamma^3/c^2\right) = 0. \tag{A.9}$$

Equation (A.9) yields $\vec{v}\cdot(\mathrm{d}\vec{v}/\mathrm{d}t) = 0$. With this relation equation (A.5) is reduced to,

$$\frac{\mathrm{d}\vec{p}}{\mathrm{d}t} = m\gamma\frac{\mathrm{d}\vec{v}}{\mathrm{d}t} \tag{A.10}$$

In the ultra-relativistic case ($E \gg mc^2$) equation (A.6) is reduced to $E \approx pc = m|\vec{v}|\gamma c$. The velocity is expressed as,

$$|\vec{v}| = \frac{E}{m\gamma c} \tag{A.11}$$

By using the relation $\vec{v}/|\vec{v}| = \hat{n}$ where $\hat{n}$ is the unit vector along the direction of flight and equation (A.11), equation (A.5) is now expressed as,

$$\frac{\mathrm{d}\vec{p}}{\mathrm{d}t} = \frac{E}{c}\frac{\mathrm{d}\hat{n}}{\mathrm{d}t}. \tag{A.12}$$

Writing the left hand side of equation (A.1) as equation (A.12), and the right hand side as equation (A.3) yields,

$$\frac{E}{c}\frac{\mathrm{d}\hat{n}}{\mathrm{d}t} = q\,\vec{v}\times\vec{B}, \tag{A.13}$$

For ultra-relativistic particles ($|\vec{v}| = c$) the velocity is given by

$$\vec{v} = c\hat{n}, \tag{A.14}$$

Equation (A.13) is now transformed to

$$\frac{\mathrm{d}\hat{n}}{\mathrm{d}t} = \frac{qc^2}{E}\left(\hat{n}\times\vec{B}\right). \tag{A.15}$$

By dividing equation (A.15) with a factor c yields

$$\frac{\mathrm{d}\hat{n}}{\mathrm{d}s} = \frac{qc}{E}\left(\hat{n}\times\vec{B}\right). \tag{A.16}$$

where $s = ct$ is the path length [49].

Appendix B

Magnetic Deflections and Active Galactic Nuclei

B.1 Magnetic deflection

The sky map in figure 4.6 in section 4.4 is divided into three regions given by red, blue and green rectangles in order to study more carefully the details about the AGN images as observed on Earth, the true positions of the AGNs, Auger events and backtracked Auger events.

Only figures showing the red region is used in section 4.6. The figures of blue and green regions are given here.

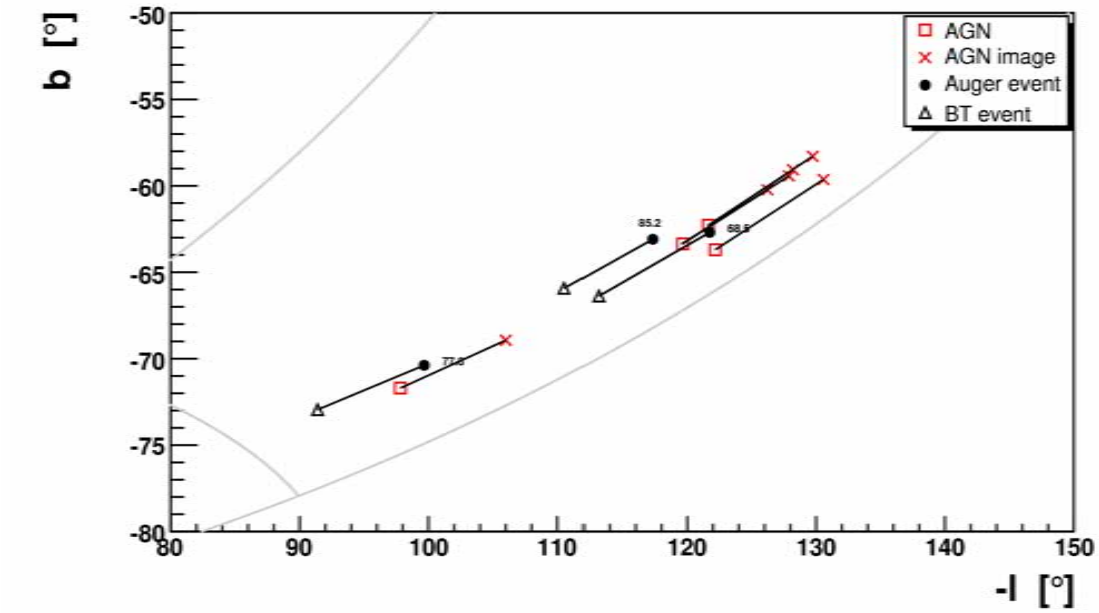

Figure B.1: The second rectangle with blue boundaries taken from figure 4.6. Here the HMR ASS-A model is used.

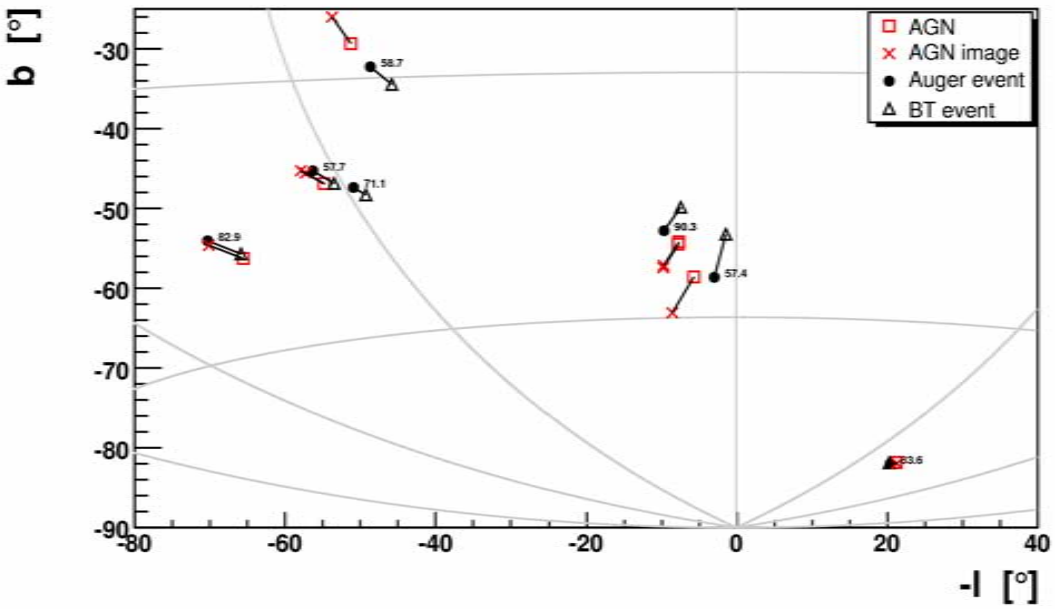

Figure B.2: The third rectangle with green boundaries taken from figure 4.6. Here the HMR ASS-A model is used.

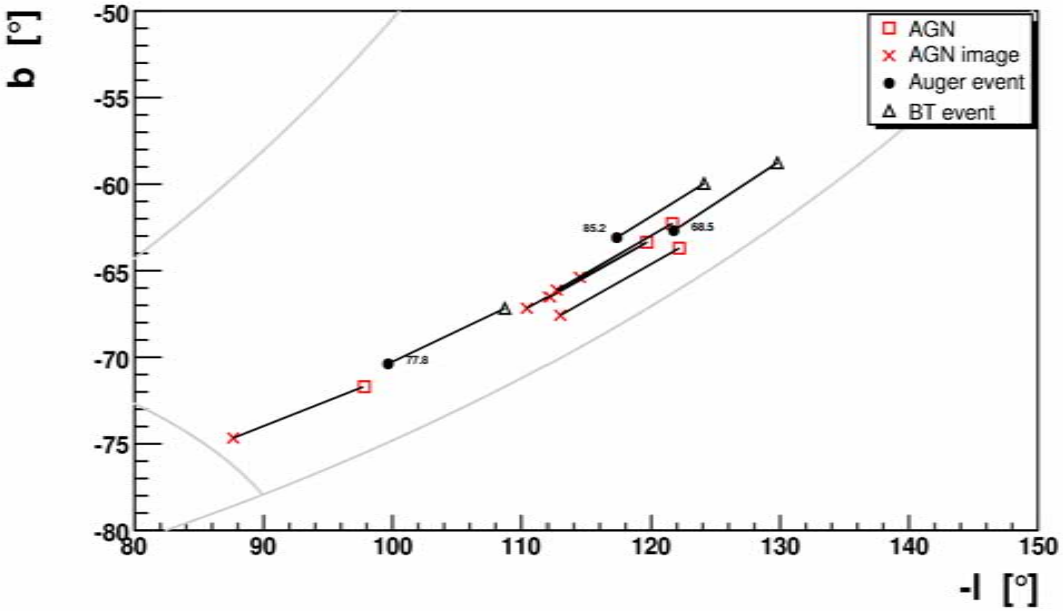

Figure B.3: The second rectangle with blue boundaries taken from figure 4.6. Here the HMR BSS-S model is used.

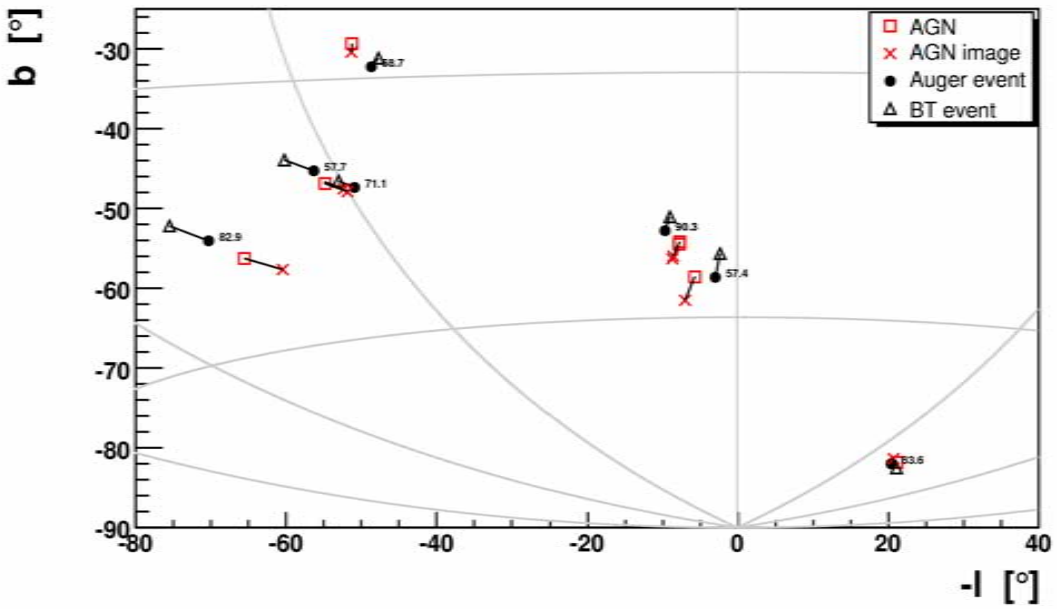

Figure B.4: The third rectangle with green boundaries taken from figure 4.6. Here the HMR BSS-S model is used.

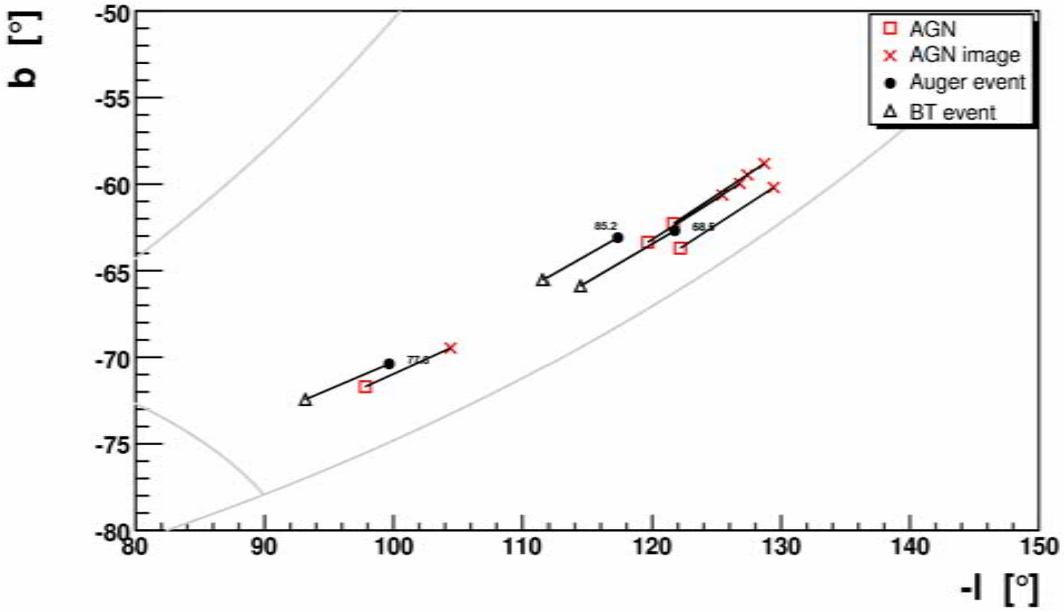

Figure B.5: The second rectangle with blue boundaries taken from figure 4.6. Here the TT BSS-A model is used.

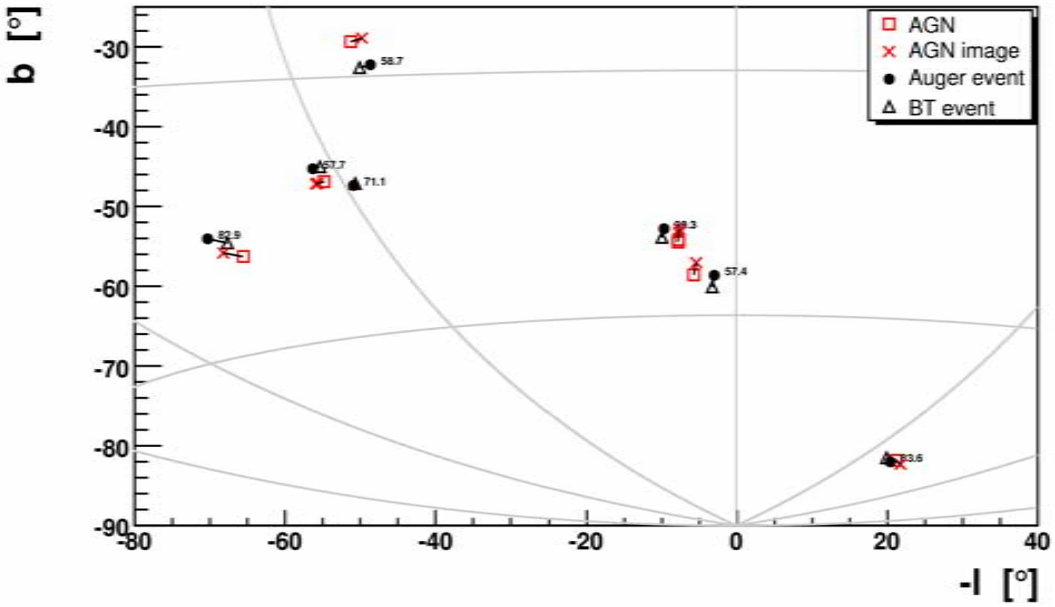

Figure B.6: The third rectangle with green boundaries taken from figure 4.6. Here the TT BSS-A model is used.

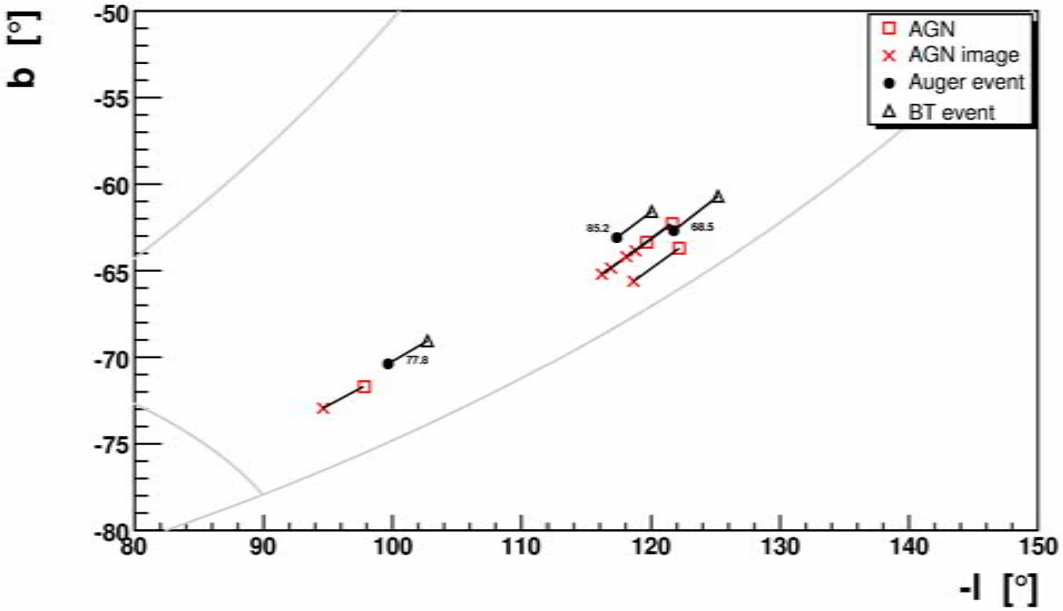

Figure B.7: The second rectangle with blue boundaries taken from figure 4.6. Here the KST BSS-A model is used.

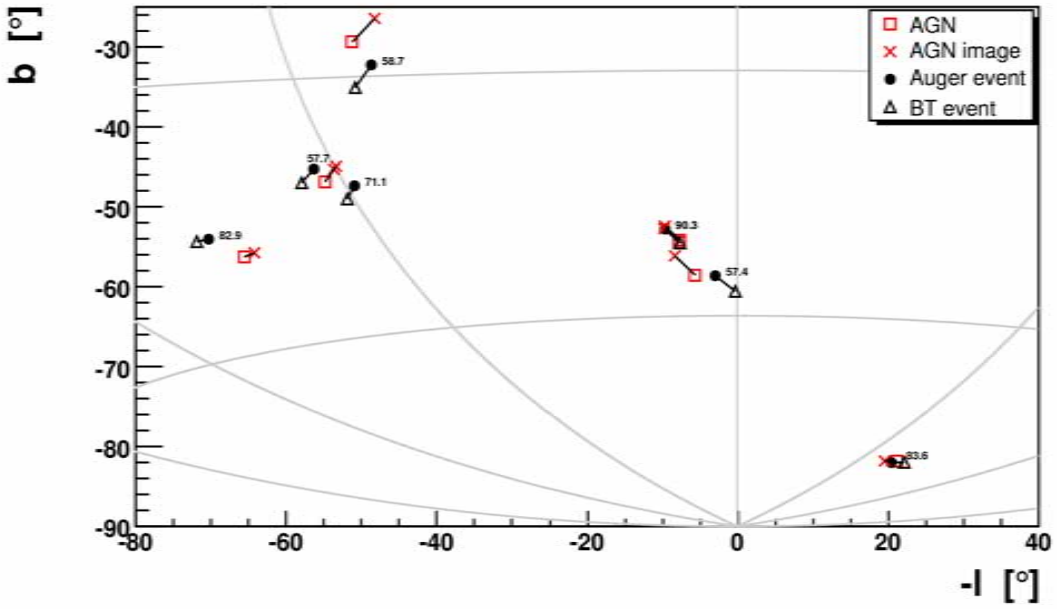

Figure B.8: The third rectangle with green boundaries taken from figure 4.6. Here the KST BSS-S model is used.

B.2 Search method

The method for establishing the correlation between the UHECR – AGNs is well described in the references [98, 99, 100, 102]. The main points of this method are explained in this appendix.

Concentrating on vertical showers only, the zenith angles have a maximum of 60°. This implies [100, 117] that the relative SD exposure is given by,

$$\omega(\delta) \propto \int_0^{2\pi} \cos(\theta(\delta, l, \alpha))\, \mathrm{d}\alpha. \tag{B.1}$$

Here $\cos(\theta(\delta, l, \alpha))$ is given by,

$$\cos(\theta(\delta, l, \alpha)) = \sin\delta \sin l + \cos\delta \cos l \cos\alpha, \tag{B.2}$$

where δ is the declination and α the right ascension. l is $-35.2°$, corresponding to the latitude of the Southern Observatory.

The first task is to establish the chance probability for an isotropic event being separated by a given angle from one or more AGNs. A large amount of arrival directions are simulated with the declination given by the $\cos\theta$ expression (B.2). The angular separation is calculated between these random simulated arrival directions and the AGNs from the Véron catalogue [101]. Angular separations in the range 1° to 8° are kept. For the purpose of calculating the chance probability an interval step of 0.1° is introduced, yielding 70 angular separation values, denoted by γ, in the range 1° to 8°. By integrating over the area of the sky spanned by circles of a given radius γ around the AGN the chance probability is obtained [100],

$$p = \frac{1}{N} \iint_A \omega(\delta)\, \mathrm{d}\delta\, \mathrm{d}\alpha, \tag{B.3}$$

where N is the total number of simulated events and A is the total area covered by the circles with a given radius γ.

Assuming that the Auger events are isotropic the probability that k or more out of n Auger events have an angular distance to an AGN less than a given γ is given by the binomial distribution,

$$P = \sum_{j=k}^{n} \binom{n}{j} p^j (1-p)^{n-j}, \tag{B.4}$$

where n is the total number of events and p is given by B.3. However, the binomial probability P given in equation (B.4) is not the real correlation probability from an isotropic distribution. It has to be penalized for the scanning procedure.

It is clear that the arrival directions of the n Auger events are only one of many sets of arrival directions possible if isotropy is assumed. Thus many sets of n generated events are simulated. The angular distance to the AGNs is recalculated. The probability in equation (B.4) is calculated for each simulated set. The correlation probability is then the fraction of the sets with values of P equal or less to the one obtained with the Auger data set.

Appendix C

Minimal Spanning Tree

The Minimal Spanning Tree (MST) is well known from graph theory and is described in abundance of literature [107]. The MST as applied to the arrival directions of cosmic rays is explained in detail in the references [108, 109, 110]. The main points of this method are explained here.

In this appendix, Auger data from the period January 2004 until the end of 2008 are used.

The points of arrival directions of the cosmic rays are connected in such a way so that the total length between the first chosen point and the last is minimal. This forms a tree like structure with no loops as seen in figure C.1. The red lines between the events constitute the branches of the tree. The structure of the tree is unique, i.e. for a given set of points there exists only one MST. The branch lengths are added up and an average is calculated. The tree is cut by setting a limit $d_{\max}$ on the branch length. The appropriate value of this limit, however, is not obvious and has to be determined manually, resulting in a somewhat arbitrary partition of the original MST. Figure C.2 shows the tree cut for two different values, $d_{\max} = 0.5\langle d\rangle$ and $d_{\max} = \langle d\rangle$, where $\langle d\rangle$ is the average length of the connections in MST.

In the upper panel ($d_{\max} = 0.5\langle d\rangle$) the majority of the clusters are doublets of Auger events. The lower panel is far richer in terms of large clusters. Applying larger cuts for $d_{\max}$ inevitably increases the number of large clusters. Figure C.3 shows the frequency of different lengths between the branches for two minimal spanning trees constructed with the energy cuts $E_{\min} = 15\,\mathrm{EeV}$ and $E_{\min} = 20\,\mathrm{EeV}$.

The frequency of low angular lengths are larger at 15 EeV cut due to the larger amount of data. This energy cut yields 1799 data events. The average length for this cut is 2.4°. Increasing this cut to 20 EeV increases the average length of the tree as seen in the lower panel. Now the number of data events is 956. To sum up, the clusters grow with lower cuts on the energy of the particles and with larger cuts on the branch lengths of the tree. In the search for threadlike structures evaluating the probability of finding such structures by chance is crucial. Large threadlike structures become a liability with respect to the computing time. In order to strike a balance between a sufficient number of potential structures and reasonable computing time suitable values for energy cut and $d_{\max}$ are adopted in chapter 5.

It was shown in equation (2.4) that the deflections the high energetic primaries undergo are proportional to $1/E$. In the high energetic range the relation between the arrival directions, $\theta_{\mathrm{arrival}}$, of the Auger events and the source position, θ_{source}, is approximated with

$$\theta_{\mathrm{arrival}} \approx \theta_{\mathrm{source}} + \frac{D}{E} \tag{C.1}$$

where D is the so-called deflection power in units of $[^\circ\mathrm{EeV}]$. The search for such linear correlations [109] requires that the clusters in figure C.2 are projected into a tangential plane on the celestial sphere through the gnomonic projection. The coordinates of an event in a given cluster

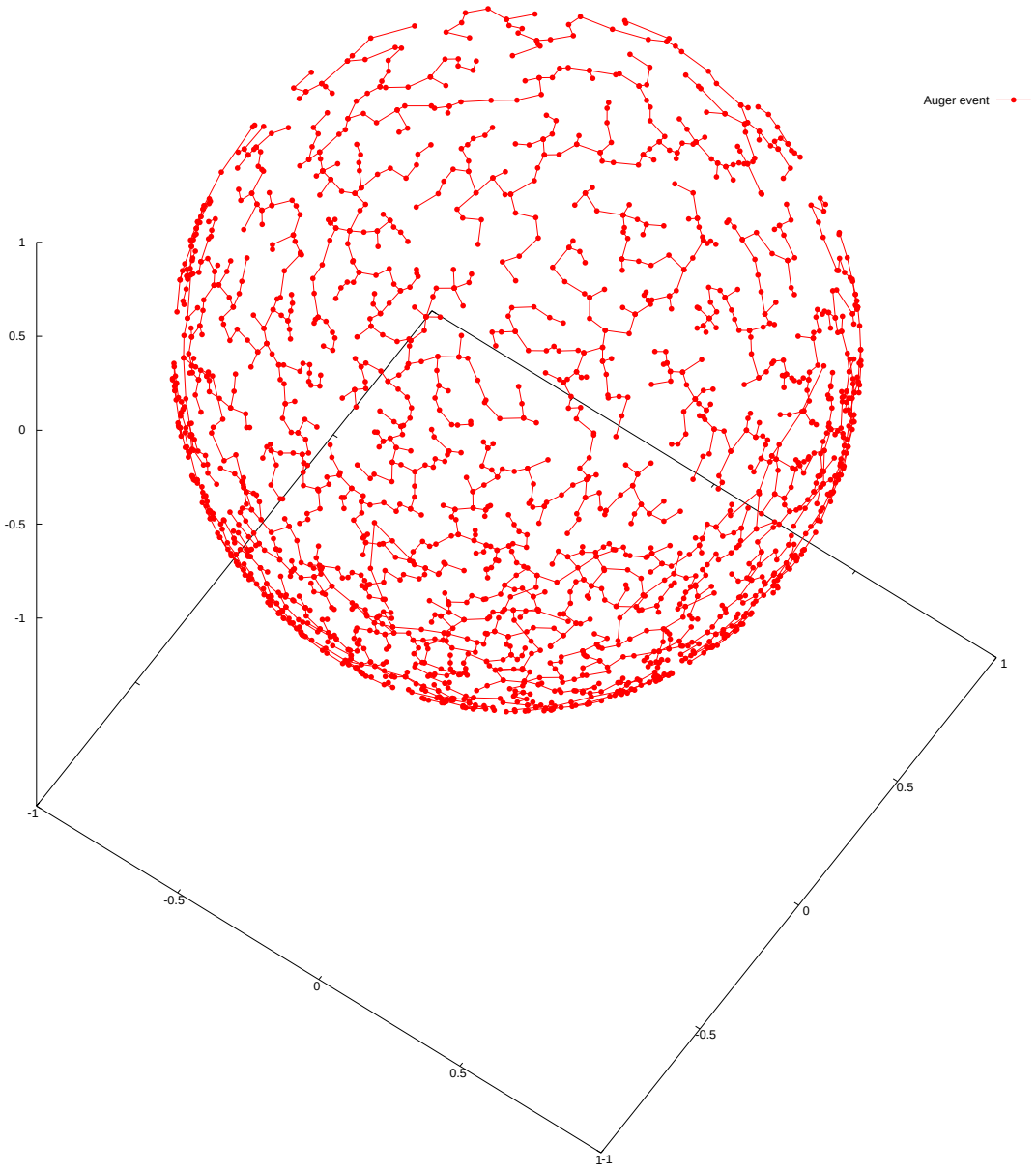

Figure C.1: Minimal spanning tree constructed by using Auger events with energy above 15 EeV, from the period January 2004 to end of 2008. The events are plotted on a unit sphere.

in this plane [111] are given by,

$$x = \frac{\cos\theta \sin(\phi - \phi_0)}{\cos c},$$
$$y = \frac{\cos\theta_0 \sin\theta - \sin\theta_0 \cos\theta \cos(\phi - \phi_0)}{\cos c}, \tag{C.2}$$

where $\cos c$ is given by,

$$\cos c = \sin\theta_0 \sin\theta + \cos\theta_0 \cos\theta \cos(\phi - \phi_0), \tag{C.3}$$

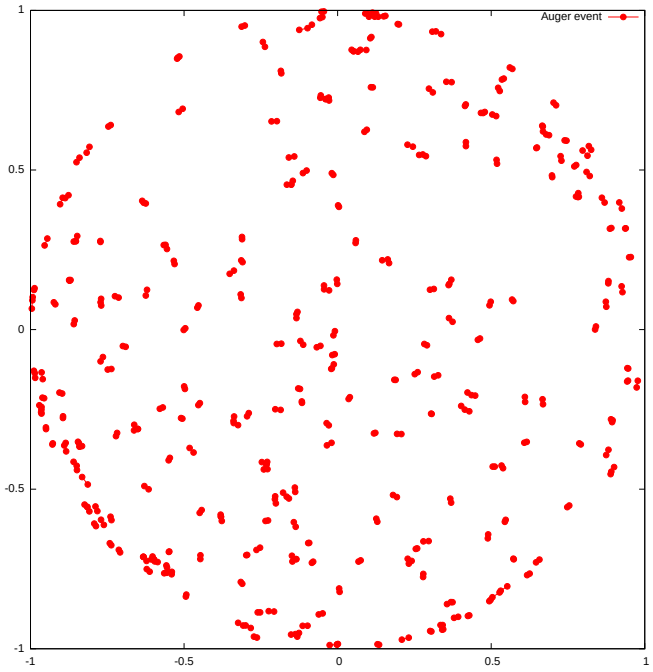

(a) $d_{\max} = 0.5\langle d \rangle$

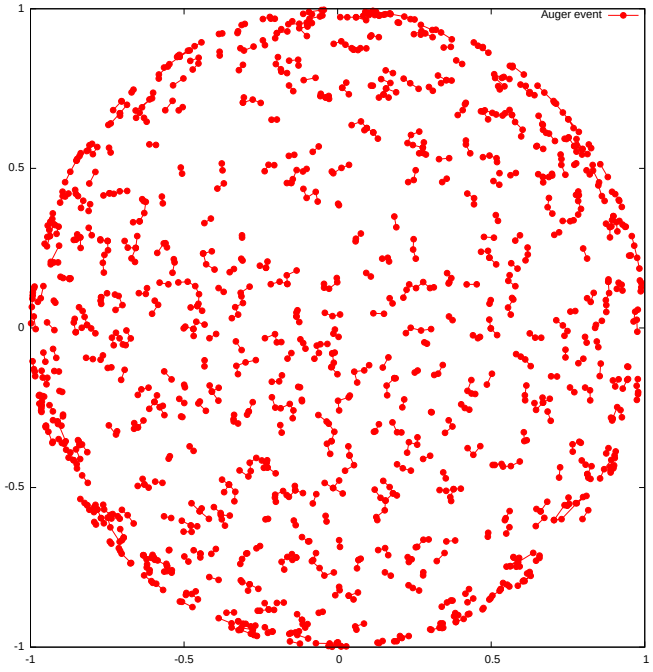

(b) $d_{\max} = 1\langle d \rangle$

Figure C.2: The minimum spanning tree from figure C.1, cut with different maximal lengths $d_{\max}$ as a function of the mean length $\langle d \rangle$ of the uncut tree.

and where θ and ϕ are the galactic latitude and longitude of the projected event. The unit vectors of the events in each cluster are added up and normalized. These new unit vectors, $\hat{n}_0$, provide

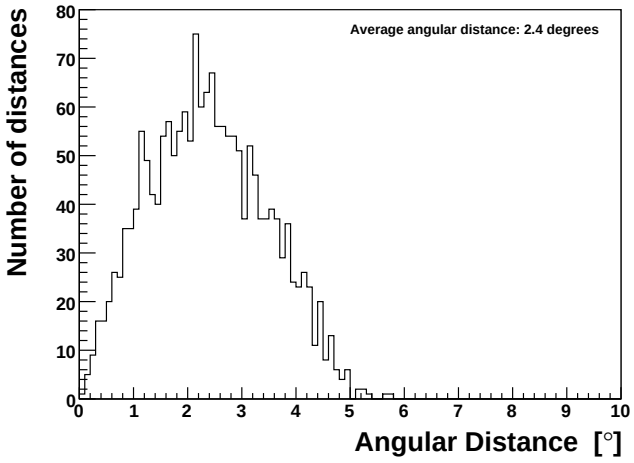

(a) $\text{Energy}_{\text{min}} = 15\,\text{EeV}$

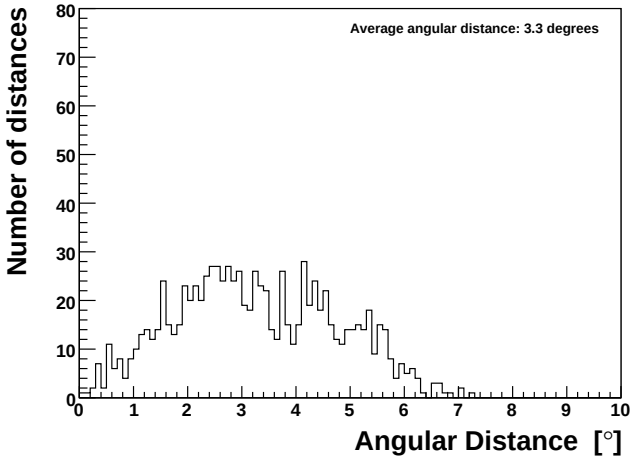

(b) $\text{Energy}_{\text{min}} = 20\,\text{EeV}$

Figure C.3: The distribution of angular lengths between the branches of the full minimal spanning tree, for different energy cuts.

the mean directions of the clusters. θ_0 and ϕ_0 are given by $\hat{n}_0$.

After the gnomonic transformation of the clusters, the covariance between the event coordinates as given by the equations (C.3) and $1/E$, is calculated. In order to maximize this correlation the coordinates are rotated by the angle,

$$\alpha = \arctan\left(\frac{\text{Cov}\,(y, 1/E)}{\text{Cov}\,(x, 1/E)}\right). \tag{C.4}$$

The new coordinates are given by,

$$\begin{aligned} z &= \quad x\cos\alpha + y\sin\alpha, \\ t &= -x\sin\alpha + y\cos\alpha, \end{aligned} \tag{C.5}$$

where z is the longitudinal coordinate so that $\text{Cov}\,(z, 1/E)$ is maximal, and t is the lateral coordinate. As seen in figure C.2 not all of the clusters are thread-like. In order to filter out these clusters following conditions are required to be satisfied,

- The correlation coefficient, $C\,(z, 1/E) = \frac{\mathrm{Cov}(z,1/E)}{\sqrt{\mathrm{Var}(z)\,\mathrm{Var}(1/E)}}$, is larger than 0.95.
- The maximum lateral spread in $\langle t \rangle$ in any cluster is lower than 2°.

The remaining clusters are called thread-like multiplets and are fitted [109] with the relation,

$$z = z_{\mathrm{source}} + \frac{D}{E}. \tag{C.6}$$

The source position is obtained from z_{source}. The deflection power D is a measure of the multiplet deflection. For a large cluster several thread-like multiplets (or threads) might be found as the events in the cluster satify the conditions above in different combinations. Thus, a cluster of seven events might yield two threads of five events each. Additional cuts are made on the deflection power and the location of the reconstructed source. An upper limit on deflection power is set to 1000°EeV, and the source position must be less than 15° away from the event with the highest energy in the cluster. Figures C.4 and C.5 show a septuplet and a nonuplet linearly fitted in the z-$1/E$ plane.

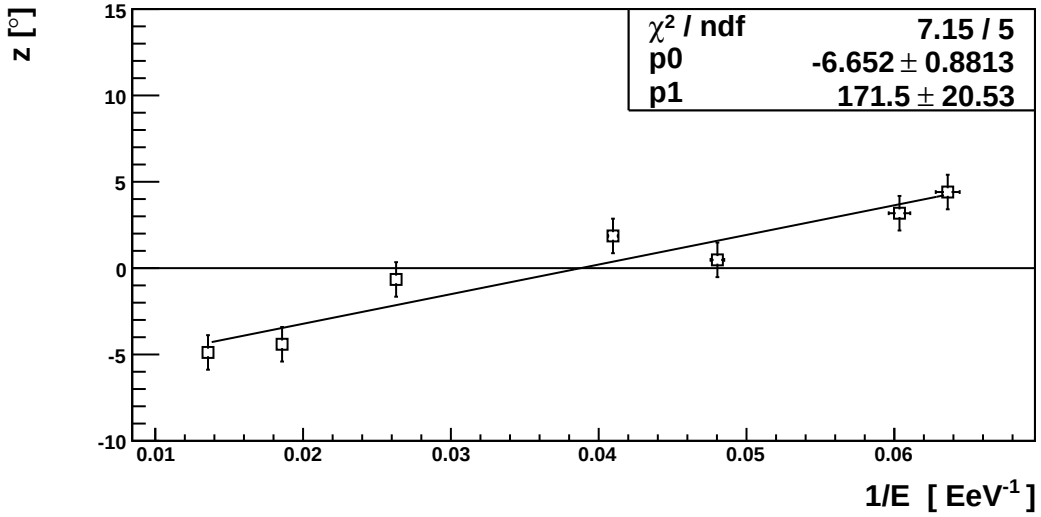

Figure C.4: A septuplet obtained from the minimal spanning tree for $E = 15\,\mathrm{EeV}$ and $d_{\mathrm{max}} = \langle d \rangle$. Here $z_{\mathrm{source}} = -6.7^\circ \pm 0.9^\circ$, and $D = 172^\circ\,\mathrm{EeV} \pm 21^\circ\,\mathrm{EeV}$.

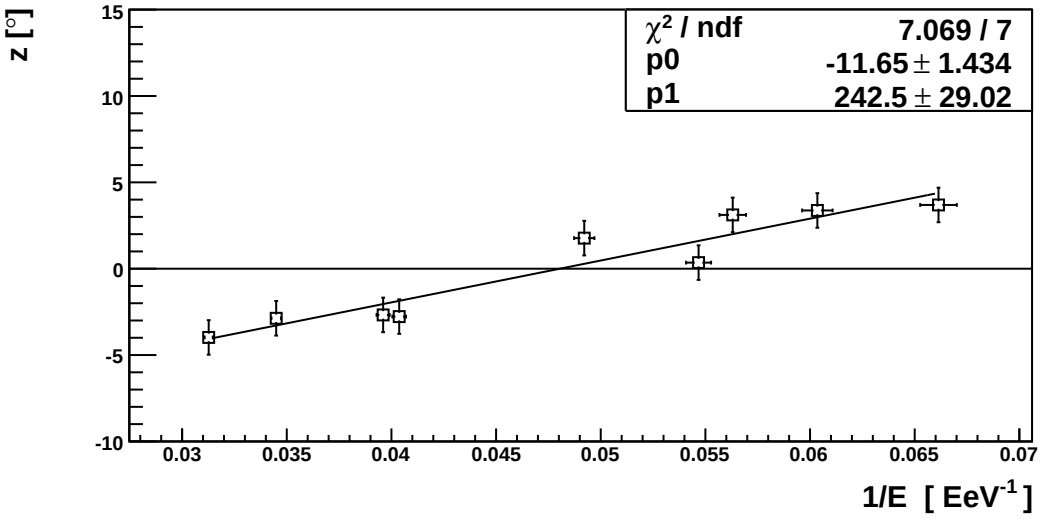

Figure C.5: A nonuplet obtained from the minimal spanning tree for $E = 15\,\mathrm{EeV}$ and $d_{\max} = \langle d \rangle$. Here $z_{\mathrm{source}} = -11.7^\circ \pm 1.4^\circ$ and $D = 243^\circ\,\mathrm{EeV} \pm 29^\circ\,\mathrm{EV}$.

Appendix D

Simulation of Auger Exposure and the Energy Spectrum

D.1 Auger exposure

The Pierre Auger Observatory currently has only one detection site. Located in Argentina it is named the southern Site of the Pierre Auger Observatory. The detection area is thus constrained mostly to the southern hemisphere. The current relative exposure of the Pierre Auger Observatory [117] is given by

$$\omega(\delta) \propto \cos(a_0)\cos(\delta)\sin(\alpha_m) + \alpha_m \sin(a_0)\sin(\delta), \tag{D.1}$$

where δ is the declination, $a_0 = -35.2^\circ$ is the latitude of the southern Site, and α_m is

$$\alpha_m = \begin{cases} 0 & ;\xi > 1, \\ \pi & ;\xi < -1, \\ \arccos(\xi) & ;\text{otherwise} \end{cases} \tag{D.2}$$

where ξ is given by,

$$\xi = \frac{\cos(\theta_m) - \sin(a_0)\sin(\delta)}{\cos(a_0)\cos(\delta)}, \tag{D.3}$$

where $\theta_m = 60^\circ$ is the maximal angle chosen for the "vertical" data set.

D.2 Energy spectrum

The cosmic ray energy spectrum is approximately described by a power law function,

$$\frac{\mathrm{d}N}{\mathrm{d}E} \propto E^{-\gamma}, \tag{D.4}$$

where γ is determined experimentally. The distribution of number of cosmic rays N over energy interval $\mathrm{d}E$ can be described as,

$$f(E) = \frac{\mathrm{d}N}{\mathrm{d}E} = k\,E^{-\gamma}, \tag{D.5}$$

where the normalization k over the energy range $[E_{\min}, \infty]$ is obtained from,

$$\int_{E_{\min}}^{\infty} f(E)\,\mathrm{d}E = 1. \tag{D.6}$$

Equations (D.5) and (D.6) yield,

$$k = \frac{\gamma - 1}{E^{-\gamma+1}}. \tag{D.7}$$

The cumulative distribution function is obtained by integration,

$$g(E) = \int_{E_{\min}}^{\infty} f(E)\,\mathrm{d}E = 1 - \left(\frac{E}{E_{\min}}\right)^{-\gamma+1}. \tag{D.8}$$

Random energies E distributed according to $f(E)$ are generated as,

$$E = g^{-1}(\xi) \tag{D.9}$$

where ξ is a random variable between zero and one. Using equation (D.8), the energies that are simulated are consequently given by,

$$E = E_{\min}(1 - \xi)^{\frac{1}{-\gamma+1}}, \tag{D.10}$$

where $E_{\min}$ is the lowest energy allowed in the simulations. In section 5.6 $E_{\min}$ is set to 30 EeV. The Pierre Auger Collaboration estimates [31] γ to be on average -4.2 for energies above 40 EeV. Here this value is used in the simulations.

Bibliography

[1] V.F. Hess, *Über Beobachtungen der durchdringenden Strahlung bei sieben Freiballonfahrten*, Phys. Zeitschr. **13** (1912) 1084.

[2] V.L. Ginzburg and S.I. Syrovatskii, *The Origin of Cosmic Rays*, Pergamon Press (1964).

[3] A.M. Hillas, *The Origin of Ultra-High-Energy Cosmic Rays*, Ann. Rev. Astron. Astrophys. **22** (1984) 425.

[4] P.L. Biermann and P.A. Strittmatter, *Synchrotron emission from shock waves in active galactic nuclei*, Astrophys. J. **322** (1987) 643.

[5] J.P. Rachen and P.L. Biermann, *Extragalactic ultra high energy cosmic rays, I. Contribution from hot spots in FR-II galaxies*, Astron. & Astrophys. **272** (1993) 161.

[6] C.D. Anderson, *The Positive Electron*, Phys. Rev. **43** (1933) 491.

[7] J.C. Street and E.C. Stevenson, *New Evidence for the Existence of a Particle of Mass Intermediate Between the Proton and Electron*, Phys. Rev. **52** (1937) 1003.

[8] C.M.G. Lattes, G.P.S. Occhialini, and C.F. Powell, *Observations on the Tracks of Slow Mesons in Photographic Emulsions*, Nature **160** (1947) 453.

[9] C.M.G. Lattes *et al.*, *Processes Involving Charged Mesons*, Nature **159** (1947) 694.

[10] E. Parizot, *Cosmic-rays: an overview (part 1)*, talk given at ISAPP-European Doctorate School, France 2007; [http://www.mi.infn.it/ISAPP/editionsold/lectures.html].

[11] R.M. Ulrich, *Measurement of the Proton-air Cross Section using Hybrid Data of the Pierre Auger Observatory*, Doctoral thesis (2008), Forschungszentrum Karlsruhe GmbH (Germany).

[12] [Auger Collaboration] J. Abraham *et al.*, *The Pierre Auger Observatory Design Report, revised 2. edition*; [http://www.auger.org/reports/design report.html].

[13] [High Resolution Fly's Eye Collaboration] T. Abu-Zayyad *et al.*, *Measurement of the Flux of Ultrahigh Energy Cosmic Rays from Monocular Observations by the High Resolution Fly's Eye Experiment*, Phys. Rev. Lett. **92** (2004) 101; [arXiv:astro-ph/0208243v7].

[14] `http://www.auger.org.ar/survey/surveyindex.shtml`.

[15] F. Schuessler, *Top-Down Reconstruction of Ultrahigh Energy Air Showers*, Diploma thesis (2005), Forschungszentrum Karlsruhe GmbH and University of Karlsruhe (Germany); Pierre Auger Collaboration note GAP-2005-094.

[16] M. Nagano and A.A. Watson, *Observations and implications of the ultrahigh-energy cosmic rays*, Rev. Mod. Phys. **72** (2000) 689; [http://prola.aps.org/abstract/RMP/v72/i3/p689_1].

[17] B. Wilczyńska *et al.*, *Variation of atmospheric depth profile on different time scales*, Astropart. Phys. **25** (2006) 106; [arXiv:astro-ph/0603088v1].

[18] T.K. Gaisser *et al.*, *Cosmic-ray composition around* 10^{18} eV , Phys. Rev. D **47** (1993) 1919; [http://prola.aps.org/abstract/PRD/v47/i5/p1919_1].

[19] P. Sommers, *Capabilities of a Giant Hybrid Air Shower Detector*, Astro. Phys. **3** (1995) 349.

[20] T.K. Gaisser, *Cosmic rays and Particle Physics*, Cambridge University Press (1991).

[21] P. Billoir, *Reconstruction of first year EA events from the Surface Detector*, Pierre Auger Collaboration note GAP-2002-044.

[22] D. Veberič and M. Roth, *Offline reference manual - SD reconstruction*, based on Pierre Auger Collaboration note GAP-2005-035.

[23] CDAS Documentation (v4r6), `http://www.auger.org.ar/CDAS/doc/`.

[24] M. Horvat, *Arrival direction measurement of ultra high energy cosmic rays*, Doctoral thesis (2006), University of Ljubljana (Slovenia); Pierre Auger Collaboration note GAP-2006-080.

[25] P. Billoir, *Reconstruction of showers with Ground Array: status of the "prototype" program*, Pierre Auger Collaboration note GAP-2000-025.

[26] M. Horvat and D. Veberič, *On Optimal Barycenter Estimation*, Pierre Auger Collaboration note GAP-2007-035.

[27] P. Sommers, *Extensive air showers and measurement techniques*, C. R. Physique **5** (2004) 463.

[28] M. Roth, on behalf of [Auger Collaboration] J. Abraham *et al.*, *The Lateral Distribution Function of Shower Signals in the Surface Detector of the Pierre Auger Observatory*, Proc. 28th ICRC, Tsukuba, Japan; [arXiv:astro-ph/0308392v1].

[29] A. Watson, on behalf of [Auger Collaboration] J. Abraham *et al.*, *Highlights from the Pierre Auger Obseervatory - the birth of the hybrid era*, highlight talk at the 30th ICRC, Merida, Mexico, July 2007.

[30] J. Hersil *et al.*, *Observations of Extensive Air Showers near the Maximum of Their Longitudinal Development*, Phys. Rev. Lett. **6** (1961) 22; [http://prola.aps.org/abstract/PRL/v6/i1/p22_1].

[31] [Auger Collaboration] J. Abraham *et al.*, *Observation of the Suppression of the Flux of Cosmic Rays above* 4×10^{19} eV, Phys. Rev. Lett. **101** (2008) 061101; [arXiv:0806.4302v1].

[32] F. Kakimoto *et al.*, *A measurement of the air fluorescence yield*, Nucl. Instrum. Phys. Res. A **372** (1995) 527.

[33] D. Kümpel, *Geometry Reconstruction of Fluorescence Detectors Revisited*, Diploma thesis (2007), Bergische Universität Wuppertal (Germany), Pierre Auger Collaboration note GAP-2007-099.

[34] B.R. Dawson *et al.*, *Simulations of a Giant Hybrid Air Shower Detector*, Astropart. Phys. **5** (1996) 239; [http://www.physics.utah.edu/~sommers/hybrid/papers/hybrid_simulations.ps.gz].

[35] P. Sokolsky, *Introduction to Ultrahigh-Energy Cosmic Ray Physics*, Redwood City, USA : Addison-Wesley (1989).

[36] T.K. Gaisser and A.M. Hillas, *Reliability of the Method of Constant Intensity Cuts for Reconstructing the Average Development of Vertical Showers*, Proc. 15th ICRC, Plovdiv, Bulgaria, **8** (1977) 353, Bulgarian Academy of Sciences; [http://adsabs.harvard.edu/abs/1977ICRC....8..353G].

[37] B. Rossi, *High Energy Particles*, Eaglewood Cliffs N J:Prentice-Hall Inc. (1952).

[38] M. Mostafá, for [Auger Collaboration] J. Abraham *et al.*, *Hybrid Activities of the Pierre Auger Observatory*, Nucl. Phys. Proc. Suppl. **165** (2007) 50.

[39] A. Watson, *Highlights from the Pierre Auger Observatory - the birth of the hybrid era*, based on highlight talk at the 30th ICRC, Merida, Mexico, July 2007; [arXiv:0801.2321v1].

[40] M. Roth for [Auger Collaboration] J. Abraham *et al.*, *Measurement of the UHECR energy spectrum using data from the Surface Detector of the Pierre Auger Observatory*, contribution to the 30th ICRC, Merida, Mexico, July 2007; [arXiv:0706.2096v1].

[41] J. Blümer for [Auger Collaboration] J. Abraham *et al.*, *Cosmic rays at the highest energies and the Pierre Auger Observatory*, J. Phys. G: Nucl. Part. Phys. **29** (2003) 867.

[42] J. Blümer, R. Engel, and J.R. Hörandel, *Cosmic Rays from the Knee to the Highest Energies*, submitted to Progress in Particle and Nuclear Physics; [arXiv:0904.0725v1].

[43] J.R. Hörandel, *Models of the Knee in the Energy Spectrum of Cosmic Rays*, Astropart. Phys. **21** (2004) 241; [arXiv:astro-ph/0402356v2].

[44] G. Medina-Tanco, for [Auger Collaboration] J. Abraham *et al.*, *Astrophysics Motivation behind the Pierre Auger Southern Observatory Enhancements*, Proc. 30th ICRC, Merida, Mexico, July 2007; [arXiv:0709.0772v1].

[45] K. Greisen, *End to the Cosmic-Ray Spectrum?*, Phys. Rev. Lett. **16** (1966) 748; [http://prola.aps.org/abstract/PRL/v16/i17/p748_1].

[46] G.T. Zatsepin and V.A. Kuz'min, *Upper limit of the cosmic-ray spectrum*, JETP Lett. **4** (1966) 78; [http://jetpletters.ac.ru/ps/1624/article_24846.shtml].

[47] K.-H. Kampert, private communication.

[48] J. Blümer and K.-H. Kampert, *Die Suche nach den Quellen der kosmischen Strahlung*, Physikalische Blätter, **56** (2000) 39.

[49] A. Achterberg *et al.*, *Intergalactic propagation of UHE Cosmic Rays*, [arXiv:astro-ph/9907060v1].

[50] K. Dolag *et al.*, *Mapping deflections of extragalactic Ultra-High Energy Cosmic Rays in magnetohydrodynamic simulations of the Local Universe*, JETP Lett. **79** (2004) 583; Pisma Zh. Eksp. Teor. Fiz. **79** (2004) 719; [arXiv:astro-ph/0310902v2].

[51] M. Kachelrieß, P.D. Serpico, and M. Teshima, *The Galactic magnetic field as spectrograph for ultra-high energy cosmic rays*, Astropart. Phys. **26** (2006) 378; [arXiv:astro-ph/0510444v2].

[52] R. Beck, *Galactic and extragalactic magnetic fields*, in *The Astrophysics of Galactic Cosmic Rays*, Space Sci. Rev. **99** (2001) 243; [http://www.springerlink.com/content/u1968p2132n81860].

[53] D. Harari *et al.*, *Lensing of ultra-high energy cosmic rays in turbulent magnetic fields*, JHEP **03** (2002) 045; [arXiv:astro-ph/0202362v2].

[54] J.L. Han and G.J. Qiao *The magnetic field in the disk of our Galaxy*, Astron. & Astrophys. **288** (1994) 759; [http://adsabs.harvard.edu/abs/1994A&A...288..759H].

[55] R.G. Rand and A.G. Lyne, *New Rotation Measures of Distant Pulsars in the Inner Galaxy and Magnetic Field Reversals*, Mon. Not. R. Astron. Soc. **268** (1994) 497; [http://adsabs.harvard.edu/cgi-bin/bib_query?1994MNRAS.268..497R].

[56] L.M. Widrow, *Origin of galactic and extragalactic magnetic fields*, Rev. Mod. Phys. **74** (2003) 775; [arXiv:astro-ph/0207240v1].

[57] H. Men, K. Ferrire, and J.L. Han, *Observational constraints on models for the interstallar magnetic field in the Galactic disk*, Astron. & Astrophys. **486** (2008) 819; [arXiv:0805.3454v1].

[58] J.L. Han *et al.*, *Pulsar Rotation Measures and the Large-Scale Structure of the Galactic Magnetic Field*, Astrophys. J. **642** (2006) 868; [arXiv:astro-ph/0601357].

[59] R. Fitzpatrick, *Advanced Classical Electromagnetism, Lectures in PHY387K*, The University of Texas at Austin (1996), `http://farside.ph.utexas.edu/teaching/jk1/lectures/lectures.html`.

[60] R. Beck, *Measurements of Cosmic Magnetism with LOFAR and SKA*, Adv. Radio Sci. **5** (2007) 399; [http://adsabs.harvard.edu/abs/2007AdRS....5..399B].

[61] R. Beck, *Galactic magnetic fields*, Scholarpedia **2** (2007) 2411.

[62] J.L. Han, R.N. Manchester, and G.J. Qiao, *Pulsar rotation measures and the magnetic structure of our Galaxy*, Mon. Not. R. Astron. Soc. **306** (1999) 371; [http://adsabs.harvard.edu/abs/1999MNRAS.306..371H].

[63] Very Large Array radio telescope, `http://www.vla.nrao.edu/`.

[64] Effelsberg radio telescope, `http://www.mpifr-bonn.mpg.de/div/effelsberg/`.

[65] Sterne und Weltraum, `http://www.suw-online.de/`.

[66] Hubble Heritage Team, `http://heritage.stsci.edu/commonpages/infoindex/ourproject/teambio.shtml`.

[67] R. Beck and M. Krause, *Revised equipartition & minimum energy formula for magnetic field strength estimates from radio synchrotron observations*, Astron. Nachr. **326** (2005) 414; [arXiv:astro-ph/0507367v1].

[68] R. Beck *et al.*, *GALACTIC MAGNETISM: Recent Developments and Perspectives*, Annu. Rev. Astron. Astrophys. **34** (1996) 155; [http://nedwww.ipac.caltech.edu/level5/March03/Beck/Beck_contents.html].

[69] R. Powell, *The Atlas of the Universe*, [http://www.atlasoftheuniverse.com/].

[70] J.L. Han, *Magnetic fields in our Galaxy: How much do we know? (II) Halo fields and the global field structure*, CP609 "Astrophysical Polarized Backgrounds", 2002 American Institute of Physics, ed. by S. Cecchini, S. Cortiglioni, R. Sault, and C. Sbarra, (2002) 96; [arXiv:astro-ph/0110319v1].

[71] J.L. Han, *Magnetic fields in our Galaxy: How much do we know? (III) Progress in the Last Decade*, Chinese Journal of Astronomy and Astrophysics, Supplement, 6f, Issue S2, Proceedings of the 2005 Lake Hanas International Pulsar Symposium. Ed: N. Wang, R.N. Manchester, B.J. Rickett, and A. Esamdin., (2005) 211; [arXiv:astro-ph/0603512v2].

[72] M. Fujimoto and M. Tosa, *Spiral Condensation of Gas in Disk Galaxies by Bisymmetric Twisted Magnetic Fields - Two-Dimensional Case*, Publ. Astron. Soc. Japan **32** (1980) 567; [http://adsabs.harvard.edu/abs/1980PASJ...32..567F].

[73] M. Simard-Normandin and P.P. Kronberg, *Rotation measures and the galactic magnetic field*, ApJ **242** (1980) 74; [http://adsabs.harvard.edu/abs/1980ApJ...242...74S].

[74] Y. Sofue and M. Fujimoto, *A bisymmetric spiral magnetic field and the spiral arms in our Galaxy*, ApJ **265** (1983) 722; [http://adsabs.harvard.edu/cgi-bin/bib_query?1983ApJ...265..722S].

[75] J.P. Vallée, *Magnetic field reversals in the Milky Way- "cherchez le champ magnétique"* , Astron. & Astrophys. **308** (1996) 433; [http://adsabs.harvard.edu/abs/1996A%26A...308..433V].

[76] T. Stanev, *Ultra High-Energy Cosmic Rays and the Large-Scale Structure of the Galactic Magnetic Field*, ApJ **479** (1997) 290; [arXiv:astro-ph/9607086v1].

[77] P.G. Tinyakov and I.I. Tkachev, *Tracing protons through the Galactic magnetic field: a clue for charge composition of ultra-high energy cosmic rays*, Astropart. Phys. **18** (2002) 165; [arXiv:astro-ph/0111305v1].

[78] D. Harari, S. Mollerach, and E. Roulet, *The toes of the ultra high energy cosmic ray spectrum*, JHEP **08** (1999) 022; [arXiv:astro-ph/9906309].

[79] M. Prouza and R. Šmída, *The Galactic magnetic field and propagation of ultra-high energy cosmic rays*, Astron. Astrophys. **410** (2003) 1.

[80] R.J. Wainscoat *et al.*, *A model of the 8-25 micron point source infrared sky*, Astrophys. J. Suppl. **83** (1992) 111; [http://adsabs.harvard.edu/abs/1992ApJS...83..111W].

[81] K. Beuermann, G. Kanbach, and E.M. Berkhuijsen, *Radio structure of the Galaxy - Thick disk and thin disk at 408 MHz*, Astron. & Astrophys. **153** (1985) 17; [http://adsabs.harvard.edu/abs/1985A&A...153...17B].

[82] P.G. Tinyakov and I.I. Tkachev, *Deflections of cosmic rays in a random component of the Galactic magnetic field*, Astropart. Phys. **24** (2005) 32; [arXiv:astro-ph/0411669v2].

[83] J.L. Han *et al.*, *Antisymmetric rotation measures in our Galaxy: evidence for an A0 dynamo*, Astron. Astrophys. **322** (1997) 98; [http://adsabs.harvard.edu/abs/1997A&A...322...98H].

[84] K.O. Thielheim and W. Langhoff, *Trajectories of high-energy cosmic rays in the galactic disk* , J. Phys. A: Gen. Phys. **1** (1968) 694.

[85] W.H. Press, S.A. Teukolsky, W.T. Vetterling, and B.P. Flannery, *Numerical Recipes in C. The Art of Scientific Computing*, Cambridge University Press (Cambridge 2002), ISBN 0-521-43108-5.

[86] E. Cheever, *Numerical Solution of Differential Equations*, [http://www.swarthmore.edu/NatSci/echeeve1/Ref/NumericInt/FrameNumInt.html].

[87] `http://sci.esa.int/science-e/www/area/index.cfm?fareaid=21`

[88] G. Weidenspointner *et al.*, *The sky distribution of 511 keV positron annihilation line emission as measured with INTEGRAL/SPI*, [arXiv:astro-ph/0702621v1].

[89] [AGASA Collaboration] N. Hayashida *et al.*, *The Anisotropy of Cosmic Ray Arrival Directions around* $10^{18}eV$, Astropart. Phys. **10** (1999) 303; [arXiv:astro-ph/9807045v2].

[90] J.A. Bellido *et al.*, *Southern Hemisphere Observations of a* $10^{18}eV$ *Cosmic Ray Source Near the Direction of the Galactic Centre*, Astropart. Phys. **15** (2001) 167; [arXiv:astro-ph/0009039v2].

[91] G.A. Medina-Tanco and A.A Watson, *On the possible galactic sources of the ultra-high energy cosmic ray anisotropy at 1 EeV*, Proc. 27th ICRC, Hamburg, Germany, August 2001; [http://adsabs.harvard.edu/full/2001ICRC....2..531M].

[92] [Auger Collaboration] J. Abraham *et al.*, *Anisotropy studies around galactic centre at EeV energies with the Auger Observatory*, Astropart. Phys. **27** (2007) 244; [arXiv:astro-ph/0607382v3].

[93] R. Bonino and G. Navarra, *Study of the Galactic Center region*, Pierre Auger Collaboration note GAP-2008-003.

[94] G. Weidenspointner *et al.*, *A asymmetric distribution of positrons in the Galactic disk revealed by γ-rays*, Nature **451** (2008) 159.

[95] R.W Clay, *Propagation of Cosmic Rays from the Vicinity of the Galactic Centre*, Publ. Astron. Soc. Aust. **17** (2000) 212; [http://adsabs.harvard.edu/full/2000PASA...17..212C].

[96] M. Hussain, S. Vorobiov, and D. Veberič, *Magnetic Deflections of Cosmic Rays from the Galactic Center Region*, Pierre Auger Collaboration note GAP-2008-085.

[97] `http://root.cern.ch/root/html/TMinuit.html`.

[98] [Auger Collaboration] J. Abraham *et al.*, *Correlation of the Highest-Energy Cosmic Rays with Nearby Extragalactic Objects*, Science **318** (2007) 938.

[99] [Auger Collaboration] J. Abraham *et al.*, *Correlation of the highest-energy cosmic rays with the positions of nearby active galactic nuclei*, Astropart. Phys. **29** (2008) 188; [arXiv:0712.2843v2].

[100] D. Harari, S. Mollerach, and E. Roulet, *Correlation of cosmic rays with astronomical objects in the Pierre Auger Observatory data*, Pierre Auger Collaboration note GAP-2006-046.

[101] M.-P. Véron and P. Véron, *A catalogue of quasars and active nuclei: 12th edition*, Astron. & Astrophys. **455** (2006) 773. The authors of reference [99] also acknowledged the use of the VizieR catalogue access tool, CDS, Strasbourg, France, at `http://webviz.u-strasbg.fr/viz-bin/VizieR?-source=VII/248`.

[102] The code used for finding the correlation in reference [98, 99, 100] is found on the homepage of the Bariloche group of the Pierre Auger Observatory, `http://particulas.cnea.gov.ar/experiments/auger/private/AGN/events.html`.

[103] G. Golup *et al.*, *Source position and magnetic field reconstruction from ultra-high energy cosmic ray arrival directions*, submitted to Astropart. Phys., [arXiv:0902.1742v1].

[104] S. Vorobiov, M. Hussain, and D. Veberič, *Large-scale Galactic Magnetic Field and the AGN Correlation*, Pierre Auger Collaboration note GAP-2008-055.

[105] S. Vorobiov, M. Hussain, and D. Veberič, *UHECR propagation in the Galactic Magnetic Field*, based on a talk at the 21st ECRS in Kosice, Slovakia, 9–12 September 2008; [arXiv:0901.1579v1].

[106] S. Vorobiov, M. Hussain, and D. Veberič, *Studies of the UHECR propagation in the Galactic Magnetic Field*, to be published in the proceedings of the ISVHECRI 2008 in Paris, France, September 1–6 2008; [arXiv:0902.3123v1].

[107] R.L. Graham and P. Hell, *On the History of the Minimum Spanning Tree Problem*, Ann. Hist. Comp. **7** (1985) 43.

[108] D. Harari, S. Mollerach, and E. Roulet, *Detecting filaments in the ultra-high energy cosmic ray distribution*, Astropart. Phys. **25** (2006) 412; [arXiv:astro-ph/0602153v2].

[109] D. Harari *et al.*, *Detection of deflection-energy correlations with the Minimal Spanning Tree*, Pierre Auger Collaboration note GAP 2006-106.

[110] D. Harari, S. Mollerach, and E. Roulet, *The Minimal Spanning Tree of Auger data*, Pierre Auger Collaboration note GAP 2006-023.

[111] E.W. Weisstein, *Gnomonic Projection*, From MathWorld–A Wolfram Web Resource, `http://mathworld.wolfram.com/GnomonicProjection.html`.

[112] T. Wibig and A.W. Wolfendale, *Heavy Cosmic Nuclei from Extragalactic Sources above " The Ankle"*; [arXiv:0712.3403v1].

[113] R. Beck and B.M. Gaensler, *Observations of magnetic fields in the Milky Way and in nearby galaxies with a Square Kilometre Array*, New Astron. Rev. **48** (2004) 1289; [arXiv:astro-ph/0409368v2].

[114] H. Goldstein, C.P. Poole, and J.L. Safko, *Classical Mechanics*, Addison-Wesley (2001).

[115] J.H. Field, *Derivation of the Lorentz Force Law, the Magnetic Field Concept and the Faraday-Lenz Law using an Invariant Formulation of the Lorentz Transformation*, Phys. Scripta **73** (2006) 639; [arXiv:physics/0409103v2 [physics.class-ph]].

[116] E.W. Weisstein, *Permutation Symbol*, From MathWorld–A Wolfram Web Resource, `http://mathworld.wolfram.com/PermutationSymbol.html`.

[117] P. Sommers, *Cosmic Ray Anisotropy Analysis with a Full-Sky Observatory*, Astropart. Phys. **14** (2001) 271; [arXiv:astro-ph/0004016v1].